NANOSTRUCTURED THIN FILM ELECTROLYTE FOR THIN FILM SOLID OXIDE FUEL CELLS

A Dissertation

by

SUNGMEE CHO

Submitted to the Office of Graduate Studies of
Texas A&M University
in partial fulfillment of the requirements for the degree of

DOCTOR OF PHILOSOPHY

August 2011

Major Subject: Electrical Engineering

Nanostructured Thin Film Electrolyte for Thin Film Solid Oxide Fuel Cells

NANOSTRUCTURED THIN FILM ELECTROLYTE FOR THIN FILM SOLID OXIDE FUEL CELLS

A Dissertation

by

SUNGMEE CHO

Submitted to the Office of Graduate Studies of
Texas A&M University
in partial fulfillment of the requirements for the degree of

DOCTOR OF PHILOSOPHY

Approved by:

Chair of Committee,	Haiyan Wang
Committee Members,	Mehrdad Ehsani
	Jun Kameoka
	Lin Shao
Head of Department,	Costas N. Georghiades

August 2011

Major Subject: Electrical Engineering

ABSTRACT

Nanostructured Thin Film Electrolyte for Thin Film Solid Oxide Fuel Cells.

(August 2011)

Sungmee Cho, B.S., Dajin University, Korea;

M.S., Hongik University, Korea

Chair of Advisory Committee: Dr. Haiyan Wang

Solid oxide fuel cells (SOFCs) are very attractive as energy generation devices because they are clean, reliable, and almost entirely pollution-free. SOFCs have flexible fuel selections compared with other fuel cell technologies. The main disadvantage of SOFCs is their high operating temperature (~1000ºC for conventional SOFCs) which leads to cell cracking and formation of non-conducting compounds at electrolyte/electrode interfaces. Therefore, intermediate temperature SOFCs (ITSOFCs) in the range of 500-700 ºC has attracted extensive research interests. To achieve high cell performance at reduced temperatures, it requires high-catalytic activity, high ionic conductivity, and comparable thermal expansion coefficient (TEC) of the cell components. To address the above issues, the research focuses on two main approaches (i.e., the interlayer approach and the electrolyte approach) in order to improve the overall cell performance. First, the design of a thin layer of a vertically-aligned nanocomposite (VAN) structure as an interlayer between the electrolyte and cathode is demonstrated. The development of the VAN structures consisted of the cathode material as a perovskite or ordered double perovskite structure, $La_{0.5}Sr_{0.5}CoO_3$ (LSCO) or $PrBaCo_2O_{5+\delta}$ (PBCO),

and the electrolyte material as a fluorite structure, $Ce_{0.9}Gd_{0.1}O_{1.95}$ (CGO or GDC), were achieved for thin film solid oxide fuel cell (TFSOFCs). The VAN structure significantly improves the overall performance of the TFSOFC by increasing the interfacial area between the electrolyte and cathode and also acts as a transition layer that improves adhesion and relieves both thermal stress and lattice strain. Second, microstructural and electrical properties of Gd-doped CeO_2 (GDC, $Ce_{0.9}Gd_{0.1}O_{1.95}$) thin films electrolyte are studied for intermediate temperature solid oxide fuel cells (SOFCs). The GDC thin film electrolytes with different grain sizes and grain morphologies were prepared by varying the deposition parameters such as substrate temperature, oxygen partial pressure, target repetition rate, and laser ablation energy. The electrical property of the GDC thin film is strongly affected by the grain size. Third, bilayer electrolytes composed of a gadolinium-doped CeO_2 (GDC) layer (~6 μm thickness) and an yttria-stabilized ZrO_2 (YSZ) layer with various thicknesses (~330 nm, ~440 nm, and ~1 μm) are achieved by a pulsed laser deposition (PLD) technique for thin film solid oxide fuel cells (TFSOFCs). One effective approach is to incorporate YSZ thin film as a blocking layer in between the GDC and anode for preventing chemical reduction of GDC and electrical current leakage. This bilayer approach effectively improves the GDC's chemical/ mechanical stability and reduces the OCV loss under reducing conditions. The results suggest that the YSZ thin film serves as a blocking layer for preventing electrical current leakage in the GDC layer and also provides chemical, mechanical, and structural integrity in the cell, which leads to the overall enhanced performance.

DEDICATION

I dedicate this dissertation to my family, to father, mom, and sisters.

ACKNOWLEDGEMENTS

First of all, I would like to thank all the people who have helped and encouraged me during my doctoral study.

I really would like to thank my Ph.D. advisor, Dr. Haiyan Wang, for providing great research advice, accessible teaching and financial support which is an incredibly precious opportunity for me at Texas A&M University. In addition, she was always accessible and willing to help her students with their research. As a result, research life became rewarding for me. I would like to thank my committee members, Professors Mehrdad Ehsani, Jun Kameoka, and Lin Shao, for their guidance and support through the course of this research.

I want to thank all my lab friends, Chen-Fong Tsai, JoonHwan Lee, Zhenxing Bi, Michelle Myers, Li Chen, Fauzia Khatkhatay, Qing Su, Aiping Chen, ZhuYuanyuan, Jiao Liang, and Tommy Lynch, for making my time at Texas A&M University a great experience and my colleagues, Dr. Jung-Hyun Kim and Dr. YoungNam Kim and Dr. Arumugam Manthiram at the University of Texas at Austin, for giving me a great opportunity for collaboration on measuring power performance of the single cells.

I would like to thank my former master's advisors, Professor JeBack Ju and Taewon Sohn in Chemical Engineering, at the Hongik University and Professor Dong-Myung Shin, professor of Chemical Engineering at the Hongik University, who have been my teachers and the offered advice and suggestions for many years.

Lastly, thanks to my family, particularly, my mother and 2nd sister, Minji Cho, for their financial support and encouragement and to my husband, HyungDae Jin, for his support and love.

TABLE OF CONTENTS

Page

Page

Page

LIST OF FIGURES

FIGURE Page

FIGURE Page

FIGURE Page

FIGURE Page

LIST OF TABLES

CHAPTER I

INTRODUCTION

1.1 Fuel Cells

Fuel cell is an interesting electrochemical device which converts chemical energy of a reaction into electrical energy directly. The electrochemical reactions occur at the electrodes to generate an electric current through an electrolyte, while the generated corresponding electric current performs work on the load. Based on the selection of the electrolyte and fuel, fuel cell types can be determined by the electrode reactions and types of ions. They are promising power generation systems with a low emission and a high efficiency. Unlike conventional power generations, the fuel cells are unrestricted by thermodynamic limitations of heat engines, e. g., as Carnot efficiency.

1.1.1 Basic Principles of Fuel Cells

Sir William Rovert Grove, a pioneer of fuel cell technology, demonstrated the first fuel cell in 1839 [1]. Based on his demonstration, electrochemical cells are classified as either galvanic or electrolytic cells [2]. First, the galvanic cell creates a spontaneous reaction at the electrodes when the cell is connected with an external conductor. This cell is used in converting chemical energy into electrical energy such as primary cells, secondary cells (battery) and fuel cells. Second, the electrolytic cell carries out desired chemical reaction by expending electrical energy. As shown in Fig 1.1(b),

---

This dissertation follows the style and format of *Advanced Functional Material.*

the reactions are effected by a high external voltage and the reversible potential of the cell. Commercial electrolytic cells are electrorefining, electrolytic cells, and electroplating.

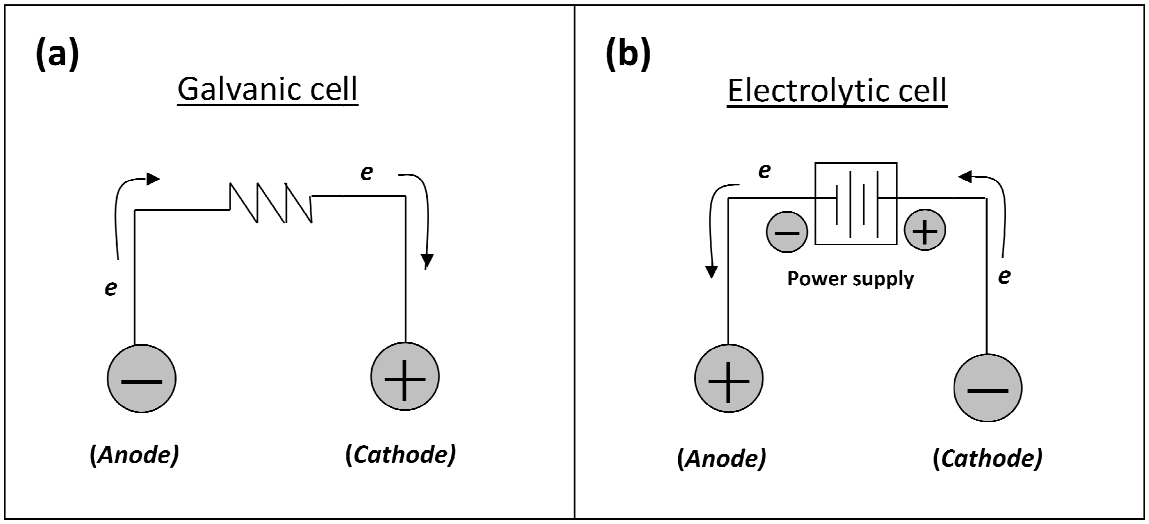

Fig 1.1. Schematic illustration of electrochemical cells (a) galvanic cell, (b) electrolytic cell [2].

The basic physical structure of a fuel cell consists of an electrolyte layer in contact with a porous anode and cathode on both sides as shown schematic diagram in Fig 1.2. Typically, a constant fuel is supplied to the anode side (negative) and an oxidant is fed the cathode (positive). The fuel cell generates electricity inside a cell through electrochemical reactions between a fuel and an oxidant, and it can operate continuously as long as the necessary reactant and oxidant flows are provided.

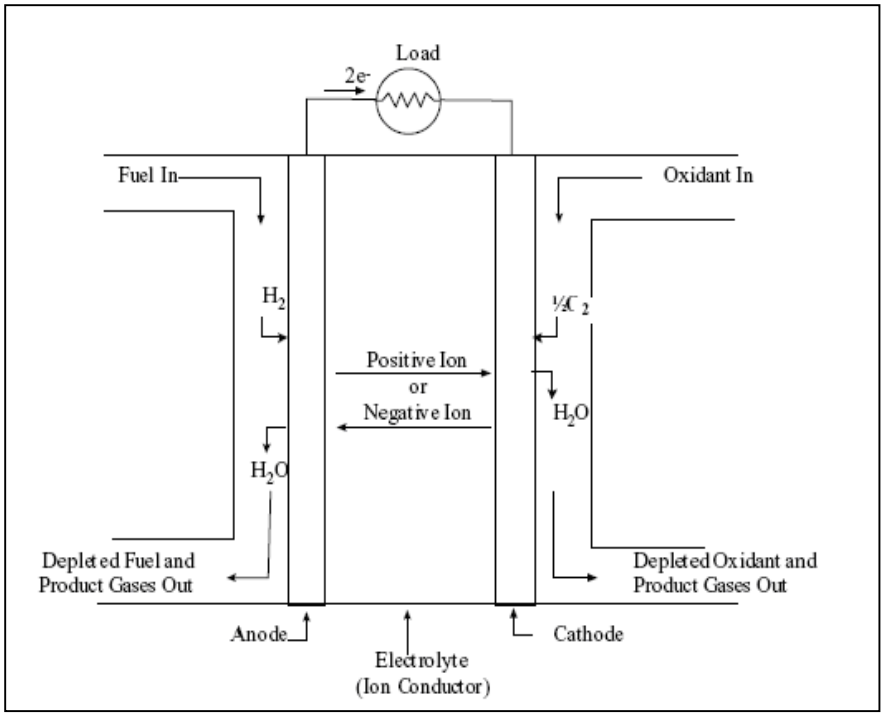

Fig1.2. Illustration of the working mechanism of an individual fuel cell [3].

1.1.2 Types of Fuel Cells

Based on the selection of the electrolyte and fuel, the fuel cell can be classified into five major types, i.e., polymer electrolyte fuel cell (PEFC), alkaline fuel cell (AFC), phosphoric acid fuel cell (PAFC), molten carbonate fuel cell (MCFC), and solid oxide fuel cell (SOFC) as shown in Table 1.1 [3-4]. For instance, the fuel cell can utilize a proton-conducting electrolyte, such as is the case for a solid acid, PEFC, and PAFC in which the anode to cathode electronic and ionic flues are inverted compared to the oxygen conducting cells. Other fuel cell variants, such as MCFC, which conduct CO_3^{2-} ions, and AFC, which conduct OH^- ions, have confined their applications. Further, these fuel cells also can be separated depending on the operating temperature, which plays a

crucial role in determining the fuel processing requirement for the choice of the electrolyte. All of the fuel has to be transferred to hydrogen prior to arrive at the cell in low temperature fuel cells. In high temperature fuel cells, CO or CH_4 can be converted to hydrogen. Consequentially, all of the cell components have the same property requirements although the differentiation across the various types of fuel cells.

Table 1.1. A summary of fuel cell types [3].

	PEFC	AFC	PAFC	MCFC	ITSOFC	TSOFC
Electrolyte	Ion Exchange Membranes	Mobilized or Immobilized Potassium Hydroxide	Immobilized Liquid Phosphoric Acid	Immobilized Liquid Molten Carbonate	Ceramic	Ceramic
Operating Temperature	80°C	65°C - 220°C	205°C	650°	600-800°C	800-1000°C
Charge Carrier	H^+	OH^-	H^+	$CO3^=$	$O^=$	$O^=$
External Reformer for CH_4 (below)	Yes	Yes	Yes	No	No	No
Prime Cell Components	Carbon-based	Carbon-based	Graphite-based	Stainless-based	Ceramic	Ceramic
Catalyst	Platinum	Platinum	Platinum	Nickel	Perovskites	Perovskites
Product Water Management	Evaporative	Evaporative	Evaporative	Gaseous Product	Gaseous Product	Gaseous Product
Product Heat Management	Process Gas + Independent Cooling Medium	Process Gas + Electrolyte Calculation	Process Gas + Independent Cooling Medium	Internal Reforming + Process Gas	Internal Reforming + Process Gas	Internal Reforming + Process Gas

1.2 Solid Oxide Fuel Cells

Solid oxide fuel cells have received much attention as a third generation fuel cell technology because they are cleans, reliable, and almost entirely nonpolluting. Additionally, it is not necessary to use only hydrogen as a fuel compared with that of other fuel cell technologies. The entire cell component consists of ceramic or ceramic metal materials, which operates at high temperatures (<1000°C) for an adequate ionic and electronic conductivity.

The high operating temperature makes it possible for the cell to react in fast electrochemical kinetics, and makes it unnecessary to use platinum catalyst. Waste heat can also be utilized for additional electric power generation during the cell operation. Moreover, the variable fuels such as hydrogen, hydrocarbons, and H_2/CO mixture gas can be used as a fuel in the cell since the high operation temperature makes the internal in situ reforming hydrocarbons [3, 5].

SOFC is an appropriate power generation system for a number of applications including mobile, military, vehicle, auxiliary power units, and stationary system. One of the most promising is large stationary power plants (>100MW) with coal as the primary fuel. Another productive market is auxiliary power for large transport vehicles, e. g., heavy-duty transportation trucks. There is a great potential to deploy some of the waste heat from the SOFCs for other applications because of its high operating temperatures to increase the overall efficiency.

1.2.1 Principles of SOFC

The SOFC is an all solid state power system which generates electricity by conducting the electrochemical reactions at the electrodes. The fuel is supplied to the anode, whereas the oxidant is fed to the porous and exist an electrochemical potential for the chemicals to react. The dense electrolyte prevents the gases from mixing and allows ion (negative) transport from the cathode to the anode as shown in Fig 1.3 [6]. Consequently, half of the cell reactions take place at the electrodes and then produced ions can go through the electrolyte. For example, oxygen will be reduced at the cathode to generate O^{2-} ions that transport through the electrolyte and react with the fuel (hydrogen) at the anode. The anode releases electrons that are consumed at the cathode, and the electron current goes through an external circuit, balancing the ion flux.

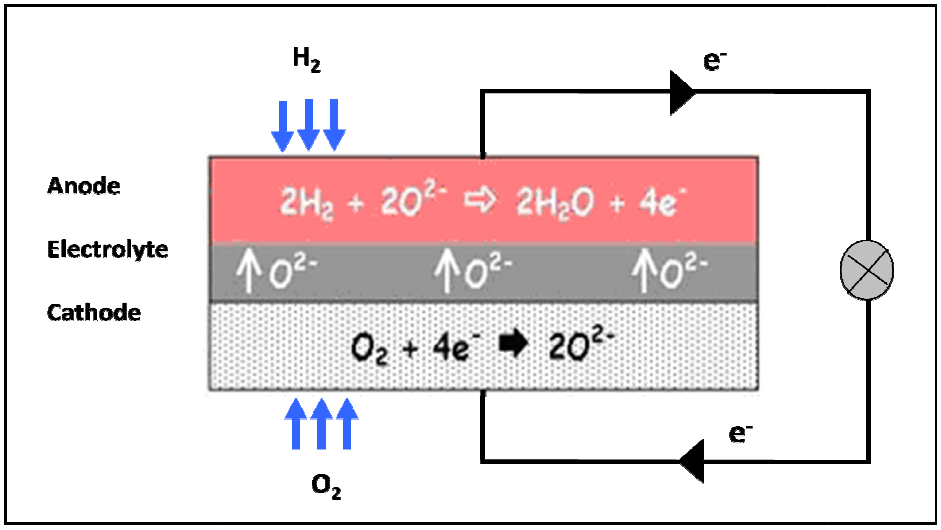

Fig 1.3. Schematic diagram of a SOFC.

The schematic diagram in Fig 1.4 shows the single cell structure of SOFCs. Traditionally, the SOFC have utilized a lanthanum strontium manganate (LSM) cathode, an yttria-stabilized zirconia (YSZ) electrolyte, and a nickel-YSZ composite anode. In order for the electrochemical reaction in the cell, the anode and cathode must be porous for their oxidation reaction (anode) and reduction reaction (cathode), and the electrolyte must require a pin-hole free film.

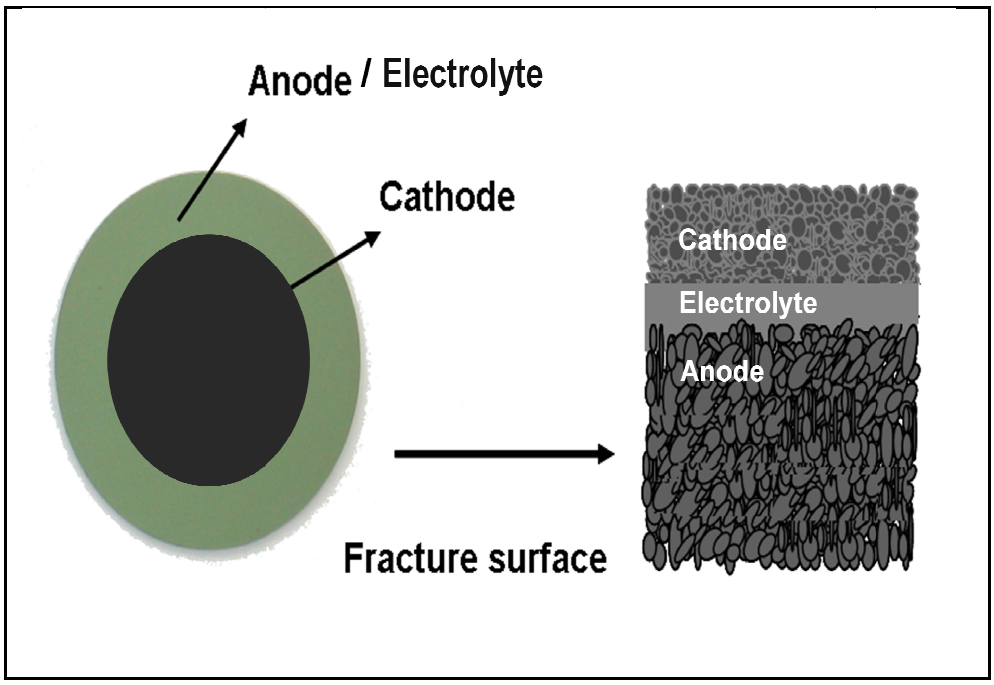

Fig 1.4. Schematic diagram of SOFC single cell.

1.2.2 Electrochemistry: Gibbs Free Energy and Nernst Potential

To understand the fuel cell operation, the chemical and thermodynamic relations need to be defined. The maximum electrical work (W) with a constant pressure and temperature in the fuel cell operation, performs the change of Gibbs free energy (ΔG) by electrochemical reaction [3]

$$W = \Delta G = -nFE \tag{1.1}$$

where n is the numbers of electrons contributed in the chemical reaction, F is Faraday's constant, and E is the ideal potential. Therefore, the Gibbs free energy change is given depending on the temperature

$$\Delta G = \Delta H - T\Delta S\, nFE \tag{1.2}$$

where ΔH is the enthalpy change and ΔS is the entropy change. The total available thermal energy is ΔH. The amount of heat is produced by reversible fuel cell operation, which is TΔS. The fuel has negative entropy change which generates the heat (hydrogen oxidation) in reactions while positive entropy change extracts the heat (direct solid carbon oxidation) if the irreversible generation of the heat is smaller than the reversible absorption of the heat.

The reversible potential of a fuel cell can be presented by Nernst equation as [3, 7]

$$E = \mathrm{E}^{\circ} + \frac{\mathrm{RT}}{\mathrm{nF}} \ln\left(\frac{\mathrm{P_{H_2}} \cdot \mathrm{P_{O_2}}^{1/2}}{\mathrm{P_{H_2O}}}\right) \quad (1.3)$$

The Nernst equation provides a relationship between the ideal potential (E°) for the cell reaction and the ideal equilibrium potential (E) at a different partial pressure of reactants and products. With an increase in the partial pressure of the reactants and a decrease in the partial pressure of the products, the cell potential is raised in the overall cell reaction. For instance, the ideal cell potential at a given temperature can be increased by operating at higher reactant pressures in the hydrogen reaction, which will show better fuel cell performance.

The ideal potential of a fuel cell (E°) is 1.229 volts at the standard condition. The relation of E° to cell temperature can be expressed as a change in the Gibbs free energy which increases as the cell temperature decreases. The ideal potential of a cell is proportional to the change in the standard Gibbs free energy. In practice, the actual cell potential is decreased from its equilibrium potential due to irreversible losses of polarization, and overpotential. There are three main polarizations: activation polarization (η_{act}), ohmic polarization (η_{ohm}) and, concentration polarization (η_{conc}) as shown in Fig 1. 5 [3]. These losses result in a lower cell voltage that is less than its ideal potential, E (V = E - Losses). The activation polarization is dominated by the rate of the electrochemical reaction in the electrodes at a low current density. The ohmic polarization occurs due to the resistance to the flow of ions in the electrolyte and

electrons through the electrode materials by the poor ionic conductivity of the electrolyte and electrode separation. Finally, the concentration polarization is related to mass transfer or slow diffusion under the gas phase in the electrode pores and occurs over the entire range of the current density. These losses become prominent at high limiting currents where it becomes difficult to supply sufficient reactant flow to the cell reaction sites.

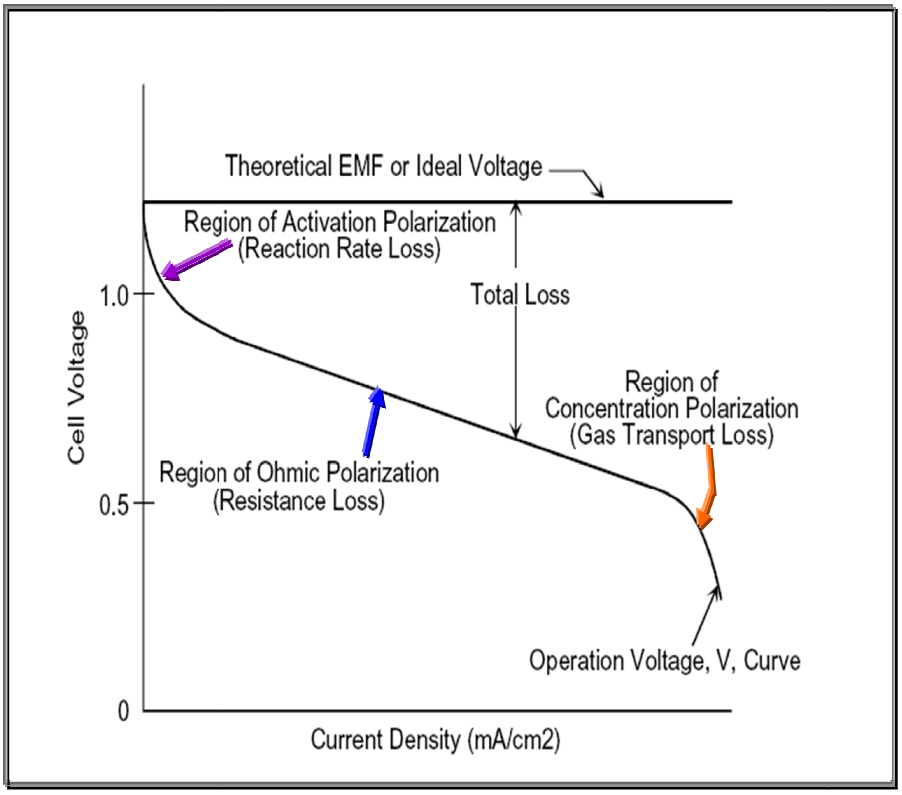

Fig 1.5. Actual and ideal cell potential in SOFCs [3].

1.2.3 Advantages and Disadvantages of SOFC

The SOFC brings up individual advantages and disadvantages according to the material construction, fabrication techniques, and different system requirements [3, 6]. First, SOFCs have the advantages of vibration free, higher system efficiency, higher power density, and simpler designs than fuel cells based on liquid electrolytes. The more benefits of SOFCs are based on a number of aspects as follows.

(1) Taking advantages of its waste heat, additional power can be produced.

(2) It has a high efficiency (40-60% unassisted, up to 70% in pressurized hybrid system) compared to engines and modern thermal power plants (30-40% efficient).

(3) Water management is not required because the byproduct is steam rather than liquid water.

(4) SOFCs can be operated on high-energy density hydrocarbon fuels such as propane and butane as well as CO_2, CH_4, N_2, and CO.

Due to a high operating temperature of 1000°C in SOFCs, this brings about the decreased the cell lifetime and increased the cost of materials, since expensive high temperature alloys are used to house the cell, and high costs of ceramics are used for the interconnections, which leads to increase the overall cost of the fuel cell substantially. Therefore, lower operation temperature has been recognized universal as the key point for low cost SOFCs. The limitations of SOFC also include:

(1) Material costs are high, particularly for interconnect and construction materials.

(2) The use of volatile chromium containing ceramics and alloys can result in the contamination of the stack components.

(3) Due to its high operating temperature, corrosion and breakdown of cell components are the problem.

1.2.4 Thin Film SOFC

Conventional SOFCs have several problems such as electrode sintering, the electrode/electrolyte interfacial diffusion, and the mechanical stress, which are associated with its high operating temperature of 1000°C. Accordingly, much attention has been focused on intermediate temperature SOFCs in the temperature range of 400-700°C. However, its low operating temperature brings about a lower conductivity and overpotentials in the air and at the fuel electrode although the SOFC allows a wider choice of electrode materials and interconnects materials [8]. Several approaches to increase the conductivity across the electrolyte are either replacing a conventional electrolyte material (YSZ) by alternative electrolyte materials for enhancing its conductance or reducing the electrolyte thickness using thin film deposition techniques such as CVD, PLD EVD, sol-gel deposition and sputtering [9-13]. In the past few decades, there has been a progressive trend towards the se of thinner SOFC components, in the case of the electrolyte, which is a significant factor for enhanced SOFC performance, e.g., the thickness of the electrolyte must be reduced from ~200μm to a few microns to avoid the compromising power output at a low operating temperature. In addition, techniques for the thin film deposition at the nanoscale have been explored in

controlled epitaxial thin films, multilayers and tuning microstructures in order to improve the electrochemical performance of SOFC materials. The schematic diagram represents typical three types of thin film SOFC configurations as shown in Fig 1. 6.

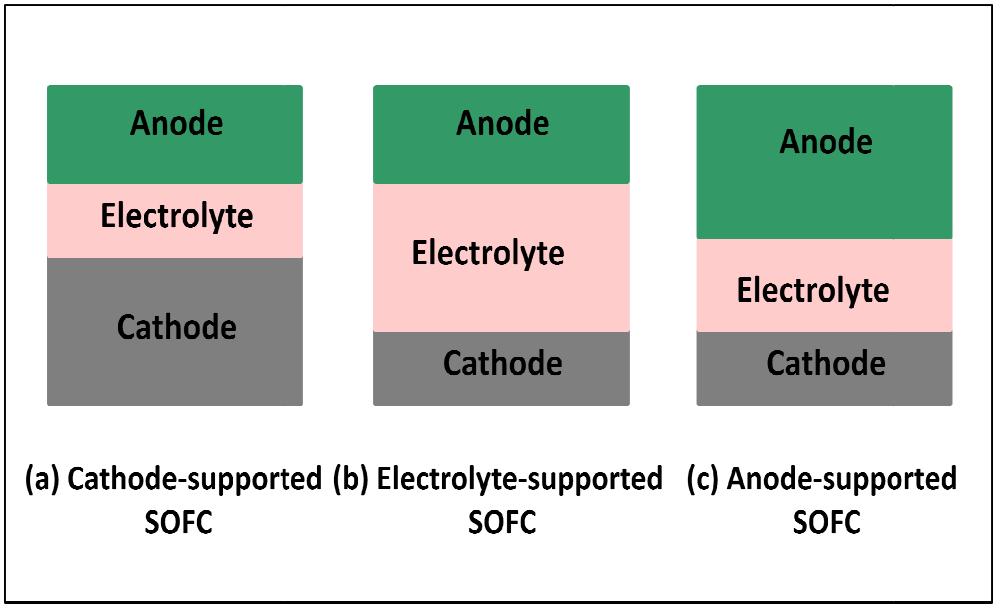

Fig 1.6. Three types of thin film SOFCs configurations.

1.3 SOFC Components

SOFCs are composed of three main components: anode, cathode, and electrolyte. The requirements of the operation condition are the chemical/mechanical stability (e.g., chemical phase, morphology) in oxidation and reduction conditions, chemical compatibility with other components, and the appropriate conductivity. In addition, both the cathode and anode must be porous to allow gas transport to the reaction sites, whereas the electrolyte must be fully dense to separate the oxidant and fuel gas. A summary of SOFC components is given in Table 1.2 [14].

Table 1.2. A summary of SOFC components [14].

Components	Materials	TEC ($\times 10^{-6}$ K^{-1})
Electrolyte	$Ce_{0.8}Sm_{0.2}O_{1.9}$	11.4
	$Ce_{0.8}La_{0.2}O_{1.9}$	11.8
	CeO_2	11.8
	8 mol% YSZ	10.3
Cathode	$LaMnO_3$	11.2
	$La_{0.8}Sr_{0.2}MnO_3$	12.4
	$La_{0.6}Sr_{0.4}Co_{0.2}Fe_{0.8}O_{3-x}$	12.5
	$La_{0.5}Sr_{0.5}CoO_{3-x}$	17.5
Anode	Ni–YSZ (Ni 15–30 vol%)	11–12
Interconnector	Fe–Cr–Ni alloy	15–20
	$La_{0.8}Sr_{0.2}CrO_3$	11.1
	$La_{0.9}Cr_{0.1}Mg_{0.1}O_3$	9.5

1.3.1 Anode

The anode has a porous structure with a catalytic active zone where the fuels allow easy to transport and arrive at the electrolyte, which must remain stable under the highly reducing fuel conditions (P_{O2}= ~10^{-20}). The electrochemical reactions take place at the triple phase boundary (TPB) [15]. The connection exists among an oxide ion conducting, electron conducting, and the fuel gas phase diffusion. The anode material must conduct electrons as well as a good ionic conductivity; a mixed ionic-electronic conductor (MIEC) provides oxygen ions and removes electrons that are produced during the oxidation as shown in Fig. 1. 7.

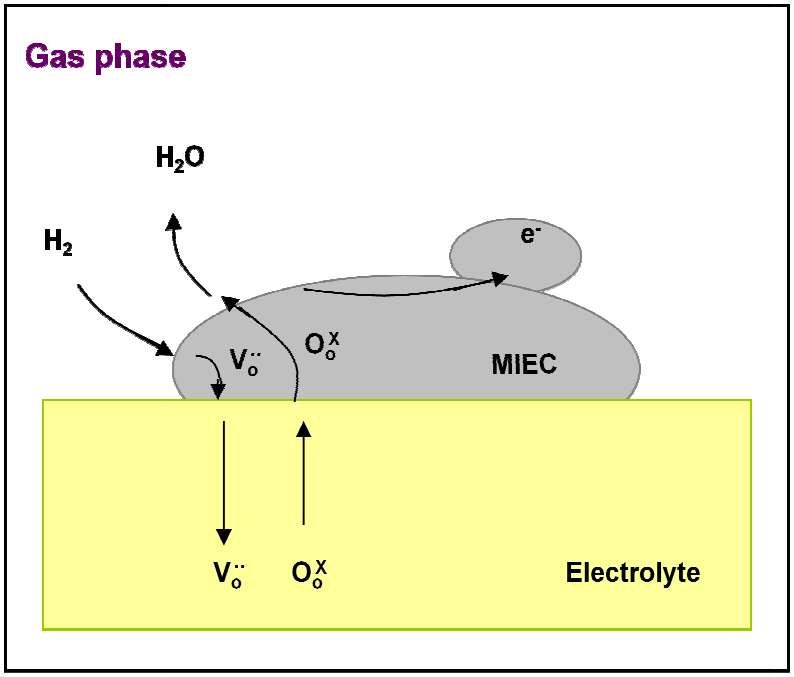

Fig 1.7. Entire surface of MIEC in electrochemical reactions.

The most common material is a ceramic metal mixture of nickel/yttria-stabilized zirconia (Ni/YSZ) cermet for the anode [16-17]. Nickel is the best candidate considering the advantages of good chemical stability, catalytic activity, and cost under reducing conditions at a high temperature of 1000ºC. Besides, the cermet mixture with YSZ can give a similar thermal expansion coefficient (TEC), which can match with other cell components. In addition, a property of the YSZ in the anode inhibits the sintering of the metallic particles. Other materials such as cobalt and noble metals are also possible candidates. A summary of the important requirements for the anode is given as [18]:

(1) Long term stability at high operating temperatures and retaining good electronic /ionic conductive phases with enough porosity.

(2) Match TEC with the electrolyte to prevent electrode cracking or delaminating.

(3) Low polarization resistance of the electrode.

(4) Chemical stability in reducing conditions at high temperatures.

(5) High catalytic activity to support electrochemical reaction of the fuel with oxygen ions.

1.3.2 Electrolyte

The SOFC electrolyte is a dense layer of ion ceramic oxide is conducting material which conducts oxygen ions and allows the kinetics of the oxygen ion transport to be sufficient for the cell performance at a high operation temperature range of 900-1000 ℃. Yttria-stabilized zirconia (YSZ), the most common electrolyte, has a high oxygen-ion conductivity of 0.1 S/cm at 1000℃ [19-21]. Pure ZrO_2 does not serve as a good electrolyte due to its low ionic conductivity, i.e., doping Y_2O_3 with ZrO_2 results in a substitution of Y^{3+} on the Zr^{4+} cation, which shows a reliable conductivity. This substitution makes large oxygen vacancies as well as the stable cubic fluorite structure as shown in Fig 1.8. However, its high operation temperatures give some problems in material selections for SOFC components, mechanical strength of the cells, and the life time of the cells. To overcome those drawbacks, electrolyte materials with a high ionic conductivity are needed for low operation temperature SOFCs.

Many efforts have been made to improve the ionic conductivity in SOFCs using alternative electrolyte materials such as gadolinia doped-ceria (GDC), lanthanum strontium gallate magnesite (LSGM), and scandia-stabilized zirconia (ScSZ). These materials have significantly higher conductivities at intermediate temperatures as shown

in Fig 1.9 [22]. GDC is one of the most promising candidates because of its high ionic conductivity which can be used for low temperature SOFC applications [23-24]. However, the GDC electrolyte is a mixed ionic and electronic conductor (MIEC), which can not only increase the electronic conductivity under a reducing condition but also decrease the theoretical voltage caused by the reduction of ceria from Ce^{4+} to Ce^{3+} where the anode side is exposed to the fuel. The perovskite-based material (ABO_3) is considered as another option for the electrolyte. Since ABO_3 can take on a number of different structures with aliovalent cations doping on the AB sites which can also accommodate very large concentrations of anion vacancies into their structures. Particularly, the $LaGaO_3$-based perovskite type oxide, LSGM, exhibits high oxygen ion conductivity (0.12 S/cm at 800ºC) and the excellent structural and chemical compatibility with perovskite cathode materials, e. g., lanthanum cobaltite [25-28]. However, the LSGM reacts with nickel electrodes which can be minimized by adding a CeO_2 buffer layer between the two materials.

In addition, the electrolyte requirements for SOFC applications can be summarized as follows.

(1) Chemical, morphological stabilities under the dual condition;

(2) Adequate ionic conductivity in the dual atmospheres;

(3) Chemical compatibility with other components;

(4) Matching TEC to avoid crack and delamination;

(5) Denseness to prevent gas cross leakage.

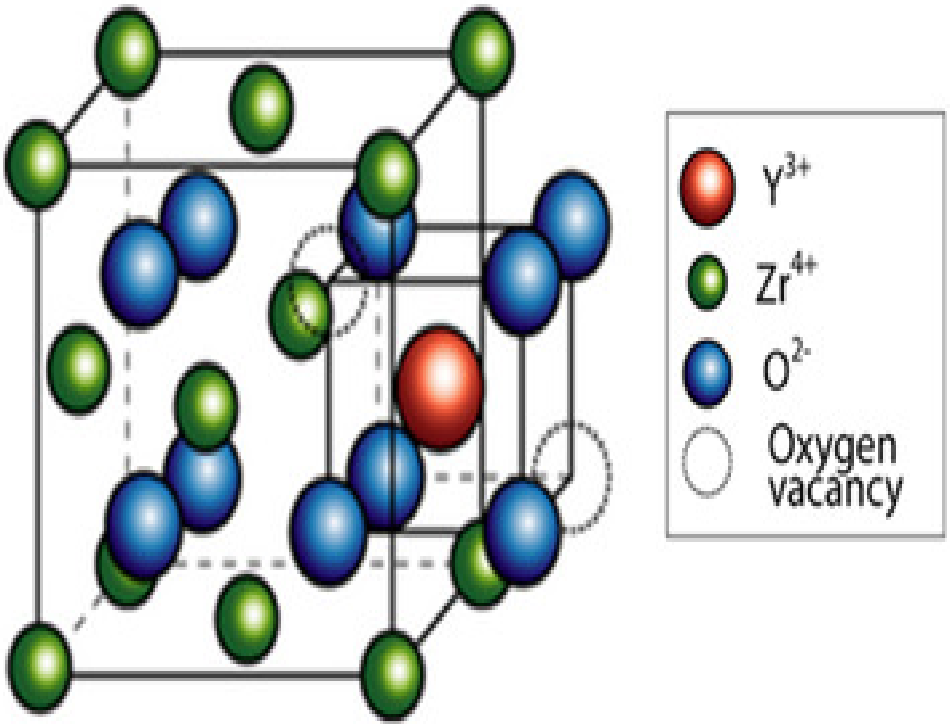

Fig 1.8. Cubic fluorite structure of an YSZ electrolyte.

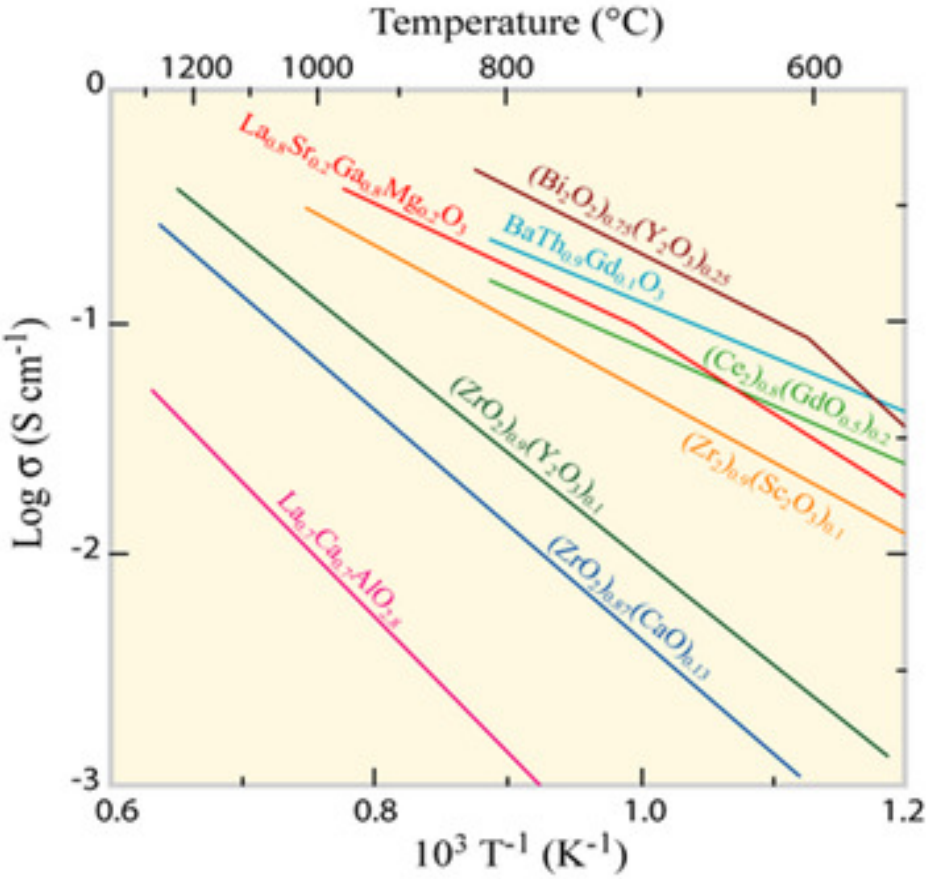

Fig 1.9. Total conductivity of several well-known oxide-ion conductors as a function of the inversed temperature.

1.3.3 Cathode

The cathode in SOFCs must be porous to allow oxygen molecules to reach the electrode/electrolyte interface. Hence the cathode material is very critical since the oxidation reaction determines the overall efficiency of the fuel cell. The most commonly used cathode material is lanthanum manganite ($LaMnO_3$) as a p-type perovskite structure which is typically doped with rare earth elements (e.g., Sr, Ce, Pr) to increase its electrical conductivity. For many years, the perovskite LSM as shown in Fig 1.10 has been considered the state-of-the-art material owing to its suitable properties such as a good electronic conductivity (200~300 S/cm at 900°C) and similar TEC with the electrolyte [29-30]. However, aiming towards the low temperature SOFCs brings in critical problems, for example, decreased oxygen reduction at the cathode, which results in an increased cathode polarization resistance. Many efforts has been studies to diminish the polarization resistance using composite cathodes with electrolyte materials and alternative cathode materials such as $La_{1-x}Sr_xCoO_{3-\delta}$ (LSC) and $La_{1-x}Sr_xCo_{1-y}Fe_yO_{3-\delta}$ (LSCF), which can offer a substantial ionic conductivity of the MIEC material as well as an increase of the active area for the oxygen reduction [31-32]. Particularly, the LSCF material has promising electrocatalytic properties because of the enhanced oxygen diffusion and surface exchange processes by incorporating iron [33-34]. In addition, the TEC of the LSCF cathode closely matches with GDC and YSZ electrolytes. The LSC of cobalt-based materials shows higher ionic and electronic conductivities than other cathodes, i.e., high electrical conductivity, high catalytic activity, high surface area, and compatibility with the electrolyte (and interconnect). Furthermore, there has been

considerable interest in searching for new SOFC cathode materials along with high electronic conductivity and ideally high ionic conductivity like perovskite (e.g., BSCF) or order layered perovskite (e.g., NBCO, PBCO, GBCO) and related (e.g., Ruddlesden-Popper) systems [35-37].

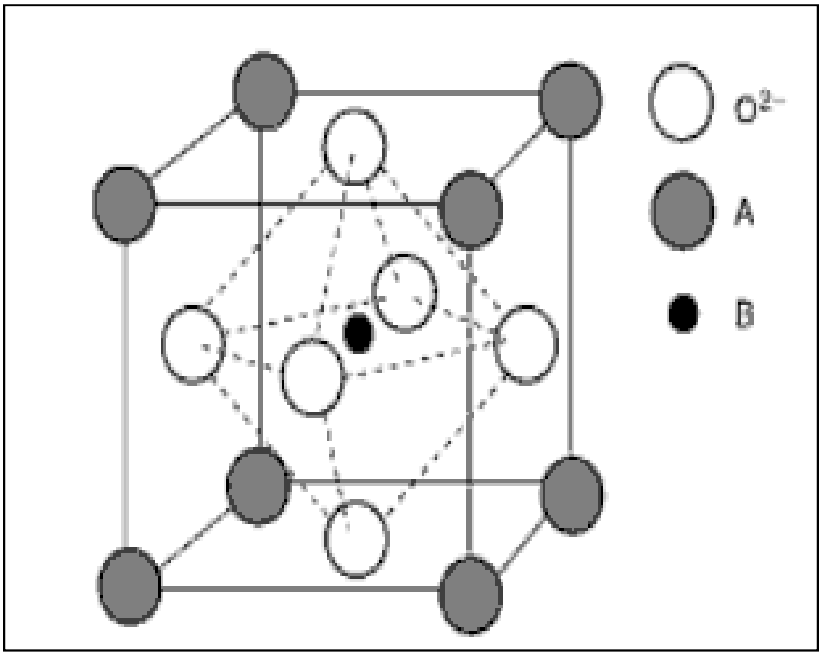

Fig 1.10. The cubic pervoskite structure.

1.4 Current Research Review on Thin Film SOFCs

The current research trend focuses on decreasing operating temperature from 1000°C to lower temperatures to avoid thermomechanical degradation of each component and to use low-cost metallic interconnects. Thin film SOFCs have attracted great research interests, particularly for the solid electrolyte with reduced electrolyte thickness to raise the oxygen conductance with the same material properties. Because the large-scale fabrication techniques such as tape casting and screen printing have some of the limitations for depositing the homogenous thickness of the electrolyte film with a pin-hole defect free. To overcome these restrictions, it is necessary to explore new materials with high ionic conductivity and to process new design microstructures with existing materials, i.e., reducing electrolyte thickness or modifying microstructure for a fast oxygen ion transport and for intermediate temperature SOFCs. First, integrating thin film technology on alternative electrolytes including GDC, LSGM, ScSZ, codoping barium zirconate cerate (BCZY) and so on is the primary focus for intermediate temperature SOFCs [38]. Previously, extensive SOFC research based on the YSZ has been undertaken as the electrolyte conductivity of 0.1 S^{-1} cm was required at 1000°C, thus causing the high temperature SOFC technology. Second, geometrical attempts using lithographic techniques and nanostructured templates such as nanopillars or nanopores were achieved [39]. Since reducing the electrolyte thickness is a direct way to increase oxygen ionic conductivity, it could make overall progress on limiting the cell performance. Third, the grain size effects of nanocrystalline thin films were studied to raise ionic conductivity of electrolyte materials. In nanocrystalline films, the interface

effects might dominate the overall transport mechanisms, and lead to a significant enhancement of the ionic conductivity, e.g., YSZ epitaxial thin films [40], CeO_2 thin films [41-46], and so on. Fourth, implementing multilayers of ionic conducting oxide materials was reported to improve the oxide ionic conductivity. An example of GDC and YSZ multilayers shows an obvious improvement in the oxide ionic conductivity in which the interfacial effect between two different oxides plays an important role in comparison to bulk materials [47]. Finally, an improved ionic conductivity of the electrolyte was conducted based on space charge effects at the interface between two different materials. Two different electrochemical potentials of the materials will be stabilized by interdiffusion of charge carriers, thus balancing their balance bulk charge concentration at the interface area with the extent of the order of the Debye length [48-49]. For example, GDC with Al_2O_3 thin film in the form of nanocomposite is to suppress the enrichment of the predominant electronic conductivity for the reduction of Ce^{4+} to Ce^{3+} [50].

In the cathode's case, the material's electronic conductivity must be with a good catalytic activity under oxidation condition. As addressed, current research is being spotlighted on materials with MIEC properties, which could induce lowering the SOFC operation temperature in a temperature range of 500-700°C. With these materials, the TPB zone is able to extend over the entire area of the cathode those results in a reduced cathode polarization resistance. Several dense thin film cathode materials with well-defined microstructures have been addressed for the study of a fundamental electrochemical reaction by measuring the oxygen surface exchange and bulk diffusion

properties [51, 52-53]. Many authors have reported of new cathode materials with the perovskite structure or related structure including perovskite, Ruddlesden-Popper (RP), and double perovskite structures [54-57]. First, the perovskite material which the A site cation of the ABO_3 structure is a mixture of rare and alkaline earths (e.g., La, Sr, Ca, and Ba) while the B-site cation is reducible transition metal (e.g., Mn, Fe, Co, and Ni). An example of the LSCO epitaxial thin film case shows the oxygen surface exchange as a function of an oxygen partial pressure from an electrical conductivity relaxation measurement and its κ_{chem} value was low in comparison with polycrystalline materials [58]. It was reported that the cation defects/ vacancies and strains are likely to take place in the vicinity of an epitaxial cathode/electrolyte interface, which stabilize more oxygen vacancies as well as improve the oxygen surface kinetics. Furthermore, another perovskite material, $Ba_{1-x}Sr_xCo_{1-y}$ $Fe_yO_{3-\delta}$ (BSCF) epitaxial thin film, also shows high conductivity with different activation energies compared to that of bulk materials [59]. Second, R-P structure is the homologous series of compounds with the general formula $A_{n+1}M_nO_{3n+1}$, which contains two distinct structural units such as the rock salt AO and the perovskite ABO_3). Undoped c-axis oriented $La_2NiO_{4+\delta}$ thin film deposited on $SrTiO_3$ substrate shows an increased electrical conductivity along with the a-b plane as the film thickness decreases [60]. It found that the absolute strain plays an important role on the transport properties in this material, which is related to the structural growth observed from a strained structure to a more relaxed area. Finally, ordered double perovskite structure materials have been presented as the next generation cathode. The first effort on the growth of PBCO thin film deposited by PLD shows high electrical conductivity

and rapid surface exchange kinetics by the electrical conductivity relaxation (ECR) and oxygen IEDP measurements at low temperatures [37]. Other materials such as $NdBaCo_2O_{5+\delta}$ (NBCO) and $GdBaCo_2O_{5+\delta}$ (GBCO) show epitaxial growths by altering deposition temperatures and the laser energy [61-62]. Moreover, some of micro SOFCs (μSOFCs) have been reported they have an epitaxial thin film cathode on single crystal electrolyte substrates to raise the performance of SOFC cathodes [63].

For the anode's case, the thickness in the charge transport processes at the anode generally does not affect on the electrochemical performance of the cells. There are very few experiments dealing with thin film anode in SOFCs since the cell performance is generally unlimited by the anode. Consequently, anode-supported cell is a typical choice for present SOFCs due to its sufficient thickness. Some efforts have been developed in thin film nanocomposite anodes [64-67]. An interesting example of mixed NiO-GDC cermet anode shows thin film nanocomposite structure as a thin diffusion barrier to avoid Ni coarsening over 500°C or additional thin active layer with a porous structure to help the catalytic activity for the hydrocarbon oxidation [68-69]. Other approaches for the anode are conducted to deposit thin films of Pt and Ni metal materials.

1.5 Summary

The SOFC technology is very attractive as the demand of energy generation systems with high efficiency and low emission is increased. The development of intermediate temperature SOFCs is needed for foreseeable industrial applications. As the SOFC operating temperatures, reduces the ohmic loss becomes one of limiting factors for the SOFC efficiency. Great efforts have been focused on alternative electrolyte materials such as GDC, LSGM, and ScSZ to achieve high ionic conductivity for enhancing SOFC performance at low operation temperatures. A further development is made on decreasing of the electrolyte thickness using thin film techniques which can increase its ionic conductivity; therefore, improve the power output of the cells. Furthermore, designing the cathode/electrolyte interface layer is another approach to expand electrochemically active sites around the TPB zone for reducing the cathode polarization resistance in SOFC.

In this aspect, the thesis focused on the following research directions: first, to explore the design of VAN structure interlayer of binary composite materials such as LSCO and PBCO cathodes with GDC electrolyte between the electrolyte and cathode in order to extend the TPB zone and to reduce the TEC; second, to study microstructural and electrical characterics of the GDC thin film as a function of deposition temperature by PLD for thin film SOFC applications, third, to test bilayer electrolytes consisted of GDC and YSZ layer with various thicknesses for preventing electrical current leakage in the GDC layer and chemical, mechanical, and structural integrity in the cell.

CHAPTER II

RESEARCH METHODOLOGY

2.1 Pulsed Laser Deposition (PLD) Techniques

Pulsed laser deposition (PLD) technique was first used for the preparation of semiconductors and dielectric thin films using excimer lasers at lower power densities by Smith and Turner in 1965. Dijkkamp and coworkers have been worked on high temperature superconductors and established characteristics of PLD such as the stoichiometry transfer between target and deposited film, high deposition rates of about 0.1 nm per pulse, and the occurrence of droplets on the substrate surface [70-72]. Today, PLD technique is one of the greatest growing thin-film processes for all kinds of oxides, nitrides, or carbides, and also for preparing metallic systems and polymers or fullerenes in multicomponent films. That can be used for many potential applications, from integrated circuits and optoelectronics to micromechanics and medical implants.

PLD is a thin film deposition technique which is prepared by the ablation of one or more targets illuminated by a focused pulsed-laser beam. The basic setup is relatively simple to many other deposition techniques although the physical phenomena of laser target interaction and film growth are quite complex. Fig 2.1 shows a schematic diagram of the PLD setup [73]. The target is oriented at 45º angle of incident laser beam. While the laser beam is absorbed by the target, the energy is transformed to electronic excitation and then into thermal, chemical and mechanical energy which results in evaporation, ablation, plasma formation and exfoliation. The ejected species spread out

the surrounding vacuum in the formation of a plume containing many species such as atoms, molecules, electrons, ions, clusters, and particulates. The evaporated material is deposited on a substrate placed parallel and at a distance of approximately 3-5 cm away from the target. The substrate temperature can be varied from room temperature to 800°C. The film quality depends on a variety of parameters including laser density, deposition temperature, pulse repetition rate, pressure in the chamber and substrate to target distance. The major advantage of PLD that it is possible to prepare stoichiometric thin films from a single alloy bulk target i.e., stoichiometry transfer between target and substrate has made the PLD technique interesting for the growth of complex systems, such high-temperature superconductors, and piezoelectric. Despite the advantages of PLD, there are some obstacle remains. PLD produces fine particulates chunks of target material ranging in size from microns down to submicron dimensions in some materials. In addition, the feature limitation in mass production is due to the substrate surface coverage of the plum is created by the adiabatic expansion of laser plasma.

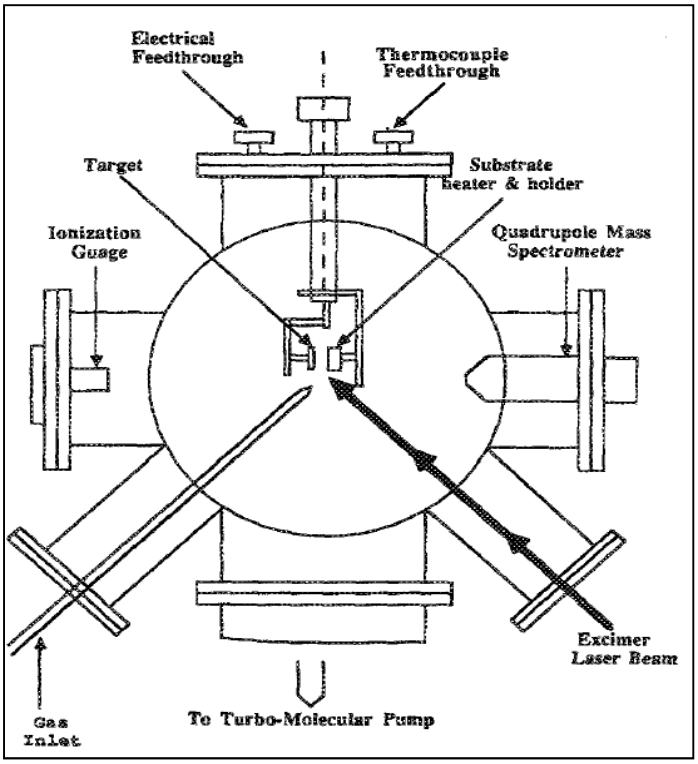

Fig 2.1. Schematic diagram of the pulsed laser evaporation (PLD) system for deposition [71].

The physical and theoretical principles of PLD have described by Singh et al. and each of laser target interactions with a solid during short pulsed laser period as shown in Fig 2.2. It depends on the kinds of the laser beam with laser target interaction can be classified into three regimes: (1) the interaction of the laser beam with the target material results in evaporation of the surface layers, (2) the interaction of the laser beam with the evaporated material leads to the formation of a high temperature iso-thermal expanding plasma composing of a positive charge and neutral particles, molecules, atoms, and other regimes, and (3) the anisotropic three dimensional adiabatic expansion of the laser

generated plasma giving increase to the characteristic of the deposition. The first two regimes begin from the laser pulse to laser pulse duration, the third regime starts right after the laser pulse terminates.

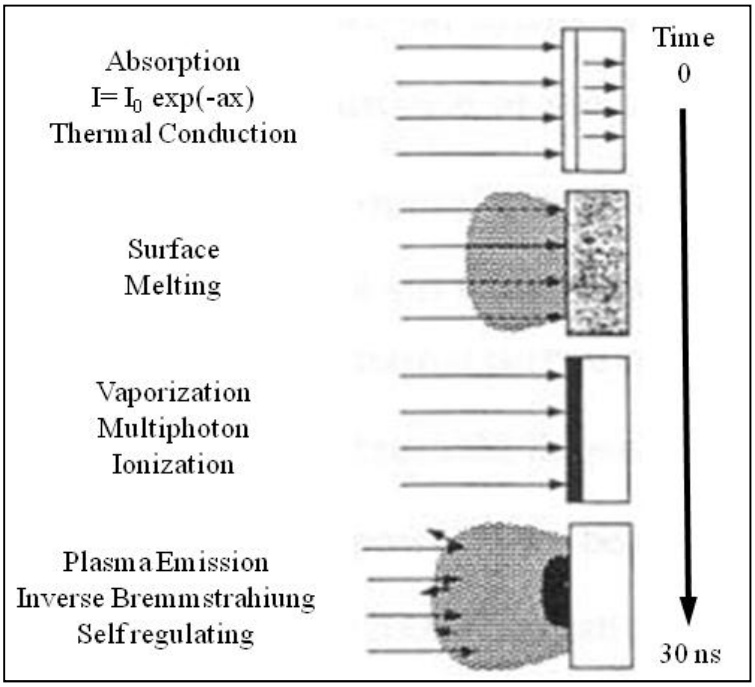

Fig 2.2. The stage of laser target interactions with a solid during short pulsed laser period [71].

2.1.1. Interaction of Laser Beam with the Bulk Target

The interaction of the laser beam with the solid is significant to understand the thermal effects generated by the intense nanosecond excimer laser radiation. These interactions can be separated into two parts. First, the laser beam interacts with the bulk target. Second, the laser beam interacts with the evaporated material from the bulk target

material. The main part deals with plasma formation, heating, and deposition of the evaporated species. The elimination or sputtering of the material from the target by laser irradiation depends on the laser beam with the solid. During the pulsed laser irradiation, the thermal history parameters such as heating rate, melting, and evaporating relies on the laser parameters (pulse energy density E, pulse duration τ, shape, and wavelength), and the temperature dependent optical (reflectivity, absorption coefficient) and thermophysical (heat capacity, density, thermal conductivity) properties in the material. The heating and melting effects of the pulsed laser irradiation involves the key of a three-dimensional heat flow which can be estimated by a one-dimensional heat flow equation with suitable boundary conditions taking into account the phase change in the material. The estimation can be presented as the following equation.

$$\rho_i(T)\, C_p(T)\, \frac{\partial T(x,t)}{\partial t} = \frac{\partial}{\partial t}\left(K_i(T)\, \frac{\partial T_i(x,t)}{\partial x}\right) + I_0(T)\,\{1 - R(T)\}\, e^{-a(T)x} \qquad (2.1)$$

Where χ is direction perpendicular to the sample, t is time, i = 1, 2 refers to the solid and liquid interface, respectively, $\rho_i(T)$ is temperature dependent density, $C_p(T)$ is thermal heat capacity per unit mass of the target material, $R(T)$ is temperature dependent reflectivity, $a(T)$ is absorption coefficient at the laser wavelength, $I_0(T)$ is time dependent incident laser intensity, and K_i is thermal conductivities of solid and liquid phases at the interface.

To understand the thermal characteristics of the pulsed laser irradiation instead of detailed computer calculation, the presence of a moving interface as a results of melting

or evaporation, and time and time dependent optical and material properties precludes analytical solutions, and numerical solutions such the finite different methods have to be adopted to count the evaporation characteristics of the pulsed laser irradiated materials. The use of simple energy balance considerations, the amount of material evaporated per pulse is calculated. The energy deposited by the laser beam on the target is same to the energy needed to vaporize the surface layers plus conduction losses by the substrate and the absorption loss by the plasma that is given by the energy threshold E_{th} represents as the minimum energy above which suitable evaporation is observed. The heat balance equation is as follows.

$$\Delta x_i = \frac{(1-R)(E-E_{th})}{\Delta H + C_v \Delta T} \tag{2.2}$$

where Δx_i is thickness of evaporated material, ΔH is latent heat of vaporization, $R$is reflectivity, C_v is volumetric heat capacity, and ΔT is maximum temperature rise. This equation is very clear for conditions where the thermal diffusion distance $(2D_\tau)^{1/2}$ is larger than the absorption length of the laser beam in the target material,$1/\alpha_t$.

2.1.2. Interaction of Laser Beam with Evaporated Material

The high surface temperature of ~2000K leads to the interaction of nanosecond high power laser beams with the bulk target material that results in emission of positive ions and electrons form the surface. This can be presented by the Richardson's equation which shows an increase of an exponential in electron emission as a function of temperature. The thermionic emission of positive ions can be calculated by the Langmuir-Saha equation which exhibits a similar relation with temperature as the electron emission. This equation is expressed as

$$\frac{i_+}{i_0} = \left(\frac{g_+}{g_0}\right) exp^{\phi - I/KT}, \tag{2.3}$$

Where i_+ and i_0 are the positive and neutral ion fluxes, $T$is temperature, $g_+$and g_0 represent the statistic weight of the positive ionic and neutral states, ϕ is the electron work function, and I is the ionization potential of the material coming from the target surface. The fraction of the ionized species increases with rising temperature since $I > \phi$.

Therefore, the high temperatures can be induced in the evaporated plasma by the interaction of the laser beam with the material even through the surface temperature of the target is close to the vaporization temperature. The penetration and absorption of the laser beam in the plasma depends on the electron and ion density, temperature, and the wave length of laser light. The penetration or reflection of the incident laser beam relies on the plasma frequencyV_p , which need to be lower than the laser frequency. For

example, the laser frequency corresponds to $9.74 \times 10^{14}\,\mathrm{s}^{-1}$ for the excimer laser wavelength (λ = 308nm). The plasma frequency is given by

$$V_p = 8.9 \times 10^3 n_e^{0.5} \tag{2.4}$$

where n_e is the electron concentration in the plasma. Using this equation, the critical electron density for reflection of the beam by the plasma is found to be $1.2 \times 10^{22}\,\mathrm{cm}^{-3}$ which value is very close to the concentration of atoms present in a solid or liquid.

$$\alpha_p = 3.69 \times 10^8 \left(\frac{Z^3 n_i^2}{T^{0.5} v^3}\right) \left[1 - e^{-hv/KT}\right] \tag{2.5}$$

where Z is the average charge, n_i is ion density and *T is* temperature of the plasma, *h* is the Planck constant*, K* is Boltzmann constant*,* and v is frequency of the laser light. If (α_px) is large, the laser energy is highly absorbed, where *X* is the dimension perpendicular to the target of the expanding plasma. This equation shows that the absorption coefficient of the plasma is proportional to *nT*. Accordingly, the plasma absorbs the incident laser radiation very closed distances to the target i.e., the density of ionized species is high. The term $\left[1 - e^{-hv/KT}\right]$ presents the losses based on stimulated emission which depends on the plasma temperature and the laser wavelength. For example, the excimer laser wavelength *(A* = 308 nm), the exponential term becomes accord for *T* <40,000 K and can be approximated by hv/KT for T>40,000 K. The

absorption period shows a $T^{-3/2}$ temperature dependence at high temperatures (T>40,000 K) and $T^{0.5}$ dependence at low temperatures (T <40,000 K) Then, the frequency variation of the absorption coefficient changes from v^2 to v^3based on the hv/KT value. Because of the high expansion velocities of the leading plasma edge, the electron and ion densities decline very rapidly with time, thus making the plasma transparent to the laser beam. As the plasma is constantly augmented at the inner edge by the evaporated target material during the time of the laser pulse, a high density of ions is produced next to the surface of the target, which is constantly absorbing the laser radiation during the time interval of the laser pulse, while the outer border of the plasma is transparent to the laser beam. Fig 2.3 shows a schematic diagram of the laser interaction with the plasma target based on these observations. It shows that the four regions during the incidence of the laser pulse which can be distinguished: (1) unaffected bulk target, (2) evaporating target surface, (3) area near the surface absorbing the laser beam, and (4) quickly expanding outer edge that is transparent to the laser beam. It is reasonable to assume that during the time of the laser pulse for PLD deposition, an isothermal temperature is reached near the target surface. A dynamic equilibrium exists between the plasma absorption coefficient and the rapid transfer of thermal energy into kinetic energy. These two mechanisms control the isothermal temperature achieved by the plasma. At even higher energy densities when appreciable amount of energy is absorbed by the plasma, a self-regulating mechanism exists near the target surface. During the isothermal regime and assuming an initial expansion velocity of 10^5~10^6 cm/s, the perpendicular dimension of the plasma is in the order of 10^{-3} ~ 10^{-2} cm at the

end of 30 nsec laser pulse. The rapid expansion of the plasma in vacuum occurs due to the density gradients in the plasma. This plasma represents a heated high-pressure gas kept in small dimensions and then suddenly allowed to expand in vacuum. Fig 2.4 shows the schematic diagram of the density, pressure, and velocity profiles in the plasma. It presents that the inner edge of the plasma, density is at a maximum as the velocity is at a minimum. Moreover, the expansion velocities rise, the acceleration begins to reduce and become zero which results in a similar elongated plasma shape.

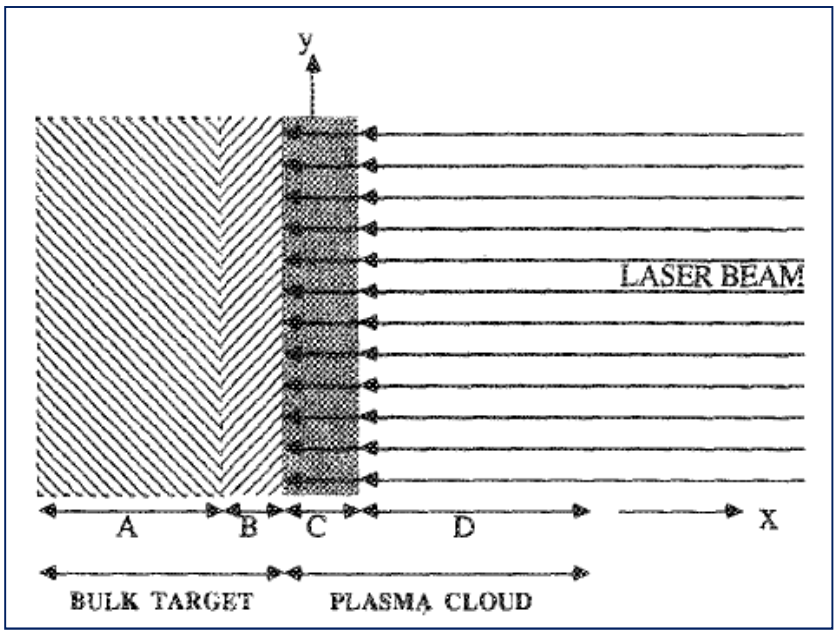

Fig 2.3. Schematic diagram showing the different phases present during irradiation of a laser on a bulk target: (A) unaffected bulk target, (B) evaporated target material thickness, (C) dense plasma-absorbing laser radiation, and (D) expanding plasma transparent to the laser beam [71].

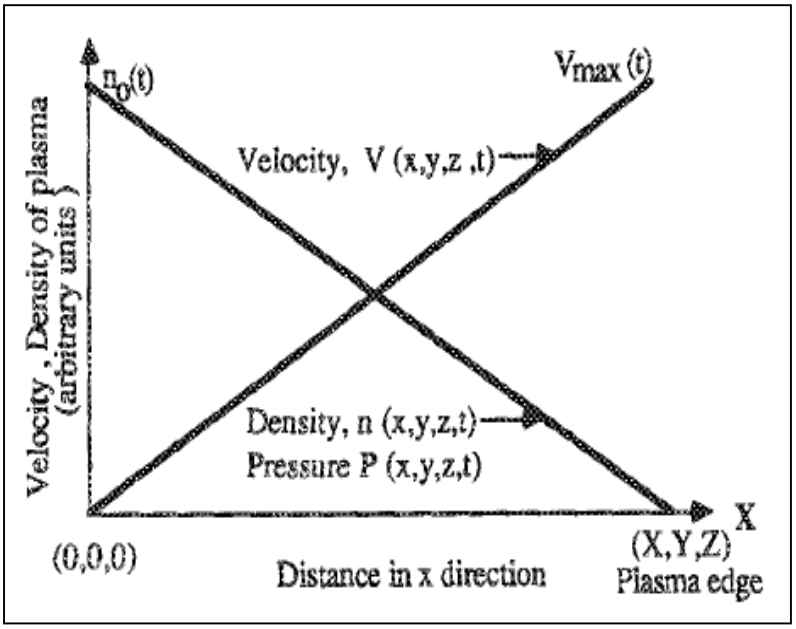

Fig 2.4. Schematic diagram showing the density *(n),* pressure *(P),* and velocity profile *(V)* employed in the model. The density and pressure in the plasma are maximum at the inner central edge of the plasma, while the velocity is maximum at the outer edge [72].

2.1.3 Adiabatic Plasma Expansion and Thin Film Deposition

The adiabatic expansion of the plasma in vacuum pulse gives rise to the characteristics of PLD. After the termination of the laser pulse, there is not any additional input in the number of particles injected into the plasma from the target; nor is there no absorption of laser energy. Hence an adiabatic expansion occurs where the temperature can be related to the dimensions of the plasma by a thermodynamic relation given by

$$T[X(t)\,Y(t)\,Z(t)]^{\gamma-1} = const \qquad (2.6)$$

In this equation, r corresponds to the ratio of the specificheat capacities at constant pressure and volume. During the adiabatic regime, the thermal energy shows a fast conversion to kinetic energy with the plasma, attaining extremely high expansion velocities. A rapid temperature drop occurs as the spherical plasma expands; however, the temperature will not continue to fall off as (radius) ^{2} because the cooling will be equilibrium by the energy regained from the recombination process of the ions. The temperature drop will be slow because of the preferential expansion of the plasma in one direction. As the plasma expands, the pressure decreases rapidly until the most thermal energy is transferred into kinetic energy, so there is no more energy left for the expansion process. Finally, the plasma becomes extended in the shorter dimensions and holds its profile while the deposition process. This is shown schematically in Fig 2.5, where initially the plasma is el1iptical in shape with the *z* direction being its major axis, the plasma still preserves an elliptical appearance after adiabatic expansion; however the major axis corresponds to the *z* direction.

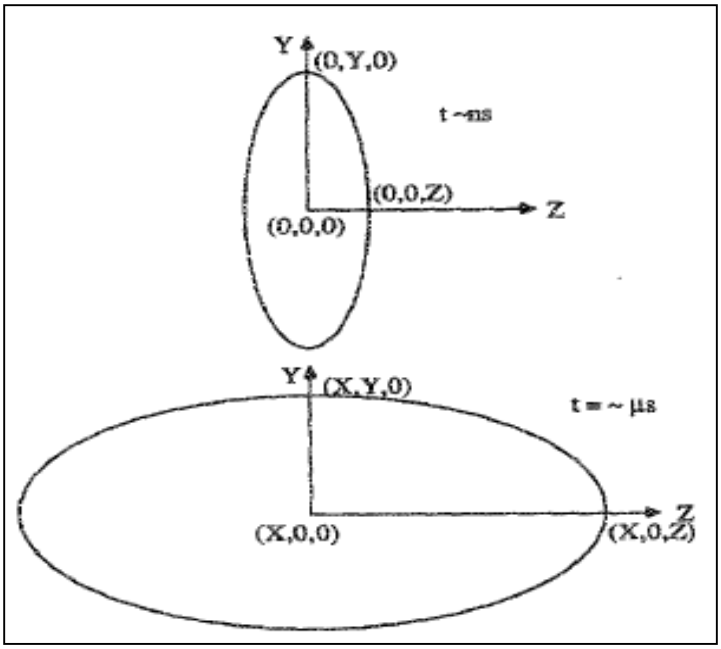

Fig 2.5. *(a)* Schematic diagram to show the initial elliptical shape of the plasma just after tennination of the laser pulse. (b) Final shape of the plasma before it strikes the substrate. The major and minor axes have reversed in the two cases [72].

2.2 Thin Film Crystal Structure Analysis

For the analysis of thin film properties in this dissertation, X-ray diffraction (XRD), atomic force microscope (AFM), and scanning electron microscope (SEM), and transmission electron microscopy (TEM) were performed to understand microstructural characteristics of thin films in SOFCs. In order for optimal device performance, the films should possess specific physical, electrical, electrochemical properties which are strongly influenced by the microstructural qualities of the films such as crystalline or epitaxial, crystallographic orientation, crystallite size, strain and defect. Hence, microstructural characterization of thin films is extraordinarily important for the design and improvement of cell performance.

2.2.1 X-ray Diffraction

XRD is a versatile and non-destructive analytical technique that reveals information about the crystallographic structure, chemical composition, and physical properties of materials and thin films [74-75]. This technique is based on observation of the scatter intensity of an X-ray beam hitting a sample as a function of incident and scattered angle, polarization, and wavelength. X-rays are electromagnetic radiation with typical photon energies in the range of 100 eV - 100 keV. Only short wavelength x-rays in the range of a few Å to 0.1 Å (1 keV - 120 keV) are used for diffraction applications. Since the wavelength of x-rays is as good as to the size of atoms, they are ideally matched for probing the structural arrangement of atoms and molecules in a wide range of materials. The energetic x-rays can penetrate into the materials and provide

information about the bulk structure. X-rays are generated by either x-ray tubes or synchrotron radiation. The x-ray tube as primary x-ray source used in laboratory x-ray instruments, x-rays are generated when a focused electron beam accelerated across a high voltage field attacks a stationary or rotating solid target. As electrons have a collision with atoms in the target and slow down, a continuous x-rays spectrum are emitted, which is termed Bremsstrahlung radiation. The high energy electrons emit inner shell electrons in atoms during the ionization process. An x-ray photon with energy characteristic of the target material is emitted when a free electron fills the shell. Common targets used in x-ray tubes such as Cu and Mo that emit 8 keV and 14 keV x-rays with corresponding wavelengths of 1.54 Å and 0.8 Å, respectively.

There are Several X-ray diffraction techniques.

(1) Single crystal X-ray diffraction is used to solve structure of crystalline materials ranging from inorganic solids to complex macromolecules such as proteins or polymers. Although obtaining single crystals is difficult, single crystal X-ray crystallography is a primary method for determining the molecular conformations of biological interest such as DNA, RNA and proteins.

(2) Power X-ray diffraction is used to characterize crystallographic structure, grain size, and preferred orientation in polycrystalline or powder solid samples which is a preferred method of analysis for characterization of unknown crystalline materials. Compounds are identified by comparing diffraction data against a database of known materials. Powder diffraction is also a common method for determining strains in crystalline materials.

(3) Thin film diffraction and grazing incidence X-ray diffraction may be used to characterize the crystallographic structure and preferred orientation of substrate-anchored thin films.

(4) High-resolution X-ray diffraction is used to characterize thickness, crystallographic structure, and strain in thin epitaxial films. It employs parallel-beam optics.

X-rays mainly interact with electrons in atoms. When x-ray photons collide with electrons, some photons from the incident beam will be deflected away from the direction. The scattered x-rays carry information about the electron distribution in materials. On the other hand, in the inelastic scattering process, x-rays transfer some of their energy to the electrons and the scattered x-rays will have different wavelength than the incident x-rays. Diffracted waves from different atoms can interfere with each other and the resultant intensity distribution is strongly modulated by this interaction. If the atoms are arranged in a periodic fashion, as in crystals, the diffracted waves will consist of sharp interference maximum peaks with the same symmetry as in the distribution of atoms. Finally, measuring the diffraction pattern allows us to infer the distribution of atoms in a material. The peaks in an x-ray diffraction pattern are directly related to the atomic distances. Fig 2.6 shows the relationship describing the angle at which a beam of X-rays of a particular wavelength diffracts from a crystalline surface was discovered by Sir William H. Bragg and Sir W. Lawrence Bragg and is known as Bragg's Law [76]. The atoms represented as spheres in the graph, can be seen as forming different sets of planes in the crystal. For a given set of lattice planes with an inter-plane distance of d, the condition for a diffraction to occur can be simply written as

$$2d\ sin\theta = n\lambda, \tag{2.7}$$

where λ= wavelength of the x-ray, θ = scattering angle, n = integer representing the order of the diffraction peak, and d is inter-plane distance of atoms, ions, and molecules. That equation is known as the Bragg's law, which is one of most important laws used for interpreting x-ray diffraction data. It is important to note that the law holds true if the atoms are replaced by molecules or collections of molecules, such as polymers, colloids, proteins and virus particles.

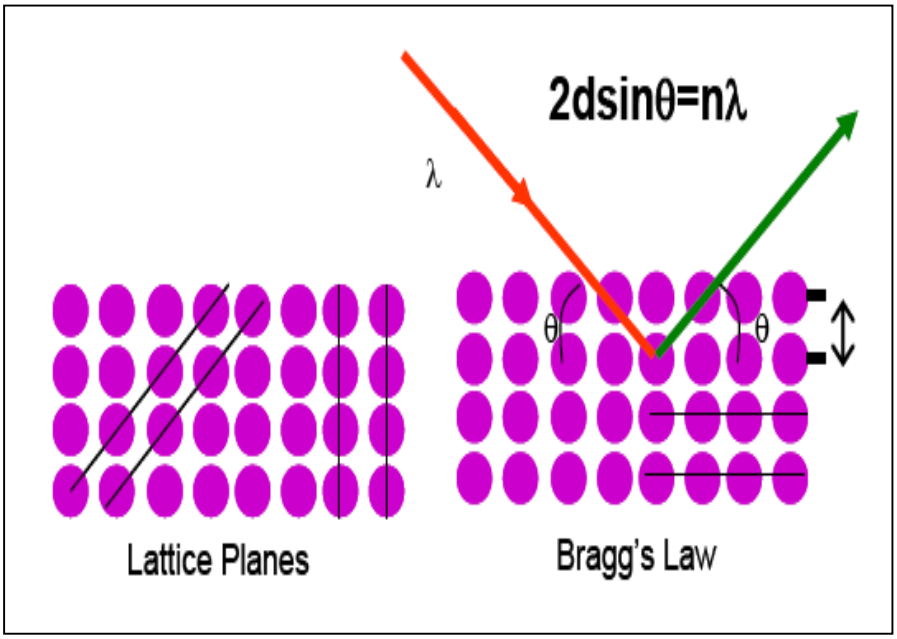

Fig 2.6. The Bragg's law: (a) A two dimensional periodic array of atoms in the crystal, (b) the Bragg's Law [76].

2.2.2 Atomic Force Microscope (AFM)

To observe the grain morphologies and grain size of the surface in the film, Atomic force microscopy (AFM) is achievable. AFM is a very high-resolution type of scanning probe microscope, with demonstrated resolution of fractions of a nanometer, more than 1000 times better than the optional diffraction limit [77]. Because AFM is one of the primary tools for imaging, measuring and manipulating matter at the nanoscale and has some advantages as an imaging tool in biology and physics. It is not only AFM achieve molecular resolution but also can be performed under fluids permitting samples to be imaged in near native conditions. Furthermore, the AFM works by scanning a fine ceramic or semiconductor tip over a surface as a phonograph needle scans a record.

Fig 2.7 shows the schematic of the AFM. For the operation of the AFM, the tip is positioned at the end of a cantilever beam shaped much like a diving board. As the tip is repelled by or attracted to the surface, the cantilever beam deflects. The magnitude of the deflection is captured by a laser that reflects at an oblique angle from the end of the cantilever. A plot of the laser deflection versus tip position on the sample surface provides the resolution of the hills and valleys that constitute (tip touching the sample) and tapping mode (the tip can tap across the surface) [78]. First, the contact mode is also known as repulsive mode; an AFM tip makes soft “physical contact” with the surface. The tip is attached to the end of a cantilever with a low spring constant, lower than the effective spring constant holding the atoms of the sample together. As the scanner gently traces the tip across the sample, the contact force causes the cantilever to bend to

accommodate changes in topography. This is useful for small, high-speed atomic resolution scans, and is known as variable-deflection mode because the tip is in hard contact with the surface, the stiffness of the lever needs to be less that the effective spring constant holding atoms together, which is on the order of 1 – 10 nN/nm. Most contact mode levers have a spring constant of < 1N/m. Second, the tapping mode is large vibrations of the probe i.e., the cantilever is driven to oscillate up and down at near its resonance frequency by a small piezoelectric element mounted in the AFM tip holder similar to non-contact mode for imaging. However, the amplitude of this oscillation is greater than 10 nm, typically 100 to 200 nm. It allows for measurements to be made at ambient conditions. While the oscillating probe hits the sample, its short-time interactions with minimal shear are less destructive than the contact mode. To identify a type of tip-sample force, e.g. attractive or repulsive, recording of the phase behavior of the AFM probe can be used. The tapping mode at small amplitudes operation is illustrated by attractive tip-sample forces and overlaps with operation in noncontact mode.

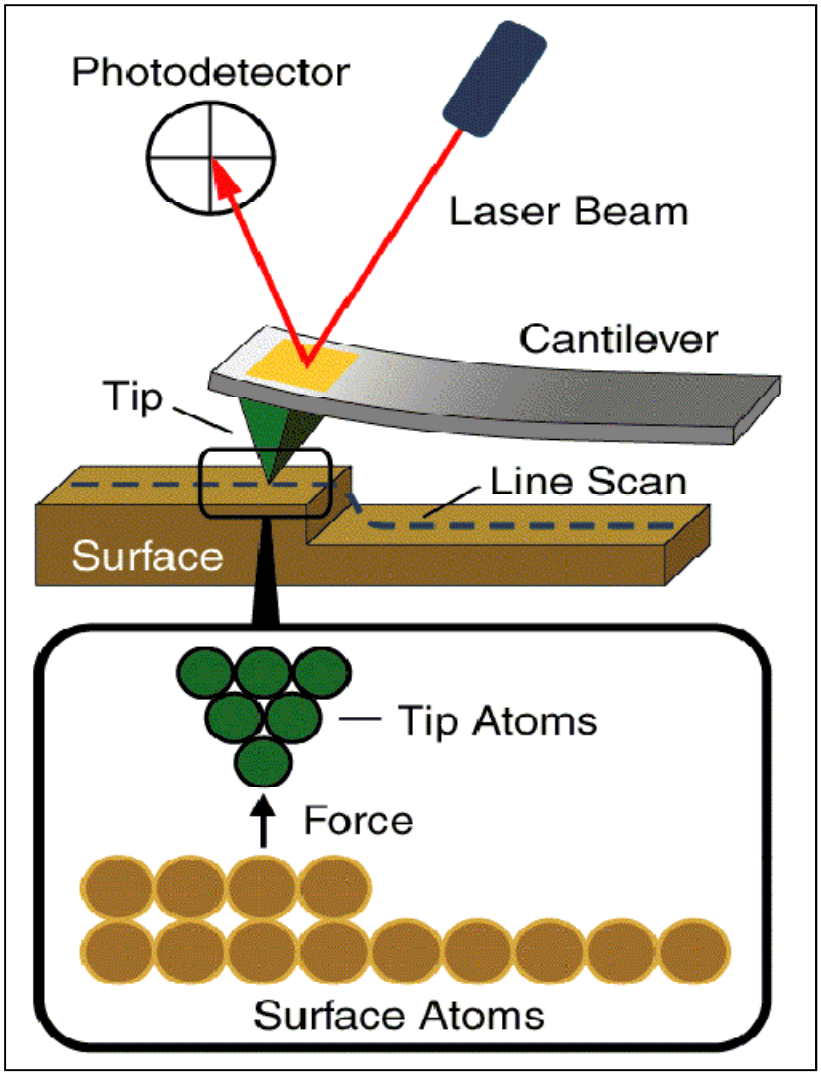

Fig 2.7. Schematic diagram of the AFM [78].

2.2.3 Scanning Electron Microscope (SEM)

The scanning electron microscope (SEM) uses a focused beam of high energy electrons to generate various signals at the surface of solid specimens. The signals that derive from electron sample interactions reveal information about the sample such as texture, chemical composition, and crystalline structure. For the fundamental principal of SEM, accelerated electrons take significant amounts of kinetic energy, and this energy is dispersed as a variety of signals generated by electron sample interactions as the incident electrons are decelerated in the solid sample. These signals contain secondary electrons for producing SEM images, backscattered electrons (BSE), and diffracted backscattered electrons (EBSD) for determining crystal structures and orientations of minerals, photons, visible light (cathodoluminescence) and heat. Among them, secondary electrons and backscattered electrons are commonly used for imaging samples: First, secondary electrons are most valuable for showing morphology and topography on samples. Second, backscattered electrons are most valuable for illustrating contrasts in composition in multiphase samples i.e. for rapid phase discrimination. X-ray generation is produced by inelastic collisions of the incident electrons with electrons in discrete orbital (shells) of atoms in the sample. Since the excited electrons return to lower energy states, they yield X-rays that are of a fixed wavelength which is related to the difference in energy levels of electrons in different shells for a given element. Hence, characteristic X-rays are produced for each element in a mineral that is excited by the electron beam. SEM analysis is considered to be non-destructive that x-rays generated by electron interactions do not lead to volume loss of the sample, so it is possible to analyze the

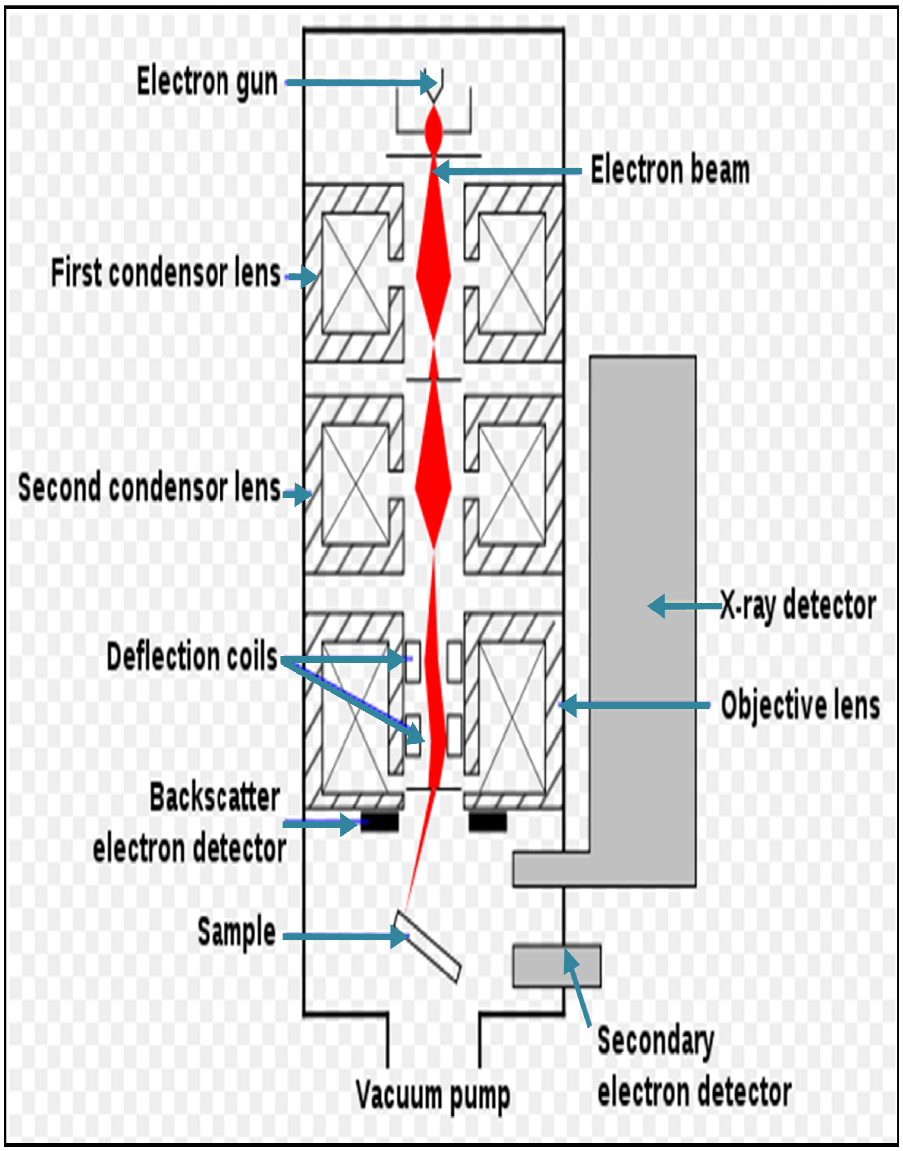

Fig 2.8. Schematic diagram of SEM equipment.

same materials repeatedly. Fig 2.8 shows schematic diagram of an SEM equipment. In most applications, data are collected over a selected area of the surface of the sample, and a 2-dimensional image is generated that displays spatial variations in these properties. Areas ranging from approximately 1 cm to 5 microns in width can be imaged in a scanning mode by traditional SEM techniques (magnification ranging from 20X to approximately 30,000X, spatial resolution of 50 to 100 nm). The SEM is available of performing analyses of selected point locations on the sample which are particularly useful in qualitatively or semi-quantitatively determining chemical compositions using EDS, crystalline structure, and crystal orientations with EBSD [79].

2.2.4 Transmission Electron Microscopy (TEM)

Transmission Electron Microscopy (TEM) is capable of displaying magnified images in the range 10^3 to 10^6 for a thin specimen and useful for analyzing the properties of a crystalline specimen. TEM uses electrons instead of light as light source and their much lower wavelength makes it possible to get such a high resolution images. It provides information about the microstructural features having sizes from nanometers to microns and controlling many important properties of materials [80]. The basic operation of the TEM is like a slide projector. A projector shines a beam of light which transmits through the slide. The patterns painted on the slide only allow certain parts of the light beam to pass through. Accordingly, the transmitted beam reproduces the patterns on the slide, forming an enlarged image of the slide while falling on the screen. Besides diffraction and spatial imaging, the high energy electrons in TEM cause

electronic excitations of the atoms in the specimen. Analytical TEM uses two types of spectrometries to obtain chemical information from electronic excitations:

- In energy dispersive x-ray spectrometry (EDS), and x-ray spectrum is acquired from small areas of the specimen enlightened with a focused electron beam, usually using a solid- state detector. Characteristic x-rays from the chemical elements are used to determine the concentrations of the different elements in the specimen.
- In electron energy loss spectroscopy (EELS), energy losses of the electrons are measured after high energy electrons have traversed the specimen.
- Information on local chemistry and structure is attained from the features in EELS spectra caused by 50 excitations and core electron excitations.

Fig. 2.9 shows a block diagram of a TEM. A recent TEM have the ability of imaging the variations in diffraction across the specimen (diffraction contrast imaging), imaging the phase contrast of the specimen (high-resolution imaging), obtaining diffraction patterns from selected areas of the specimen, and performing EELS and EDS spectroscopy measurements with a small, focused electron beam. Due to its high capability, TEM has become a major analysis method in a range of scientific fields, in both physical and biological sciences and its applications are in cancer research, virology, materials science as well as pollution and semiconductor research [81].

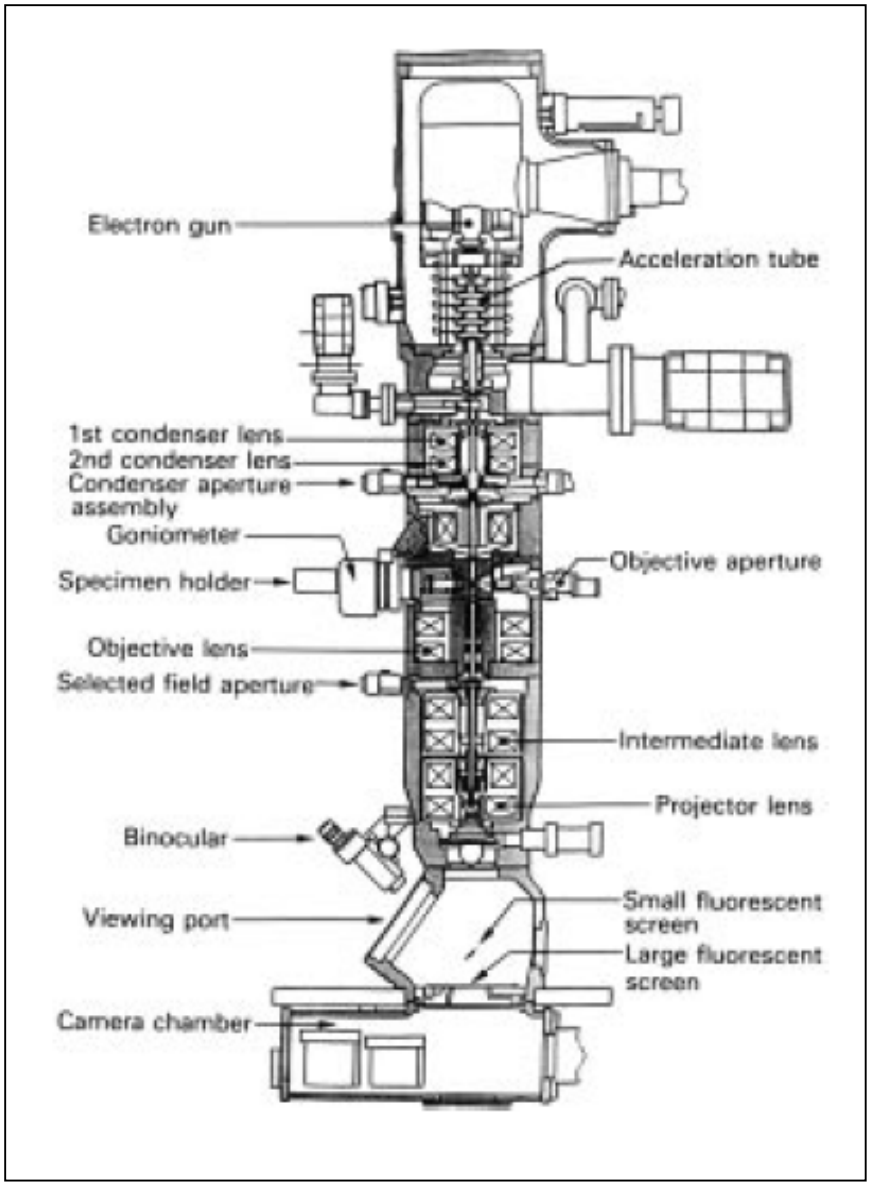

Fig 2.9. A block diagram of a TEM [81].

2.3 Electrochemical Analysis

Solid materials are conventionally characterized by elemental analysis, x-ray diffraction, spectroscopy and microscopic techniques. Among them, electrochemistry analysis is a complementary and versatile tool for solid state characterization. Solid state electrochemistry techniques have been important for the study of intercalation process for battery material, but also are applied to a wide range of solid materials. Additionally, electrochemistry can offer further analytical information, allowing the identification of structural features or distinct solid phases, the presence of different solid species, and composition of the solid. Here, AC impedance, electrical conductivity, and IV measurement is discussed in the following section.

2.3.1 AC Impedance Spectroscopy

AC impedance spectroscopy or electrochemical Impedance Spectroscopy (EIS) has many advantages in comparison with other electrochemical methods. AC impedance is a non-destructive method for the evaluation of a wide range of materials, including coatings, anodized films, corrosion inhibitors, and batteries and fuel cells and can give detailed information of the systems under examination. By applying a small sinusoidal ac signal (typically a few millivolts), the ac response from the cell over a range of applied frequencies can be analyzed [82]. The resultant data are plotted in the complex plane (Nyquist plot) in Fig 2.10 (b) or as magnitude and phase versus frequency (Bode plot) which can be fitted by the equivalent circuit shown in Fig 2.10 (a). This simple model circuit is commonly applied to electrochemical systems in which contact

resistance and other effects are quite small to ignore. For simplicity, assume that the polarization resistance of one electrode is much larger than that of the other electrode, so that one can legitimately omit circuit elements associated with one of the electrodes. Polarization resistance is the reaction equivalent, double-layer capacitance is the interfacial capacitance of the cathode, and the ohmic resistance is the resistive component of the fuel cell to be evaluated. The voltage source element is an ideal DC voltage source (zero internal impedance and constant voltage) with a potential equal to the open circuit voltage of the fuel cell. The voltage source element does not affect AC analysis although allows the model to approximate the DC behaviour of the fuel cell.

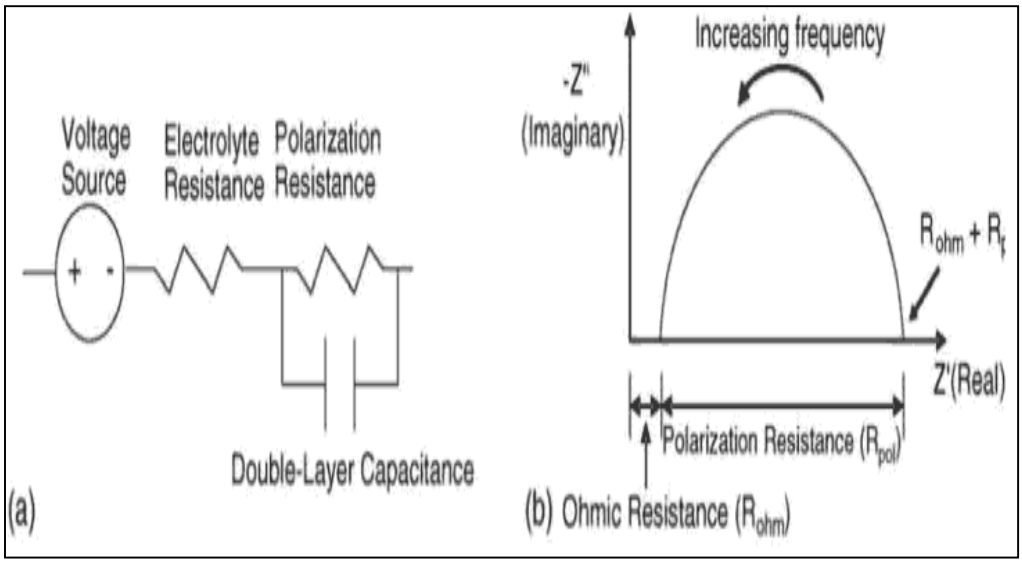

Fig 2.10. AC impedance of (a) Simplified, idealized equivalant circuit in fuel cells (b) Nyquist plot [83].

For the electrical property of the electrolyte using AC impedance in this dissertation, the electrochemical cells for were prepared with the in-plane configuration. Two rectangular platinum strips (Heraeus CL11-5100, Pt ink) on the thin film were prepared by screen printing method and platinum grids were used as current collectors. Total conductivity of thin film electrolytes was conducted using AC impedance measurement in the frequency range of 10^{-1} – 30MHz from 300 to 700 ºC in air.

2.3.2 Electrical Conductivity Measurement

The electrical conductivity of thin films is measured with a four probe point by the Van der Pauw method. Its power lies in its ability to accurately measure the properties of a sample of any arbitrary shape and the electrodes are placed on its perimeter [81~84]. To make the resistivity measurement, a current is caused to flow along one edge of the sample (e.g., I_{12}) and the voltage across the opposite edge (e.g., V_{34}) is measured. From these two values, a resistance (for this example, $R_{12,34}$) can be found using Ohm's law:

$$R_{12,34} = \frac{V_{34}}{I_{12}} \tag{2.8}$$

Van der Pauw discovered that the sheet resistance of samples with arbitrary shape can be determined from two of these resistances - one measured along a vertical edge, such as $R_{12,34}$, and a corresponding one measured along a horizontal edge, such as $R_{23,41}$ as

shown in Fig 2.11. The actual sheet resistance is related to these resistances by the Van der Pauw formula two characteristic resistances RA and RB [84]:

$$e^{-\pi R_{12,34}/R_S} + e^{-\pi R_{23,41}/R_S} = 1 \quad (2.9)$$

this can be solved numerically for RS.

Thus, the specific resistivity of the sample can be calculated as

$$\rho = R_s \mathrm{d} = \frac{\mathrm{I}}{\mathrm{V} \cdot \mathrm{đ}} \quad (2.10)$$

where *I* is the applied current, *V* is the measured voltage, and *d* is the sample thickness.

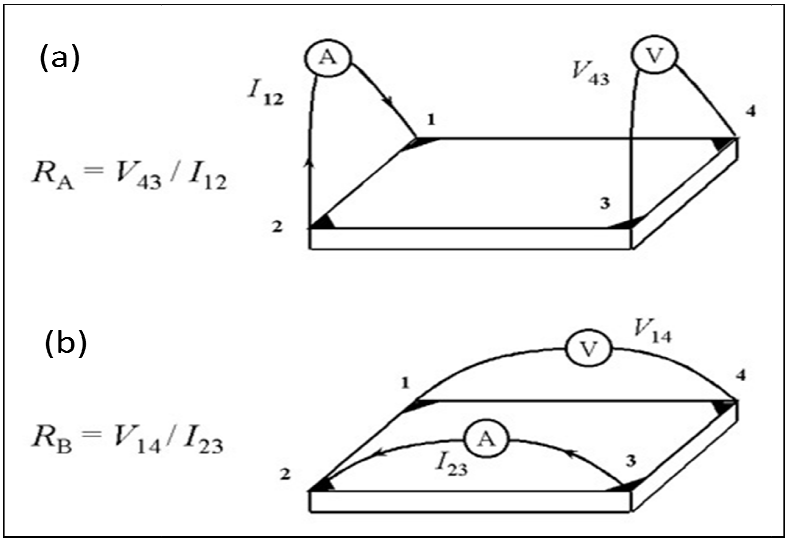

Fig 2.11. Schematic of a Van der Pauw which can be solved numerically for *R*S [84].

2.3.3 Single Cell Power Measurement

Anode-supported single cell performance was conducted with YSZ/GDC bilayer electrolyte or vertically aligned nanocomposite LSCO/GDC interlayer and PBCO/GDC interlayer. The bilayer electrolyte or interlayer was deposited on the anode disks of NiO/GDC or NiO/YSZ under varying oxygen partial pressure with a KrF excimer laser (Lambda Physik 210, λ = 248 nm, 2-10 *Hz*) using a pulsed laser deposition (PLD) technique. The cathode powders were ball milled for 48hrs in ethanol using zirconia milling media. The resultant cathode materials mixed with an organic binder (Heraeus V006) to make slurry which subsequently applied on the thin film electrolyte using screen printing method. The effective electrode area of the cell was 1.13 cm^2. During the single-cell performance test, humidified H_2 (~3% H_2O at 30 ºC) and air were supplied as fuel and oxidant, respectively, at a constant flow rate of 100 mL min^{-1}. Platinum grids and wires were attached onto porous electrodes, and were used as current collectors. Current-voltage (*IV*) measurements were performed with two electrode configuration consisting of the cathode and anode in cell operation with an Arbin BT2000/fuel cell test station. The schematically illustration of the SOFC power measurement is shown in Fig 2.12. More detailed experimental methods such as the firing temperature of various cathodes, anode disks and so on will be presented in the following chapters.

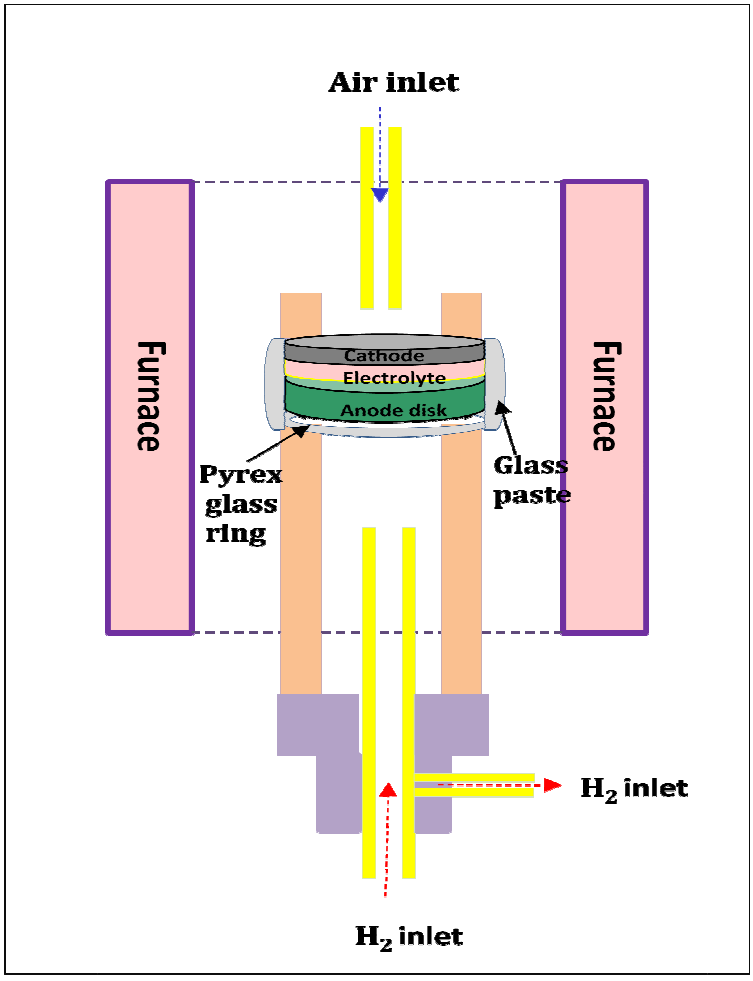

Fig 2.12. Schematically illustration of the SOFC power measurement.

CHAPTER III

VERTICALLY ALIGNED NANOCOMPOSITE THIN FILMS AS A CATHODE-ELECTROLYTE INTERFACE LAYER FOR THIN FILM SOLID OXIDE FUEL CELLS

3.1 Overview

A thin layer of a vertically-aligned nanocomposite (VAN) structure was deposited between the electrolyte, $Ce_{0.9}Gd_{0.1}O_{1.95}$ (CGO), and the thin film cathode layer, $La_{0.5}Sr_{0.5}CoO_3$ (LSCO), of a thin film solid oxide fuel cell (TFSOFC). The self-assembled VAN nanostructure contains highly ordered alternating vertical columns of CGO and LSCO formed through a one-step thin film deposition process using pulsed laser deposition (PLD). The VAN structure significantly improves the overall performance of the TFSOFC by increasing the interfacial area between the electrolyte and the cathode. Low cathode polarization resistances of 9×10^{-4} Ω and 2.39 Ω were measured for the cells with the VAN interlayer, respectively, at 600 and 400 ^{o}C. Furthermore, anode-supported single cells with LSCO/CGO VAN interlayer demonstrate maximum power densities of 329, 546, 718, and 812 mWcm^{-2} at 550, 600, 650, and 700 ^{o}C, respectively, with an open circuit voltage (OCV) of 1.13 V at 550 ^{o}C.

---

* Reprinted with permission from "Vertically aligned nanocomposite thin films as a cathode-electrolyte interface layer for thin film solid oxide fuel cells" by J. Yoon, S. Cho, J-H. Kim, Z. Bi, J. Lee, A. Serquis, X. Zhang, A. Manthiram, H. Wang, Journal of Advanced Functional Material, 19 (2009) 1-6. Copyright (2009).

The cells with the interlayer *triple* the overall power output at 650^{o}C compared to that achieved with the cells without interlayer. The binary VAN interlayer could also act as a transition layer that improves adhesion and relieves both thermal stress and lattice strain between the cathode and the electrolyte.

3.2 Introduction

Thin film solid oxide fuel cells (TFSOFCs) have been extensively investigated because of their potential in compact and high-efficiency energy conversion applications. TFSOFCs are one of the most promising alternative energy sources among all fuel cell types because they have wider fuel options and higher fuel efficiency when combined with heat processors. Although current SOFC technology has made great progress, there are several technical challenges that need to be addressed to realize its wide applications. For example, conventional SOFCs require relatively high operating temperatures around 700-900ºC because of the low ionic conductivity of the electrolyte at low temperatures. This temperature limitation imposes a considerable amount of constraint on selecting cell component materials such as interconnect, electrode, and gasket materials, which ensure the structural integrity of the cell after many thermal cycles. Furthermore, in order to achieve cost effectiveness and expand the cell lifetime, it is also necessary to decrease the cell operating temperature down to 500 ºC or lower [85]. However, the ionic conductivity of electrolyte decreases significantly at these lower temperatures. The most promising way to enhance the ionic conductivity at low temperatures is to reduce the electrolyte thickness, which is quite difficult to achieve for

electrolyte-supported SOFCs. We present here an alternative approach to overcome this problem where a conventional electrolyte-supported structure can still be used.

In order to increase the reaction probability, a vertically aligned nanocomposite (VAN) layer is introduced between the cathode and the electrolyte, which increases the effective area of triple phase boundary (TPB) at the cathode/electrolyte interface. It was previously reported that the microstructural variations in the electrolyte and the electrode could affect the reaction kinetics of thin film SOFCs dramatically [86-91]. The majority of power losses in planar SOFCs occurs as a result of the polarization resistance at the cathode/electrolyte interface. The binary VAN interlayer is a composite of cathode and electrolyte materials, in our case, $La_{0.5}Sr_{0.5}CoO_3$ (LSCO) and $Ce_{0.9}Gd_{0.1}O_{1.95}$ (CGO). The VAN interlayer is processed through a single-step deposition without any additional lithography patterning steps. A schematic sketch of the binary VAN interlayer is given in Fig 3.1(a) and (b). This layer effectively increases the cathode-electrolyte interfacial area in a controllable fashion, lowers the polarization resistance of the cathode/electrolyte interface, and improves the kinetic performance of the cathode. These improvements increase the overall performance of the TFSOFC. The goal of this work is to achieve an overall enhancement in power output in anode-supported solid oxide fuel cells by implementing the binary VAN interlayer in the cells and tuning the microstructure of the CGO electrolyte and the LSCO cathode.

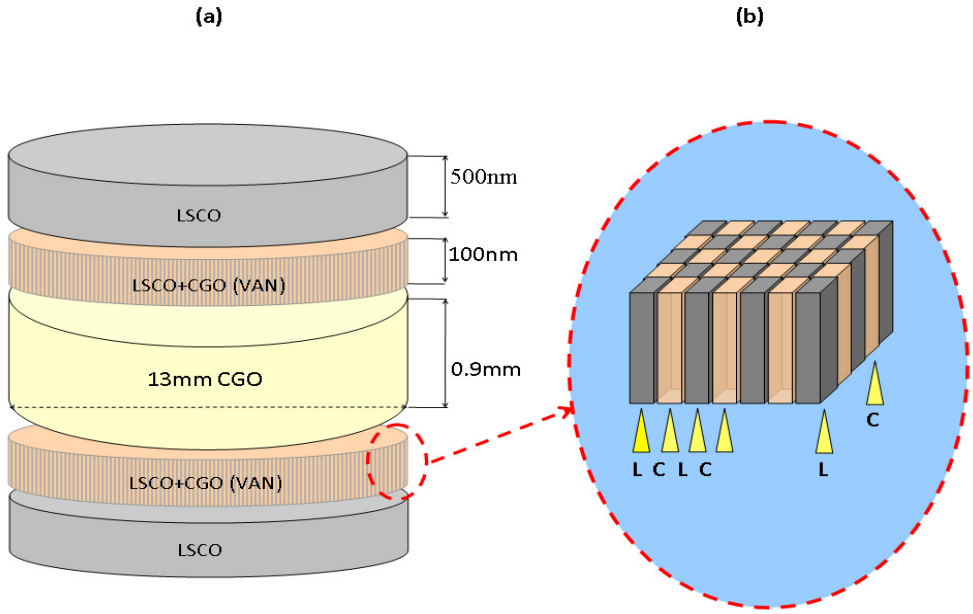

Fig 3.1 (a) Schematic diagram of a symmetric cell and (b) VAN interlayer where "L" and "C" stand, respectively, for LSCO and CGO columns.

3.3 Experimental

Pulsed laser depositions (PLD) of the VAN interlayer, CGO electrolyte, and LSCO cathode layer were performed in a multitarget chamber with a KrF excimer laser (Lambda Physik 210, λ = 248 nm, 5-10 *Hz*). Various substrates including YSZ, STO, pressed CGO disks, and pressed anode disks were selected for this work. The laser beam was focused to obtain an energy density of approximately 5 J cm^{-2} at 45º angle of incidence. The hot-pressed targets including LSCO, LSCO + CGO (50:50), 8 mol% YSZ (500nm, Tosoh Co), $Ce_{0.9}Gd_{0.1}O_{1.95}$ (CGO), 60wt% NiO + 40wt% $Ce_{0.8}Gd_{0.2}O_{1.95}$ (NiO-CGO, 500nm, Praxair Inc) anode disks, and CGO electrolyte disks were all prepared by mixing stoichiometric amounts of the raw powders including La_2O_3, $Sr(NO_3)_2$, Co_3O_4, CeO_2, and Gd_2O_3. LSCO/CGO VAN interlayers (about 50 – 100 nm) were processed through a one-step thin film deposition. For preparing the anode substrates, the commercial NiO-CGO cermet was compacted into disks under uniaxial pressure using a die set of 1inch in diameter and sintered at 1350 ºC for 3 h. Subsequent 8 um CGO electrolyte (with a thin layer of YSZ deposited prior to the CGO layer), 2 um VAN interlayer, and 30 um LSCO thin film cathode layer were deposited on a NiO-CGO anode disk substrate under the stated conditions in our previous work [92-94]. The growth rates of these thin films were about 1 nm/s for LSCO cathode layer, 0.1 nm/s for VAN interlayer at an oxygen partial pressure of about 200 mTorr, and, 0.8 and 0.9 Å/s for YSZ and CGO layers under an oxygen partial pressure of 20 mTorr. The substrate temperature was varied from 300 to 700 ºC to optimize the film crystallinity and the nanopore size of the cathode layer. Four symmetrical working cells with different VAN

thicknesses were prepared to study the effects of interlayer thickness on the cathode polarization resistance. Microstructural characterizations of these films were performed by cross-sectional TEM using a JEOL2010 analytical electron microscope and a JEOL3000F analytical electron microscope with a point to point resolution of 0.18 nm. STEM was performed by a FEI Tecnai F20 with a point to point resolution of 0.27 nm. Surface morphology study for the thin films was conducted by SEM. The electrochemical cells were prepared with the symmetrical configuration. Platinum grids were slightly pressed onto porous electrodes, and were used as current collectors. Using a potentiostat/impedance analyzer (Autolab-Eco Chemie BV), ac impedance spectroscopy measurements were conducted in the frequency range of 10^{-3} – 10^{6} *Hz* from 400 to 600 ºC in pure oxygen. The AC impedance data were measured after a waiting period of 3-8 h at each temperature until the system was stabilized. The effect of VAN interlayer on the cathode performance was evaluated with the anode-supported single cells consisting of LSCO/VAN/CGO/YSZ/NiO+CGO, and compared with the cell without VAN interlayer. During the single-cell performance test, humidified H_2 (~3% H_2O at 30 ºC) and air were supplied as fuel and oxidant, respectively, at a constant flow rate of 100 mL min^{-1}. The effective electrode area of the cell was 1.13 cm^2. Measurement details can be formed from previous work [92-93].

3.4 Results and Discussions

Yttria-stabilized zirconia (YSZ) and $SrTiO_3$ (STO) substrates were chosen first to demonstrate the growth of binary VAN structures of LSCO/CGO. Cross-sectional transmission electron microscopy (TEM) images of a typical VAN interlayer structure are shown in Figs 3.2(a) and (b). Alternating vertically aligned columns, around 10 nm in diameter, of CGO and LSCO grains grow over a large area (Fig 3.2(a)). The VAN structure extends all the way through the film thickness, in this case, 100 nm. LSCO has a perovskite structure with a lattice parameter of 0.381 nm and CGO is face-centered cubic with a lattice parameter of 1.084 nm (2×0.542 nm). Both of them match well with the lattice parameters of YSZ (a= 0.515 nm) and STO (a=0.390 nm), either through direct cube-on-cube matching or after a 45^o rotation. Another important consideration is that the possibility of intermixing between LSCO and CGO is small since the cations of one component are much larger than the interstitial sites of the other component. For example, $Ce^{3+/4+}$ ion is much larger than the interstitial sites in LSCO. Previously, we have successfully demonstrated the growth of $BiFeO_3$ / Sm_2O_3 VAN structure on a STO substrate and a LSMO/ZnO VAN structure on sapphire substrate with similar material selection criteria [94-96].A high resolution TEM image covering a set of VAN columns is shown in Fig 3.2(b). A LSCO/CGO binary VAN structure can be clearly observed based on their contrast difference in Fig 3.2(b).

To confirm that LSCO and CGO grow as alternative columns without intermixing, scanning transmission electron microscopy (STEM) was conducted under a high angle annular dark field (HAADF) condition. This is also called Z-contrast, where

the contrast is roughly proportional to Z^2. A typical Z-contrast image over a large area of LSCO/CGO VAN structure is shown in Fig 3.2 (c). Because of the higher Z numbers of Ce and Ga, CGO columns have much higher contrast (brighter columns) than LSCO columns. The CGO and LSCO grains grow as well aligned vertical columns and alternate with a column size of 5-10 nm. The vertical column interfaces are sharp and clean. EDX mapping was conducted over the same area (not shown here) and no obvious intermixing was observed.

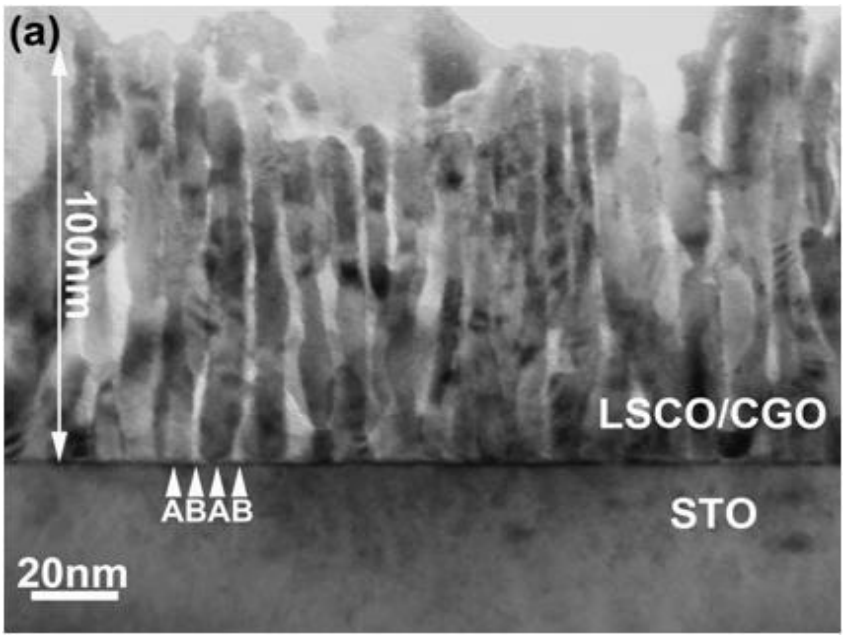

Fig 3.2**.** Cross-sectional (a) low magnification and (b) high resolution TEM images and (c) STEM image of a typical LSCO/CGO VAN structure grown by PLD on STO substrate.

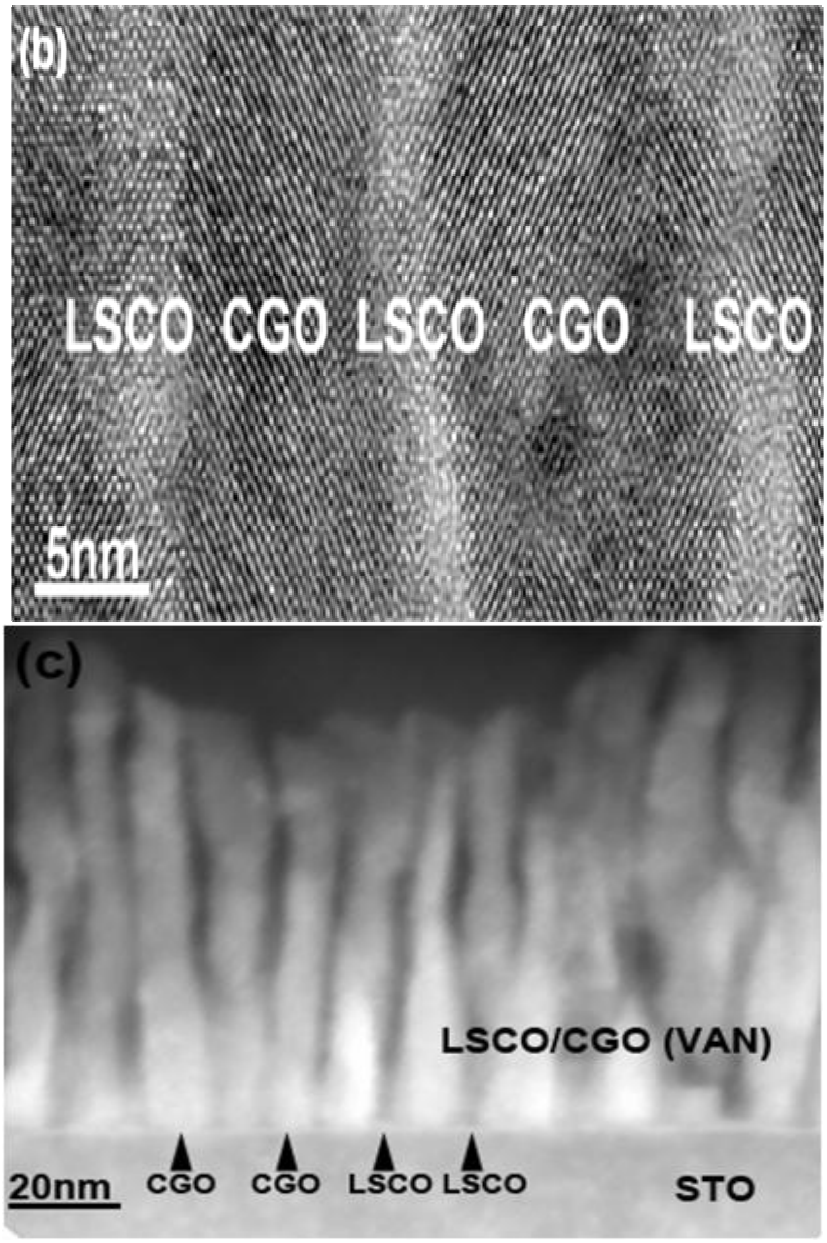

Fig 3.2**.** Continued.

In order to measure the electrochemical characteristics and test the performance of the cathode structure with the VAN interlayer, symmetric cells were processed with

the VAN interlayer deposited on both sides of a pressed CGO disk followed by depositing thin film cathode with vertically aligned nanopores (VANP) as illustrated in Scheme 1. The total cathode thickness is about 600 nm on both sides. We used the same deposition condition to ensure the identical properties on both sides of the cells. Four button cells with different VAN interlayer thicknesses were prepared in order to investigate the relationship between the VAN thickness and the electrochemical performance of the cells. The VAN structure can effectively increase the cathode-electrolyte interfacial area in a controllable fashion. Ratios of the interfacial area densities of samples with varying interlayer thickness and without the VAN layer are summarized in Table 3.1. For example, the 100 nm-thick VAN structure can increase the interfacial area up to 25 times compared to the case without the VAN interlayer. By controlling the interlayer thickness, one can systematically vary the interfacial area density. For this typical VAN structure, the average width of these nano-columns are about 5~10 nm. It is interesting to note that by controlling the deposition conditions including deposition temperature and the stoichiometry of the binary target, it is possible to vary the width of the VAN structure [96]. Sample D is a reference cell with only the VANP structure, while sample A, sample B, and sample C have both the VANP and VAN structures. Sample B has a VAN layer thickness twice that of sample A while sample C has a VAN thickness equal to that of sample A, but with an additional thin film CGO layer (~500 nm between the VAN interlayer and the CGO disk). The additional thin film CGO layer serves as a seed layer for the subsequent VAN interlayer

and provides a much smoother surface for the growth of the subsequent thin film VAN interlayer.

Table 3.1. VAN layer thickness and the ratio of the interfacial area density.

Sample ID	Thin Films on CGO disk	Film Thickness			Ratio of the interface area density
		VANP [nm]	VAN [nm]	CGO [nm]	
A	VANP/VAN	500	50	0	14
B	VANP/VAN	500	100	0	25
C	VANP/VAN/CGO	500	50	500	14
D	VANP	500	0	0	1

Cross-sectional TEM images of one such a symmetric cell, sample B (LSCO / LSCO + CGO / CGO disk), are shown in Figs 3.3(a) and (b). Fig 3.3(a) shows a cross-sectional TEM image of the LSCO cathode and the VAN interlayer deposited at 300 ºC and 650 ºC, respectively, on a CGO disk. It shows that, over a large area, the VAN interlayer grows as a smooth and dense layer with a film thickness of about 100 nm. On the top of the VAN layer, the LSCO cathode layer exhibits porous columnar growth with the pores vertically aligned in the film. In Fig 3.3 (b), an obvious surface roughness is observed in the cathode layer. The roughness is a result of the uneven surface of the CGO disk before deposition. This LSCO cathode layer has columnar grains with a grain size of 100–200 nm. The vertically-aligned nanopores can be clearly observed in Fig 3.3 (b). The total cathode thin film thickness including VAN interlayer in this sample is approximately 600 nm.

A typical scanning electron microscopy (SEM) image (Fig 3.3(c)) of the surface of the top cathode layer shows the grain structure with nanopores between the columnar grains. From the view area, no micro cracks were observed at the film surface after the thermal cycle during thin film depositions. The binary VAN interlayer acts as a transition layer that partially relieves the internal thermal stress and lattice strain between the cathode layer and the electrolyte. The interlayer can also improve the adhesion between the cathode and the electrolyte layers.

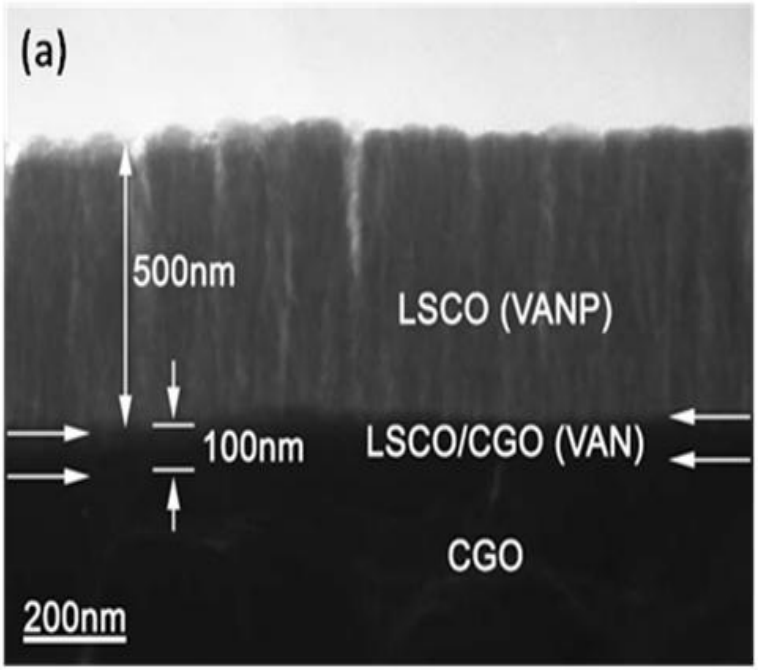

Fig 3.3. (a) Low magnification cross-sectional TEM image of the LSCO cathode and the VAN interlayer on a pressed CGO disk, (b) a closer view of the VAN interlayer structure on the CGO disk, and (c) SEM image showing a smooth surface of the cathode layer without microcrack formation.

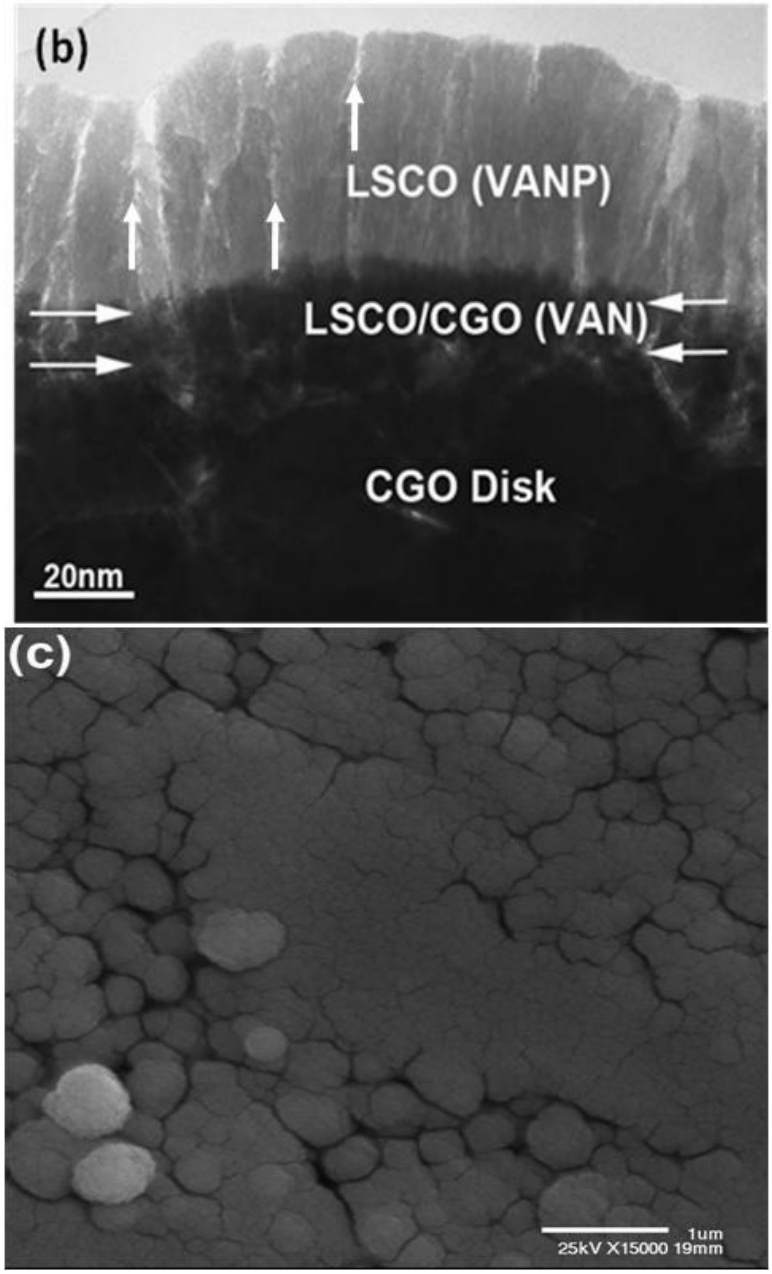

Fig 3.3. Continued.

To test the polarization resistance of the thin film cathode with the binary VAN interlayer, the complex impedance spectra were measured in oxygen in the range of 400–600 °C for all the symmetric cells. The AC Impedance spectrum of the symmetric cell with a 50 nm VAN interlayer was obtained under oxygen atmosphere at 403 ºC, as shown in Fig 3.4. Earlier study showed that the high frequency arc is independent of the oxygen partial pressure and it was attributed to the grain boundary resistance in CGO. [97-98]. The Pt/CGO/Pt cell also confirmed that the high frequency arc is due to the grain boundary resistance at this temperature. The beginning of the electrode polarization resistance was determined by fitting the electrolyte spectrum with a circuit consisting of a resistance and a constant phase element (CPE) connected in parallel. Fitting was performed with the ZView 2.8d program in Fig 3.4. For temperatures higher than 550 °C, the electrolyte spectrum is not observed due to the short time constant of the grain boundary resistance. The beginning of the electrode polarization resistance was obtained from the high frequency intercept of the spectrum with the Z' axis and the end of the polarization resistance were calculated as the average of the low frequency impedance module, when it becomes approximately constant. The error bar was estimated by taking into account of the error of the electrolyte fitting and the difference between the average and the extreme value (maximum or minimum) of the data to calculate the end of the electrode polarization resistance.

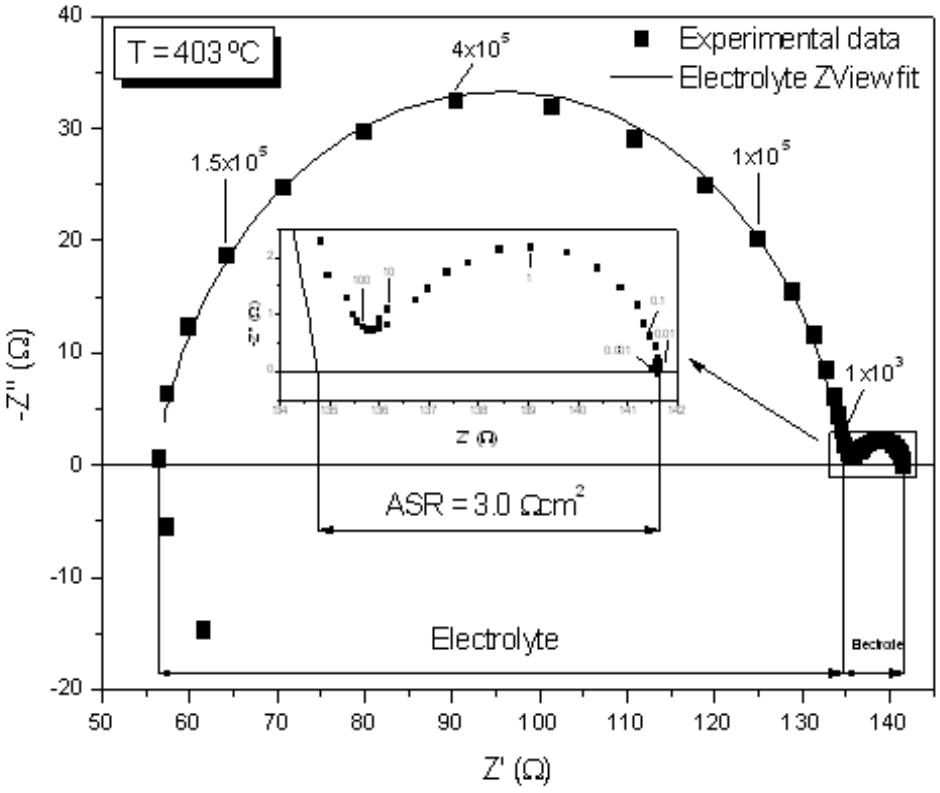

Fig 3.4. AC Impedance spectra of Nyquist plot of the symmetric cell with a 50 nm VAN interlayer at 403 ºC. The inset shows a zoom of electrode spectra.

Area specific resistance (ASR) of cathodes was determined according to the following formula (1) for a symmetric cell:

$$ASR = \frac{R_p \cdot A}{2} \tag{3.1}$$

where, R_p is the cathode polarization resistance and A is the geometrical cathode area.

An Arrhenius plot of area specific resistance (ASR) versus temperature of all the samples with different VAN interlayer thicknesses is plotted in Fig 3.5 and compared with the LSCFO cathode under the different oxygen partial pressures [97-99]. In our previous work, we have demonstrated that VANP structure can help oxygen gas phase to diffuse to reaction sites, thus enhancing the total electrochemical activity at the reaction sites. At 400 ^{o}C, the ASR is about 3.5 Ωcm^2 for sample B with a 100 nm VAN interlayer. Hence, in this work we have further lowered the ASR by at least one order of magnitude by including the binary VAN interlayers compared to that in the previous work [96]. By a large error for data measured above 550°C, the ASR was reduced by an order of magnitude compared to the small resistance resulted in the previous work. Considering the fact that iron or manganese doped LSCO cathodes give better performance than simple LSCO cathodes [100], this work suggests that doped LSCO cathodes can improve the fuel cell performance even further by inserting the VAN interface layer. Fig 3.5 indicates that the ASR plot shifts to lower values as the VAN interlayer thickness increases. This suggests that the VAN interlayer plays an important

role in decreasing the ASR. As seen in Table 3.1, the cathode / electrolyte interface area density increases as the VAN interlayer thickness increases. Therefore, the VAN interlayer enhances the catalytic reaction probability at the gas–cathode–electrolyte TPBs by increasing the effective area of the TPBs, and thus decreasing the area specific resistance of the cathode, which leads to the overall improved TFSOFC performance. Results are reproducible at different temperatures after the high temperature thermal cycles. There is no significant structural degradation (second phase formation or interfacial diffusion) for the cells with the VAN interlayer, and the VAN structure is stable after thermal cycles.

Adding an additional CGO seed layer, sample C shows the lowest ASR, which is about 35% lower than that of sample A with no CGO seed layer. This suggests the effectiveness of the additional thin film CGO seed layer. The possible functions of the CGO seed layer are: (1) improving the gas tightness of a hot pressed 0.9 mm thick CGO electrolyte, (2) preventing interfacial reactions between the electrolyte and the cathode materials, and (3) improving the charge transfer process at the electrode and the electrolyte interface [101]. The effect of the CGO layer became more pronounced at lower temperatures. Since the grain boundary region has lower ionic conductivity and higher activation energy than the bulk lattice, the grain boundary effects become significant at the intermediate temperature regime, 400 to 600 ºC [100]. However, at operating temperatures above 700 ºC, the grain boundary effect is negligible because high enough temperatures overcome the high activation energy.

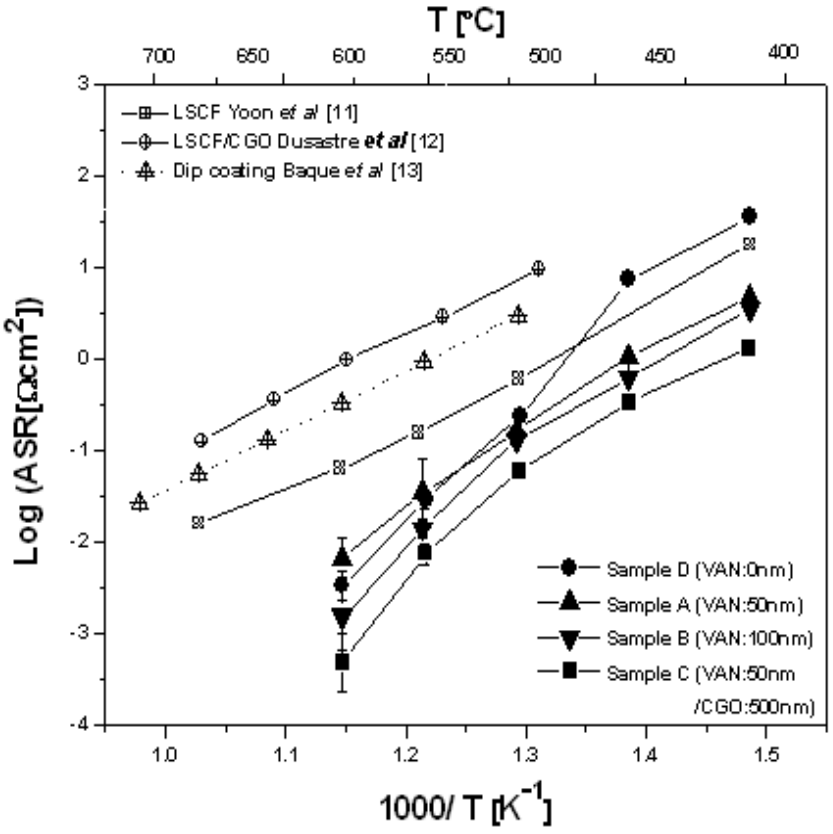

Fig 3.5. ASR of the symmetrical cells with VANP/VAN structures on CGO disks grown by PLD.

The I-V characteristics of the anode-supported single cells was measured by a two-electrode set-up under humidified hydrogen at the rate of 100 mL min^{-1}, using Pt wires held by Pt paste as electrical contacts. For SOFC measurement, the electrodes must be sufficiently porous to allow gaseous diffusion and the electrolyte should be dense, crack-free to act as a barrier for the fuel gases and oxidant for the electrodes on both sides [102-103]. The performance was measured at temperatures ranging from 550 to 750^{o}C. Fig 3.6(a) shows the cell voltage and power density as a function of current density without VAN interlayer. The OCV was 1.13 V at 600^{o}C, and the maximum power density of the cell was 172, 272 (highlighted as red arrow), and 390 $mWcm^{-2}$ at, respectively, 600, 650, and 700^{o}C. The overall trend is that the power density decreases as the measurement temperature decreases, and the cell potential also decreases due to the increasing polarization losses across the cell drawing current density. The cell with VAN interlayer (Fig 3.6(b)) provided an OCV of 1.13 V at 550^{o}C and maximum power densities of 329, 546, 718 (highlighted as red arrow), and 812 $mWcm^{-2}$ at 550, 600, 650, and 700^{o}C, respectively. Compared to the cells without interlayer, the cells with the interlayer (Fig 3.6(b)) triple the overall maximum power density at both 600 and 650^{o}C and double the power density at 700^{o}C. The overall cell performance is better than previously reported single cells with similar structure and material systems [102, 104-107]. It is noted that, concentration polarization is observed under high current drain (> 1.4 A/cm^{2}) due to the effect of anode porosity and limited fuel supply, which prevent us from evaluating the true maximum power density of the cell at 650 and 700^{o}C. The high open circuit voltages (OCV) of > 1.1 V was obtained at all temperatures by employing a

thin YSZ electrolyte in between the anode and CGO electrolyte. The YSZ thin layer prevents the reduction of Ce^{4+} into Ce^{3+} ions occurring in contact with hydrogen and the consequent decrease in OCV [108]. Besides the power density enhancement demonstrated by the binary VAN interlayer between the cathode and the electrolyte, the interlayer also performs as a transition layer mitigating thermal stress and lattice strain at the interface. This could lead to a longer life time for the cells under thermal cycles.

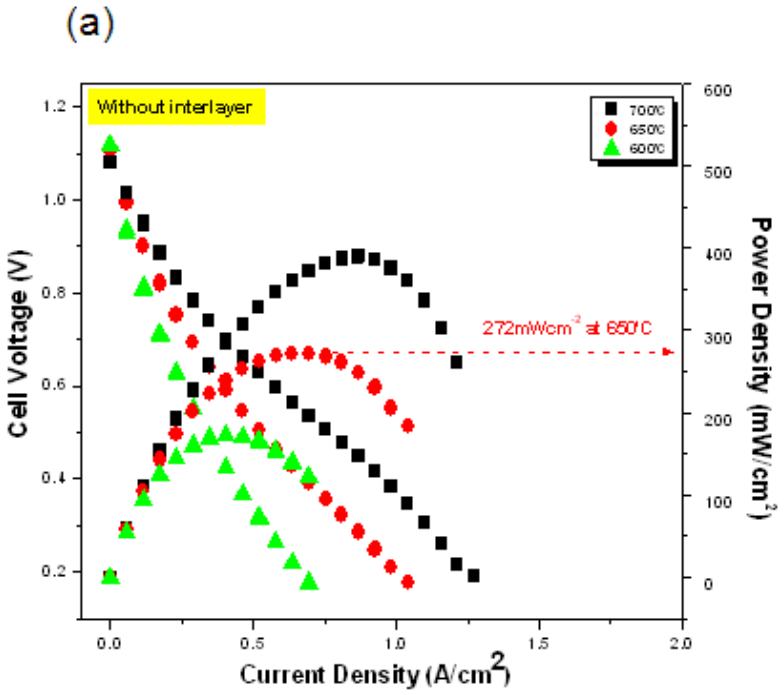

Fig 3.6. Cell voltages and power densities of anode-supported single cells at different temperatures. (550~ 700 ^{o}C) (a) without interlayer and (b) with VAN interlayer. The data demonstrate a tripling of the power density values with the VAN interlayer.

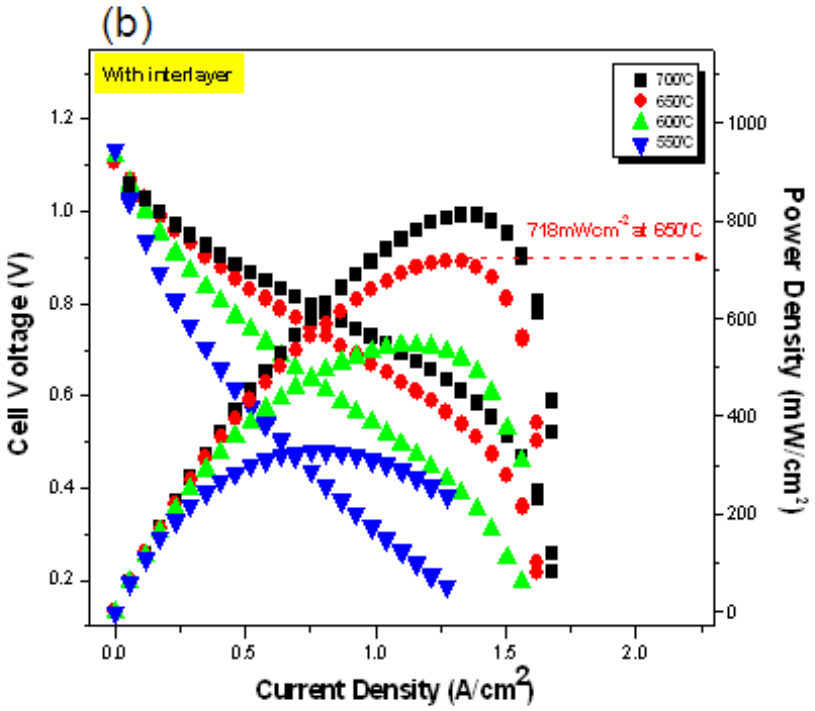

Fig 3.6. Continued.

3.5 Conclusions

We have successfully processed a binary VAN interlayer of $(LSCO)_{0.5}(CGO)_{0.5}$ between the cathode and the electrolyte for high efficiency thin film SOFC. This unique binary VAN interlayer effectively increases the cathode/electrolyte interfacial area density (by 14~25 times depending on the interlayer thickness) and significantly lowers the polarization resistance present at the cathode/electrolyte interface. Hence, low cathode polarization resistances of 9×10^{-4} Ω and 2.39 Ω were measured, respectively, at 599 and 400°C, and by combining a CGO seed layer with the VAN interlayer, a record low ASR (4.84×10^{-4} Ωcm^2 at 599°C, 1.25 Ωcm^2 at 400° C) was achieved. The effect of varying deposition parameters (pressure, pulse time) on the VAN interlayer thickness and column width is shown; the interfacial area density can be systematically controlled by varying these two dimensions. As the VAN thickness increases, the ASR shifts to lower values. The single cells with the binary VAN interlayer using NiO-CGO anode-supported structure show excellent power performance. The maximum power densities of the single cells are 329, 546, 718, and 812 $mWcm^{-2}$ at 550, 600, 650, and 700°C, respectively, with an OCV of 1.13 V at 550 °C. The cells with VAN interlayer demonstrate superior cell performance compared to the cells without the interlayer and previously reported cells with similar geometry and materials.

CHAPTER IV

MICROSTRUCTURAL AND ELECTRICAL PROPERTIES OF GDC THIN FILM ELECTROLYTE IN SOLID OXIDE FUEL CELLS

4.1 Overview

Microstructural and electrical properties of Gd-doped CeO_2 (GDC, $Ce_{0.9}Gd_{0.1}O_{1.95}$) thin films prepared by pulsed laser deposition as an electrolyte in solid oxide fuel cells (SOFCs) were investigated. The GDC thin films were prepared on various substrates including single crystal yttria-stabilized zirconia (YSZ) and magnesium oxide (MgO) substrates. The GDC thin film electrolytes with different grain sizes and grain morphologies were prepared by varying the deposition parameters, such as substrate temperature, oxygen partial pressure, target repetition rate, and laser ablation energy. The microstructural properties of these films were examined using X-ray diffraction (XRD), transmission electron microscope (TEM) and atomic force microscope (AFM). Alternatingcurrent (AC) and direct-current (DC) electrical measurements measurements through in-plane method show that the electrical property of the GDC thin film strongly depends on grain size, e.g., the total conductivity of the

---

* Reprinted with permission from "Microstructure and Electrical Property of a $Ce_{.0.90}Gd_{0.1}O_{1.95}$ (GDC) thin film electrolyte in Solid Oxide Fuel Cells" by S. Cho, J. Yoon, J-H. Kim, X. Zhang, A. Manthiram, H. Wang, Journal of Materials Research, 26 (2011) 854-859. Copyright (2011).

films deposited at 700°C (7.3 x 10^{-3} Scm^{-1}) is about twenty-times higher than the ones deposited at room temperature (3.6 x 10^{-4} Scm^{-1}) at the measurement temperature of 600^{o}C.

4.2 Introduction

Compared with other fuel cell types, solid oxide fuel cells (SOFCs) have high power efficiency and excellent long-term performance stability, and are an environmentally friendly alternative to conventional energy conversion devices [109]. Currently, the high internal resistance (IR) loss of electrolyte requires high operating temperature in SOFCs. In order to tackle this problem, there are several main approaches, including an increase in the ionic conductivity of the electrolyte by searching for new electrolyte materials such as gadolinia-doped ceria (GDC) and $La_{1-x}Sr_xGa_{1-y}Mg_yO_{3-\delta}$ [110-115], reducing the thickness of electrolyte [116-118], and decreasing electrode polarization resistance [119-120]. Some of the most successful approaches to reduce the operating temperature are to grow thinner electrolyte using thin film fabrication technique and to select new electrolyte materials with higher ion conductivity [121].

From the materials selection point of view, yttria-stabilized zirconia (YSZ) is one of the well-known electrolytes for SOFC applications. To achieve sufficiently high ion conductivity, a high operating temperature, typically around 1000˚C, is required, which severely limits the material selections on other components and decrease the long term stability of SOFCs [122]. Recently, GDC is studied as a promising candidate for

electrolyte. It has higher ionic conductivity than that of YSZ in the intermediate/low temperature range of 400–700˚C and a thermal expansion coefficient that closely matches with many metallic materials as well. This allows more flexibility in the materials selection of electrodes and interconnects thermal stress reduction in active ceramic structures as well as a longer lifetime of the cells. Considerable effort has been made on the demonstration of low temperature SOFCs based on thin film electrolyte of doped ceria (CeO_2) [123-124]. The microstructure of the GDC thin electrolyte layer can be well controlled by varying the deposition parameters in thin film deposition technique. Therefore, a systematic study to correlate microstructure (e.g., grain boundary structure) and the ionic conductivity is in great need for implementing GDC thin film electrolytes in SOFCs.

Several studies have being previously conducted on the electrical and microstructural properties of GDC electrolytes processed by various thin film deposition techniques such as spray pyrolysis [125], RF reactive magnetron sputtering [114, 126], pulsed laser deposition (PLD) [127-129], etc. Chen *et al.* demonstrated the $Ce_{0.80}Gd_{0.20}O_{2-\delta}$ (GDC20) thin films with cube-on-cube epitaxy on MgO (001) substrates by PLD. It was reported that the electrical conductivity of $Ce_{0.80}Gd_{0.20}O_{2-\delta}$ (GDC20) film is predominately ionic conductor under pO_2 in the range from 10^{-19}atm to 1 atm [127]. Joo *et al.* investigated the nanocrystalline GDC20 thin films with (111), (200) and (111) orientations on Pt (111) and sapphire (0001) substrates under a low oxygen partial pressure (~50mTorr) at 500 and 700°C by PLD and performed the electrical conductivity measurements on GDC20 thin film in in-plane and across-plane [128].

Infortuna *et al.* examined the microstructure evolution of GDC and YSZ thin films by PLD as functions of deposition temperature (room temperature (RT) ~ 900°C) and oxygen partial pressure (20~ 300mTorr) [129]. However, a systematic study on correlating the electrical properties of the GDC films with their grain sizes and grain morphologies was lacking.

In this paper, we present the deposition of GDC thin films with different grain sizes using a PLD method commonly used to deposit complex ceramic materials with the same or similar stoichiometry as the target material [130]. Specifically, we explored the grain size of the GDC films from nanocrystalline to epitaxial thin films by controlling the growth temperature. A detailed microstructural characterization was conducted and correlated with the electrochemical properties of the films as functions of grain size and grain morphologies.

4.3 Experimental

The depositions of the GDC electrolyte layers were conducted under oxygen partial pressure in the PLD chamber with a KrF excimer laser (Lambda Physik 210, California, USA, λ = 248 nm, 5*Hz*, O_2 pressure of 200 mTorr). The laser beam was focused to obtain an energy density of approximately 5 J cm^{-2} at 45º angle of incidence. For preparing the pressed target of $Ce_{0.9}Gd_{0.1}O_{1.95}$, the commercial GDC powder (500nm, Praxair Inc, New York, USA) was pressed into disk under uniaxial pressure using a 31mm die set. The disk was then sintered at 1200 ºC for 10 h with flowing oxygen. Various substrates including YSZ (001), and MgO (001) were selected for this

work. The substrate temperature was varied from RT to 700 ºC to control the grain size of the film [131]. The thin film growth rate of the GDC was 6.8, 3.6, 2.8, and 2.1$\mathring{A}s^{-1}$ under an oxygen partial pressure of about 200mTorr at the deposition temperature of RT, 300, 500, and 700ºC, respectively. Microstructural characterizations were performed by X-ray diffraction (XRD, Bruker, Wisconsin, USA) and cross-sectional TEM using a JEOL2010 analytical electron microscope (Tokyo, Japan) and a JEOL-3000F analytical electron microscope with a point to point resolution of 0.18 nm. Surface morphology study for the thin films was conducted by atomic force microscope (AFM, Digital Instruments Nanoscope**,** California, USA). For the electrochemical cells, two rectangular platinum strips (Heraeus CL11-5100, Pt ink, Hanau, Germany) on the GDC thin film were prepared by screen printing method and then the sample was baked on a hot plate at 100 ºC for 10 min. Platinum grids as current collectors were attached onto the top of platinum electrodes on the GDC thin film. The conductivity measurements of films were examined using DC four-probe method and impedance analyzer (Gamry Instrument (Pennsylvania, USA)), Solartron potentiostat (Hampshire, United Kingdom)) in the frequency range of 10^{-1} – 30M*Hz* under pure oxygen from 400 to 800 ºC. More details on the measurements can be found elsewhere [132-133].

4.4 Results and Discussions

Fig 4.1 shows the XRD patterns of the GDC thin film samples containing 10 mol% of gadolinia deposited at RT, 300ºC, 500ºC, and 700ºC on YSZ (001) single crystal substrates. The XRD pattern revealed that textured growth starts at 500ºC and strong (00*l*) GDC peaks (both (002) and (004) peaks) can be observed at 700ºC. No secondary or impurity phases were detected in the films. It suggests that at the given doping concentration of gadolinia, the deposition temperature of 500ºC is adequate to ensure the formation of highly textured GDC thin films along (00*l*) orientation. The crystallinity of the films increases with increasing substrate temperature as evidenced by the increasing peak intensity of (002) and (004) GDC peaks. It is interesting to note that GDC on YSZ still maintains a cube-on-cube matching relation even though YSZ (a=5.147 Å) has a large lattice mismatch with GDC (a=5.418 Å). The lattice mismatch could be about 5%. Based on the GDC (002) and (004) peak positions, the calculated lattice parameter of the GDC thin films is 5.412 Å. The large lattice mismatch is accommodated by domain matching epitaxy where 20 lattices of $(004)_{YSZ}$ match with 19 lattices of $(004)_{GDC}$. The residual lattice mismatch is 0.05% and the misfit dislocation spacing is ~5 nm. The XRD results of GDC films on MgO substrates (not shown here) are very similar to that of GDC films on YSZ with highly textured GDC thin films along (00*l*) orientation for the samples deposited higher than 500ºC.

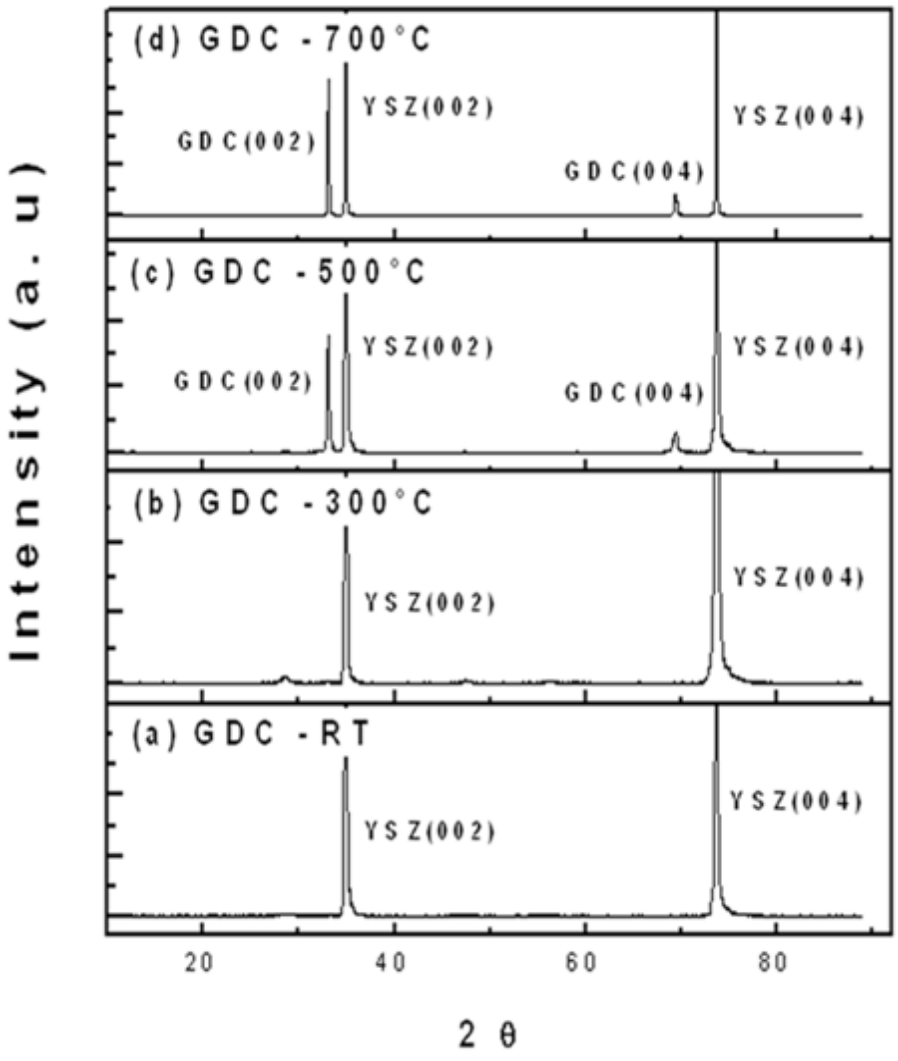

Fig 4.1. XRD patterns of GDC thin films deposited on YSZ substrates at various temperatures.

In order to observe the microstructure evolution across the film thickness, we conducted a detailed cross sectional TEM study for all of the GDC films on single crystal YSZ substrates, as shown in Fig 4.2. At room temperature (Fig 4.2(a)), the grain size is in the range of 5-10 nm due to the limited adatom surface mobility at low temperatures. The grains are randomly oriented as evidenced by the nanosized grains in the TEM image and the ring pattern in the corresponding selected area diffraction pattern (SAD, inset in Fig 4.2(a)). By increasing deposition temperature, the grain size increases obviously and the grains show more columnar structure. As the deposition temperature increases to 500 ºC and 700 ºC, highly epitaxial film starts to form as shown in Figs 4. 2(c) and 4.2(d). The obvious matching relation was found in the inserted SAD patterns in Figs 4.2(c) and 4.2(d), which is a clear cube-on-cube matching relation without any rotation in axis. It is noted that the films are very dense and free from cracks and pores from the cross-sectional images. Overall the microstructural features identified in TEM are consistent with the XRD results.

The surface morphology of the GDC thin films was observed by AFM. Fig 4.3 (a)-(d) shows the AFM images of the GDC thin films deposited on YSZ substrates at RT, 300ºC, 500ºC, and 700ºC, respectively. An apparent difference between the room temperature sample and all the others (300 to 700ºC) is that the RT sample shows much smaller grains and the grains are more isolated, which leads to a relatively porous surface structure.

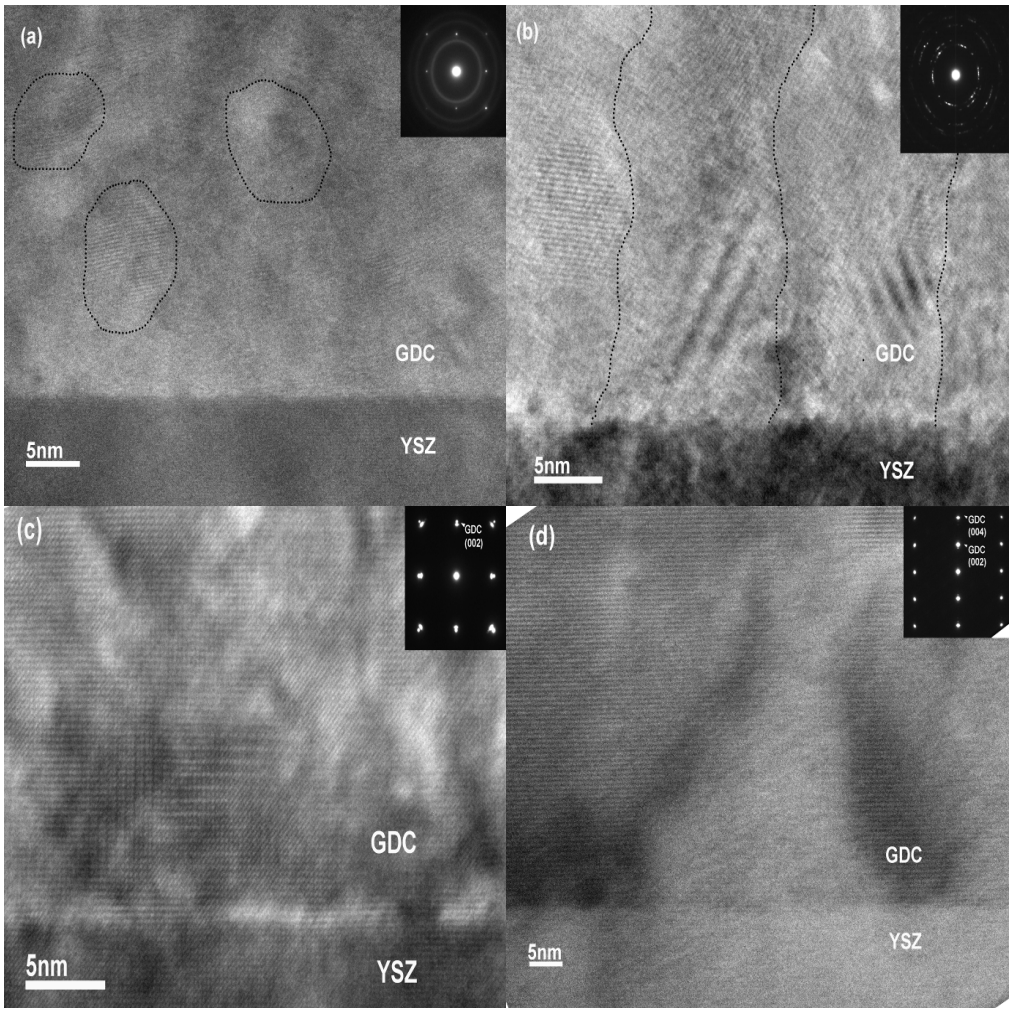

Fig 4.2. High resolution cross-section TEM images of GDC thin films deposited at (a) RT, (b) 300ºC, (c) 500ºC, and (d) 700ºC.

The average grain size of the RT sample is about 90 nm or smaller based on the surface morphology. However, the samples deposited at high temperatures show much larger grains which are well connected into large domain structures. The average domain size for the samples varied from 1 μm (300ºC) to 3 μm (700ºC). The increased grain / domain size is because of the increased adatom surface mobility at higher substrate temperatures.

A schematic sketch of grain morphology of the GDC thin films as a function of substrate temperature is given in Fig 4.4 based on the TEM and AFM observations. At low temperature (a), nanocrystalline films with some porosity can be formed due to the limited surface mobility of the adatoms. As the deposition temperature increases, a columnar grain structure forms because the mobility of adatoms at intermediate temperature (b) is still quite limited. As the deposition temperature increases to even higher (c), epitaxial films form. The thickness of the GDC films on the YSZ substrates varied in the range between 500 nm and 700 nm at different growth temperatures. Thin film growth depends on multiple parameters such as target to substrate distance, substrate temperature, laser ablation energy, and background oxygen pressure. Among those deposition parameters, substrate temperature is found to be one of the most critical factors in determining the film morphology and microstructure.

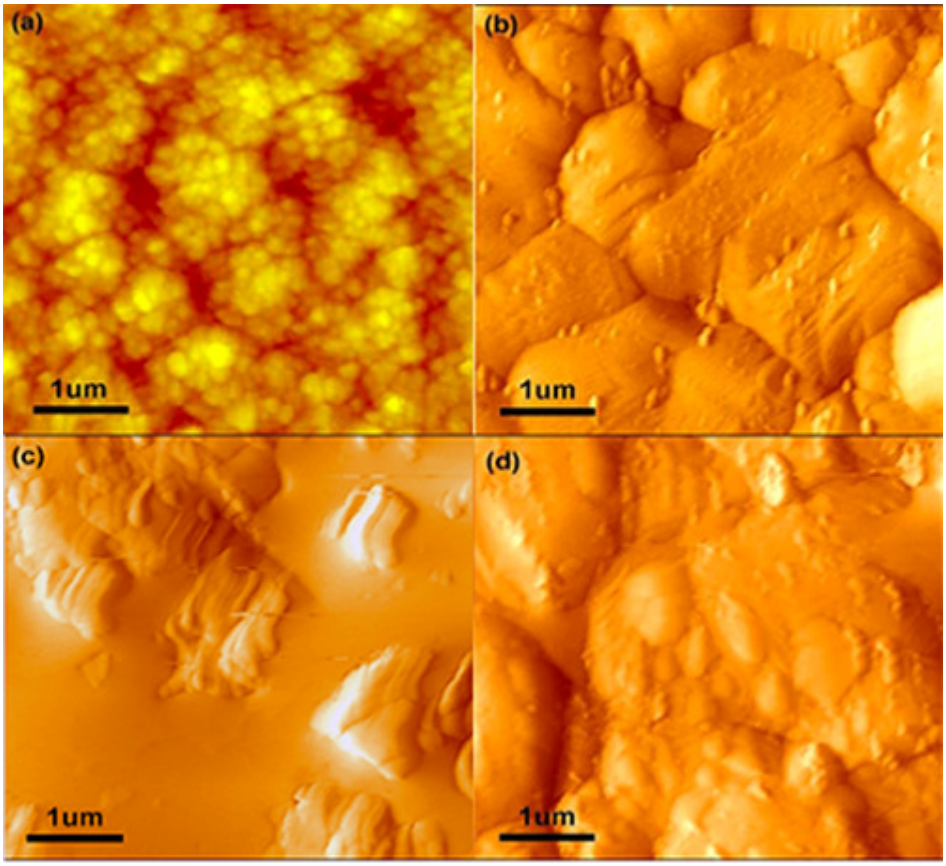

Fig 4.3. AFM images (5 **x** 5 μm in scan size) of microstructural GDC thin films deposited at (a) RT, (b) 300ºC, (c) 500ºC, and (d) 700ºC on YSZ substrates.

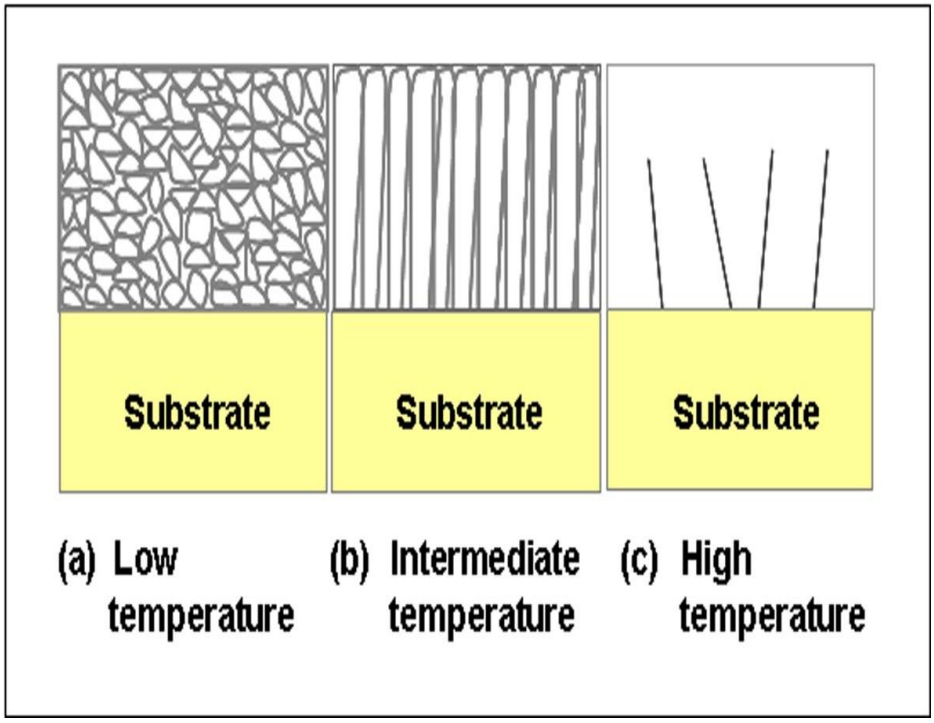

Fig 4.4. Schematic diagram of the thin film growth as a function of deposition temperature (a) nanocrystalline structure, (b) columnar structure, and (c) epitaxial structure.

To explore the effect of the grain size and grain boundary on the electrical properties of the GDC thin film as a function of deposition temperature, the films were deposited on MgO (001) single crystal substrates. Because of its high electrical resistivity, MgO has been widely employed as the substrate for electrochemical analysis of thin film samples. Both AC and DC measurements of the GDC thin films on MgO substrates were performed using the in-plane geometry under air in the temperature range of 400–800°C. Fig 4.5 plots the AC impedance spectra of samples deposited at RT, 300ºC, and 700ºC. The measurement temperature was 800ºC. The general trend is that the total resistance of the GDC thin film decreases significantly as the deposition temperature increases. Our previous study showed that the high frequency arc is attributed to the grain boundary resistance of a bulk GDC cell (Pt/GDC/Pt) at low temperature [132-133]. However, the intra-grain and grain boundary resistances of GDC thin film electrolyte are difficult to separate from their AC impedance spectra due to the short time constant and cell geometry. The appearance of one single arc in Nyquist plot is for the thin film electrolyte or nano-scaled electrolyte material according to literatures [126, 128, 134].

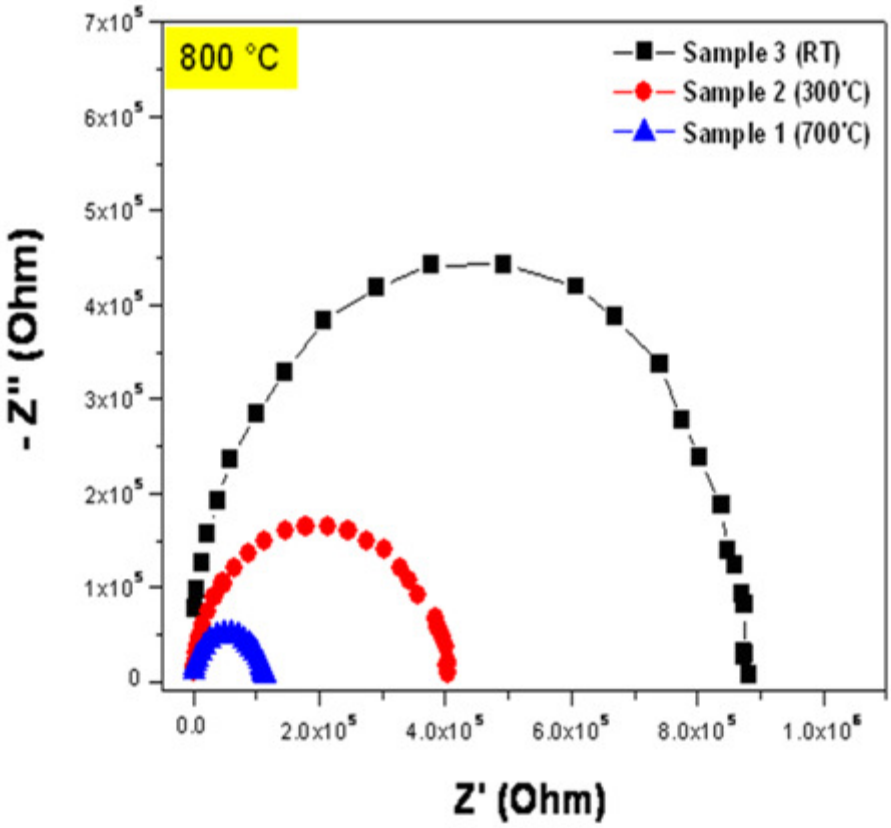

Fig 4.5. AC impedance spectra of Nyquist plots of GDC thin films.

Arrhenius plots of total conductivity versus reciprocal temperature for all of the GDC thin film samples are plotted in Fig 4.6. The solid symbols are for DC electrical measurements and the open symbols are for AC impedance measurements. First, it is interesting to note that the total conductivity results of AC and DC measurements are in good agreement with the sample deposited at 700ºC. One of the main reasons both AC and DC measurements were employed for this study is that the GDC samples deposited at RT and 300^{o}C show very high resistivity during DC conductivity measurement and the measurements could not be completed. A complementary study combining both AC

and DC measurements allows a thorough comparison between all samples. Second, it shows that the sample deposited at 700°C has higher conductivity (7.3 x 10^{-3} Scm^{-1} at 600°C) with lower activation energy (> 0.72 eV) than the ones deposited at RT (3.6 x 10^{-4} Scm^{-1} at 600°C, <1.3 eV). In other words, the total conductivity of the films deposited at high temperature (700°C) is about twenty-times higher than the ones deposited at RT at the measurement temperature of 600^{o}C. It has been reported the grain boundary conductivity has higher activation energy (> 1 eV) compared to that obtained from intra-grain conductivity (~ 0.64 eV) because of defect and impurity segregation in the vicinity of grain boundaries [109, 135-136], which results in a higher conductivity for the GDC films deposited at high temperatures with less grain boundaries. The GDC thin film deposited at 700°C (grain size: ~3 μm) shows an activation energy of 0.72 eV indicating that the overall conductivity is mainly contributed by the intra-grain conductivity. Compared with previous reports on GDC films prepared by similar processing methods [114, 126-128, 134], the GDC films in this study show a relatively higher value of the overall conductivity with a lower activation energy. As the substrate temperature decreases of the GDC thin film, the total conductivity decreases and the activation energy increases because of the poor grain connectivity and the increasing contribution of grain boundary resistivity. For example, the sample deposited at RT has the smallest grain size with poor grain connectivity which limits the transport of ions through the grain boundaries (Figs 4.2(a) and 4.3(a)). This results in the low conductivity in nanocrystalline grains deposited at RT.

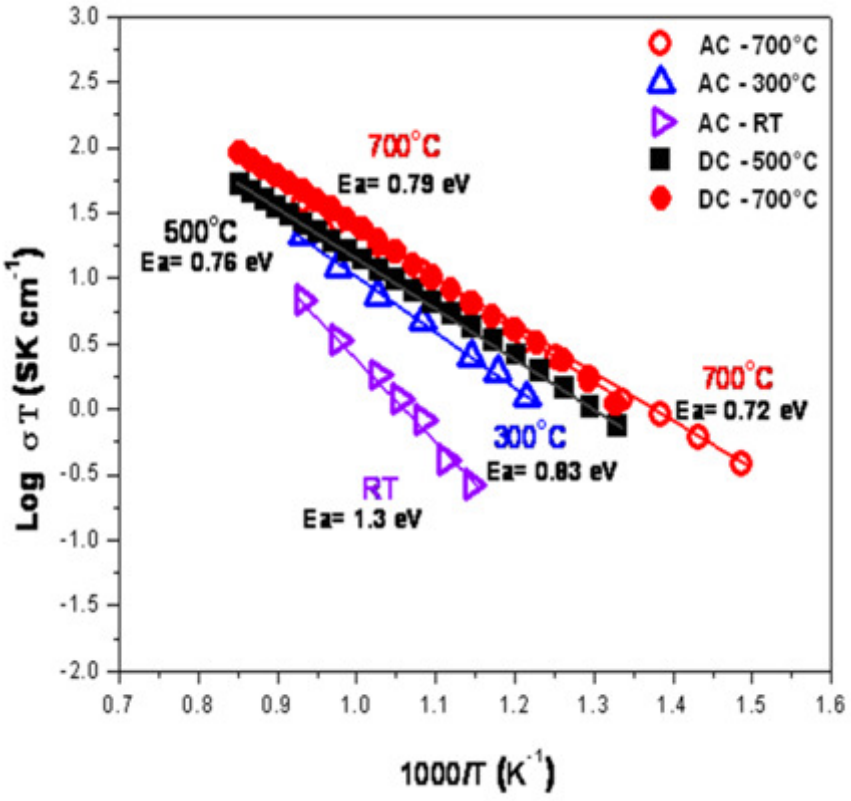

Fig 4.6. Arrhenius plots of total conductivities of GDC thin films as a function of deposition temperature.

Another observation is the different surface morphologies for the samples deposited at different temperatures after the electrical measurement. As shown in Fig 4.7(a), the plan-view SEM image of the film deposited at RT shows obvious microcrack formation after the measurement possibly due to the densification of the grains and grain boundaries during high temperature measurement. The surface remains smooth and crack-free for the samples deposited at higher temperatures (Fig 4.7(b)). This again proves that the low conductivity in the RT sample is due to the poor grain connectivity and the large amount of grain boundaries.

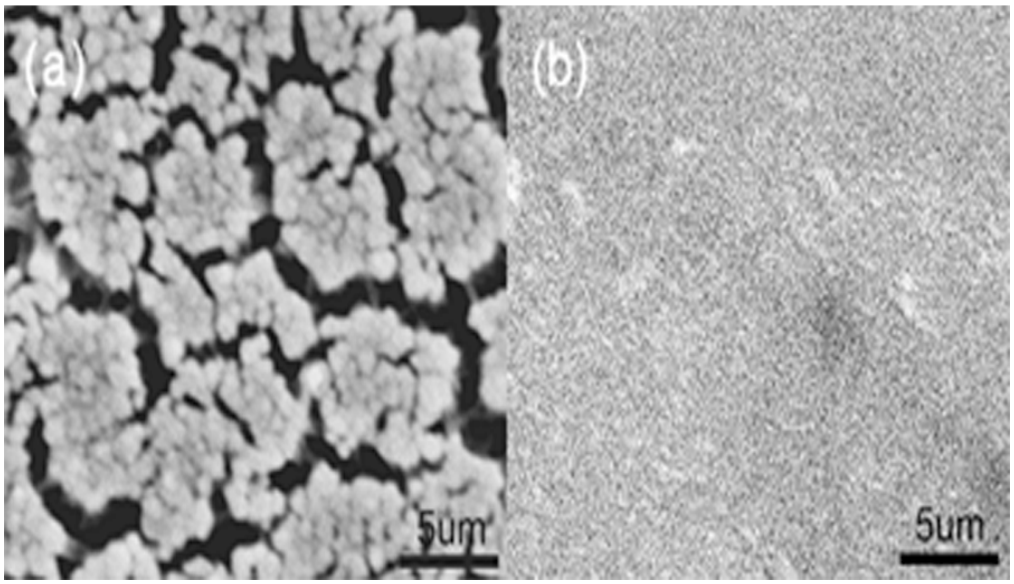

Fig 4.7. Plan-view SEM images of GDC thin films deposited (a) RT, and 500ºC after electrical measurement from 400ºC to 800ºC.

4.5 Conclusions

We have successfully processed GDC thin film electrolyte with different grain sizes at various deposition temperatures. The crystallinity of the films has been found to increase with increasing substrate temperature. The GDC thin film deposited above 500 ºC starts to show epitaxial growth on YSZ substrates. The series of electrical property measurements such as AC and DC measurements as functions of temperature and grain size show that the films with large grains (deposited at higher temperatures) have higher conductivity and lower activation energy than the films with small grains and poor grain connectivity (deposited at lower temperatures). For example, the overall conductivity of the GDC films deposited at 700^{o}C is about twenty-times of that in the RT sample. The present study suggests that substrate temperature significantly influences the microstructure of the GDC films (i.e., grain size and grain morphologies) and its overall electrical properties including ionic conductivity.

CHAPTER V

HIGH POWER DENSITY IN THIN FILM SOFCs WITH YSZ/ GDC BILAYER ELECTROLYTE

5.1 Overview

Bilayer electrolytes composed of a gadolinium-doped CeO_2 (GDC) layer (~6 μm thickness) and an yttria-stabilized ZrO_2 (YSZ) layer with various thicknesses (~330 nm, ~440 nm, and ~1 μm) were deposited by a pulsed laser deposition (PLD) technique for thin film solid oxide fuel cells (TFSOFCs). The bilayer electrolytes were prepared between a NiO-YSZ (60:40 wt.% with 7.5 wt.% carbon) anode and $La_{0.5}Sr_{0.5}CoO_3$-$Ce_{0.9}Gd_{0.1}O_{1.95}$ (50:50 wt.%) composite cathode for anode-supported single cells. Significantly enhanced maximum power density was achieved, i.e., a maximum power density of 188, 430, and 587 $mWcm^{-2}$ was measured in a bilayer electrolyte single cell with ~330 nm thin YSZ at 650, 700, and 750^oC, respectively. The cell with the bilayer electrolyte (YSZ ~330 nm) doubles the overall power output at 750^oC compared to that achieved in the GDC single layer cell.

This signifies that the YSZ thin film serves as a blocking layer for preventing electrical current leakage in the GDC layer and also provides chemical, mechanical, and structural integrity in the cell, which leads to the overall enhanced performance.

---

* Reprinted with permission from "High power density thin film SOFCs with YSZ/GDC bilayer electrolyte" by S. Cho, Y. N. Kim, J.-H. Kim, X. Zhang, A. Manthiram, H. Wang, Electrochimica Acta, 56 (2011) 5472-5477. Copyright (2011).

5.2 Introduction

Lowering the operating temperatures of solid oxide fuel cells (SOFCs) from conventional 900-1000ºC to the intermediate temperature range of 400 ~ 700ºC allows a wider selection of materials for SOFC components, a better thermal integrity of the cells, and thus a longer life time of the cells [137-139]. Electrolyte materials with higher ionic conductivity are needed in order to improve the SOFC efficiency at lower operating temperatures. Typically, yttria-stabilized zirconia (YSZ) is a conventional electrolyte material with high oxygen-ion conductivity of 0.1 S/cm at 1000ºC; however its high operation temperature significantly limits its applications due to the materials' thermomechanical degradation and raises the overall cell costs because of the ceramic interconnects required at high operation temperatures. Much work has been done to integrate thin film technologies on alternative electrolytes such as gadolinia doped-ceria (GDC)**,** lanthanum strontium gallate magnesite (LSGM), and scandia-stabilized zirconia (ScSZ) for intermediate temperature SOFCs [140-143]. Among them, GDC has been considered as one of the most promising electrolyte materials for the development of intermediate temperature SOFCs because of its high ionic conductivity [144-148]. However, one main limitation of the GDC electrolyte is its mixed ionic and electronic conduction (MIEC), i.e., higher electronic conductivity with decreasing theoretical voltage caused by the reduction of ceria from Ce^{4+} to Ce^{3+} from the anode side where the electrolyte is exposed to a reducing atmosphere. This leads to a lower open circuit voltage (OCV) and a consequent decrease in overall power output. To improve GDC's chemical/ mechanical stability and reduce the OCV loss under reducing conditions, one

effective approach reported in bulk electrolyte structure is to incorporate YSZ as a blocking layer in between the GDC and anode for inhibiting chemical reduction of GDC and electrical current leakage [149-152]. Previous studies have shown improvement in the open circuit voltage of an YSZ/GDC bilayer electrolyte cell processed by wet ceramic co-sintering process [153-154], sol-gel dip-drawing method [151], and drop coating method [155]. However, the incorporation of thick-YSZ layer will increase ohmic loss in SOFCs due to the lower ionic conductivity of YSZ in comparison with the GDC at intermediate temperatures. Therefore, it is necessary to optimize the YSZ thickness for achieving the optimum cell performance of the bilayer electrolyte cells.

In this work, we demonstrate a well designed bilayer GDC (~6 μm)/ YSZ electrolyte structure using a thin film approach, where the thickness of the YSZ layer is carefully controlled from ~330 nm to ~1 μm to explore the effect of YSZ thickness on the overall performance of the bilayer electrolyte cells. Using this approach, it is possible to identify the optimum YSZ interlayer thickness that effectively suppresses a significant cell voltage drop without reducing the ionic conductivity in the GDC electrolyte.

5.3 Experimental

The depositions of thin films of the GDC electrolyte, YSZ electrolyte and $La_{0.5}Sr_{0.5}CoO_3$ (LSCO)-GDC cathode were performed under varying oxygen partial pressure with a KrF excimer laser (Lambda Physik 210, λ = 248 nm, 5-10 *Hz*) using a pulsed laser deposition (PLD) technique. The laser beam was focused to obtain an energy density of approximately 5 J cm^{-2} at a 45º angle of incidence. For the depositions,

various substrates including $SrTiO_3$ (STO) (001), MgO (001), and pressed NiO-YSZ (60:40wt.%) with 7.5 wt.% carbon anode disks were selected for this work. The pressed targets such as LSCO-GDC (50:50 wt.%), 8 mol% YSZ, and GDC ($Ce_{0.9}Gd_{0.1}O_{1.95}$) were all prepared by mixing stoichiometric amounts of the raw powders including La_2O_3, $Sr(NO_3)_2$, Co_3O_4, CeO_2, and Gd_2O_3. For preparing the anode substrates, powders of 8 mol% YSZ (Tosoh Co), NiO (Sumitomo Chemical Co), and carbon (Kuraray Chemical Co) were mixed in the ratios of 60 wt.% NiO, 40 wt.% YSZ, and 7.5 wt.% carbon, respectively, and were ball milled for 20 hrs. We added carbon as a pore former into the anode powder to avoid concentration polarization under high current drain due to the effect of anode porosity and limited fuel supply that was observed in our previous work [156].

The resulting NiO-YSZ with 7.5 wt.% carbon cermet powders was compacted into disks under uniaxial pressure using a die set of 1 inch in diameter and sintered at 1300 ºC for 3 hrs. YSZ interlayers with various thicknesses (330 nm ~ 1 μm) with 6 μm GDC film and 100 nm LSCO-GDC composite cathode layer were deposited on the NiO-YSZ anode disk substrates under the stated conditions by PLD. The growth rates of these thin films were about 1 nm/s for LSCO-GDC cathode layer under an oxygen partial pressure of 200 mTorr, and ~0.9 Å/s for the YSZ and GDC layers in a 20 mTorr oxygen partial pressure. The substrate temperature was varied from 300 to 500ºC to optimize the film crystallinity and the nanopore size of the cathode layer. For a thick cathode layer, LSCO-GDC powder mixed with an organic binder (Heraeus V006) was applied onto the sample by screen printing method. The cathode is about 30 μm after annealing at 1150

^{o}C for 2 hrs. Microstructural characterizations of these films were performed by cross-sectional transmission electron microscopy (TEM, JEOL2010). Surface morphology study for the thin films was conducted by scanning electron microscopy (SEM). The electrochemical cells were prepared with the in-plane configuration. Two rectangular platinum strips (Heraeus CL11-5100, Pt ink) on the thin film were prepared by screen printing method and platinum grids were used as current collectors. Total conductivity of thin film electrolytes was conducted using AC impedance measurement in the frequency range of 10^{-1} – 30M*Hz* from 325 to 700ºC in air. The effect of YSZ layers on the cell performance was evaluated with anode-supported single cells consisting of LSCO-GDC/bilayer/NiO-YSZ using a potentiostat (Autolab-Eco Chemie BV). During the single cell performance test, humidified H_2 (~3% H_2O at 25ºC) and air were supplied as fuel and oxidant, respectively, at a constant flow rate of 100 mL min^{-1}. The effective electrode area of the cell was 1.13 cm^2. Measurement details can be found elsewhere [156-157].

5.4 Results and Discussions

YSZ/GDC bilayer samples with different thicknesses of YSZ layer (from ~330 nm to ~1 μm) were first deposited on top of single crystalline substrates for microstructure characterizations.

Fig 5.1 shows XRD patterns of a GDC single layer sample and YSZ/GDC bilayer samples that were deposited on the MgO (100) substrates at 500ºC. The YSZ and GDC have very similar crystal structures with the lattice parameter of 0.5147 nm for YSZ and 0.5418 nm for GDC. It is interesting to note that the thin film texture was completely different for the GDC layers with and without the YSZ layer. The growth of the GDC single layer shows a preferred (111) orientation in Fig 5.1(a). As shown in Fig 5.1(b), GDC shows a very strong textured growth along (00*l*) indicating that the GDC film shows predominantly c-axis orientation on the YSZ buffered MgO substrate, i.e., the YSZ buffer layer enables the cube-on-cube growth of GDC on MgO substrates.

Cross-sectional TEM images of GDC single layer and YSZ/GDC bilayer electrolyte structures are shown in Fig 5.2. The GDC single layer shows a columnar structure on STO substrate in Fig 5.2(a). As clearly observed from TEM images in Fig 5.2(b)-(d), the YSZ interlayer thickness varies from ~330 nm to ~1 μm. The interfaces between GDC, YSZ and STO substrate are very clean without any indication of interfacial reactions.

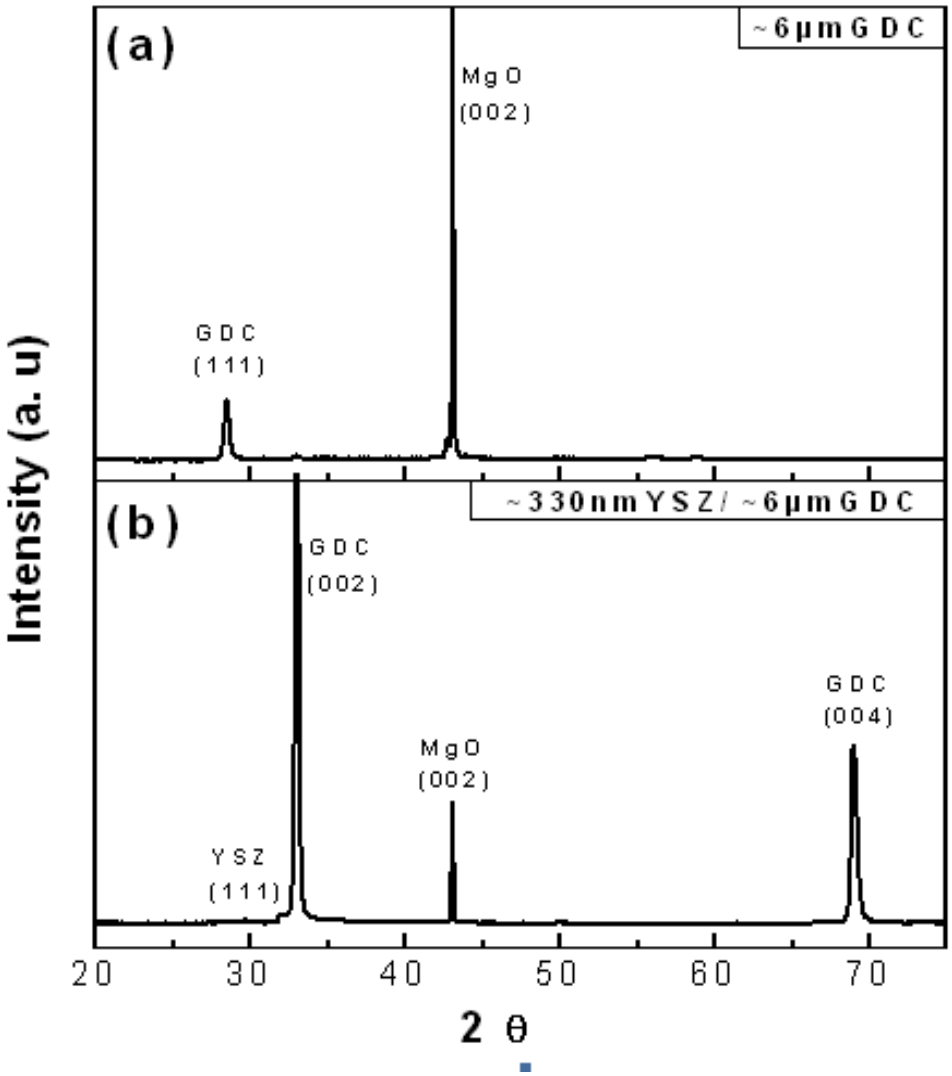

Fig 5.1. XRD patterns of (a) GDC single layer and (b) ~330nm YSZ/GDC bilayer.

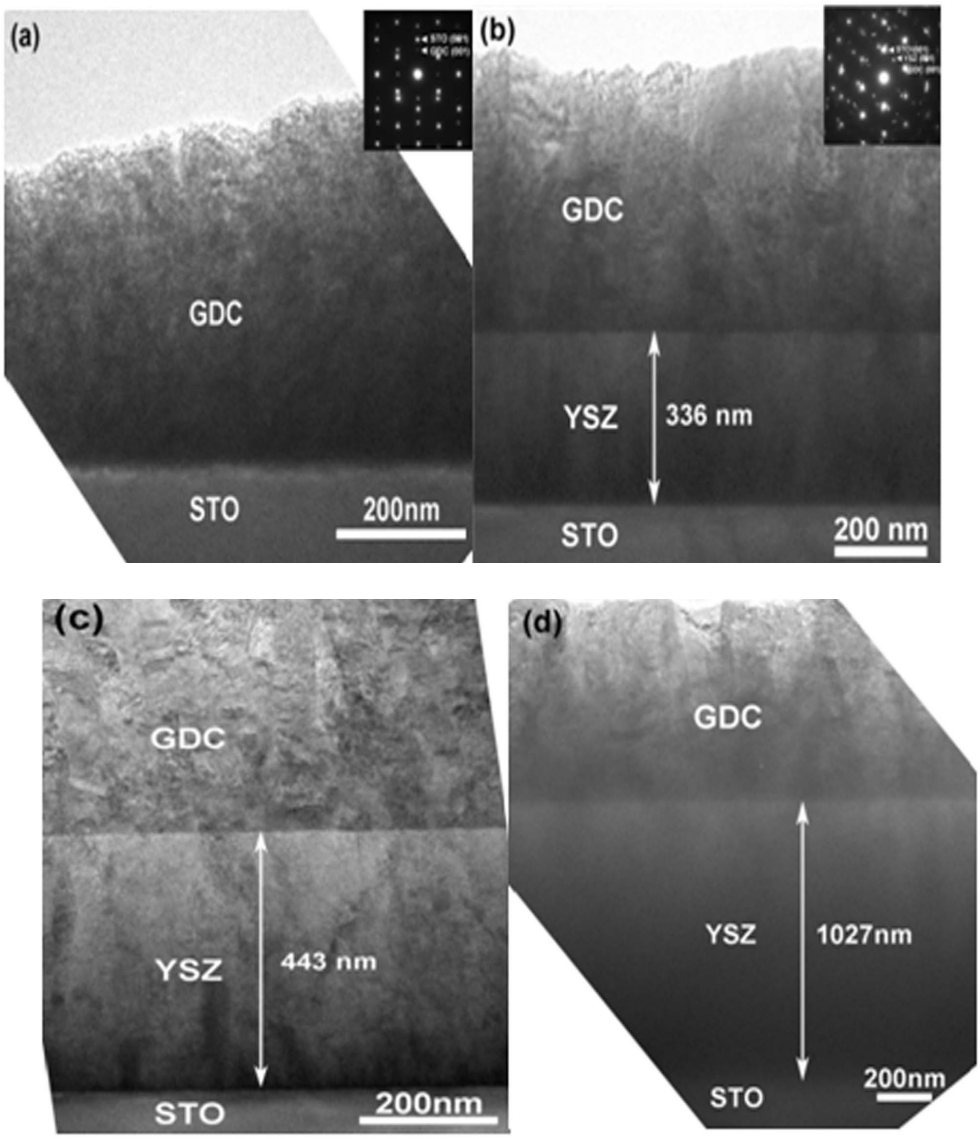

Fig 5.2. **C**ross-sectional TEM images of YSZ/GDC bilayer thin films: (a) GDC single layer, (b) ~330 nm YSZ/GDC bilayer, (c) ~440 nm YSZ/GDC bilayer, and (d) ~1 μm YSZ/GDC bilayer.

The films are dense and smooth for all four cases. The corresponding selected area diffraction patterns (SAD, insets in Fig 5.2(a) and 5.2(b)) show the diffraction dots from both the film and substrate indicating the good crystallinity for both cases. It is found that the GDC layer matches well with STO substrate (a=0.390 nm) after a 45° in-plane rotation. To further examine the microstructure across the electrolyte films, we conducted high resolution cross-sectional TEM study on the GDC layer, YSZ interlayer, and YSZ/GDC bilayer thin films on STO substrates as shown in Fig 5.3. The GDC film grows as an epitaxial film with clear lattice fringes seen in Fig 5.3(a). YSZ interlayer shows a fully dense columnar grain structure with the columnar grain boundaries outlined in Fig 5.3(b). Furthermore, Fig 5.3(c) shows that the interface between the YSZ and GDC layers is apparently clean without intermixing.

To compare the total conductivity of the YSZ/GDC bilayer thin films, the set of YSZ/GDC bilayer samples on MgO (100) substrates were measured by AC impedance under air in a temperature range of 325–700°C.

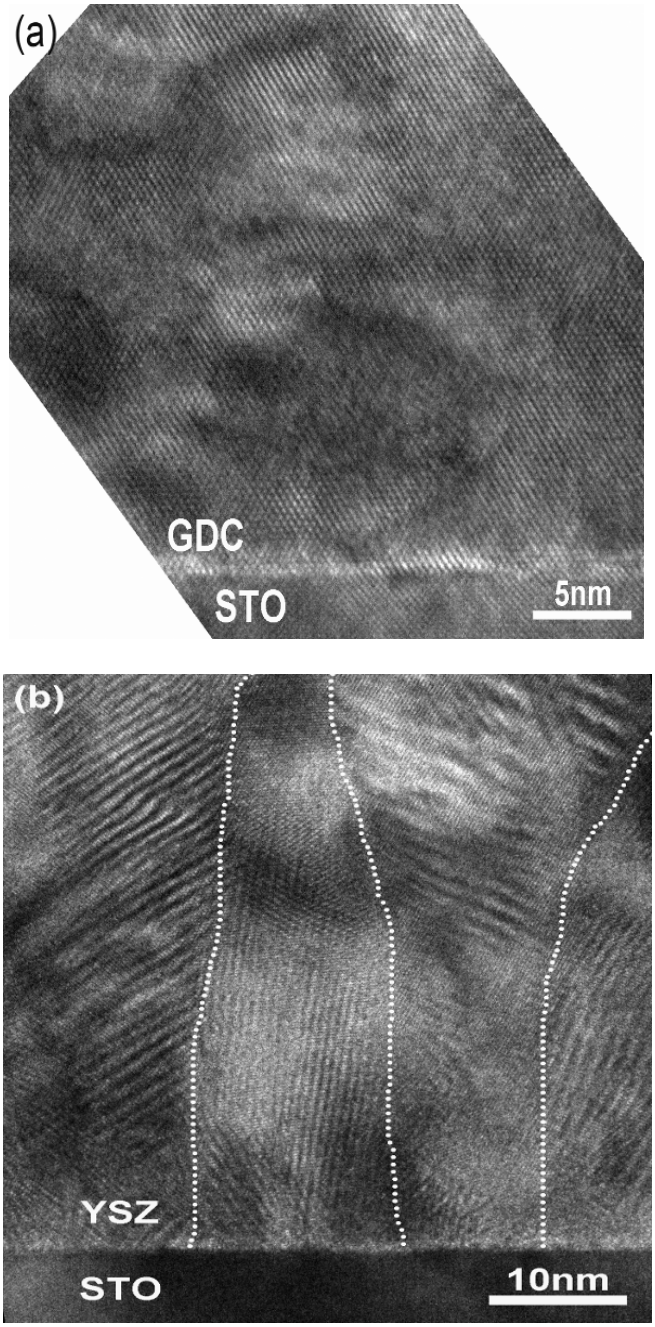

Fig 5.3. High resolution cross-sectional TEM images of YSZ/GDC bilayer thin films (a) GDC thin film, (b) YSZ thin film, and (c) interface between GDC and YSZ.

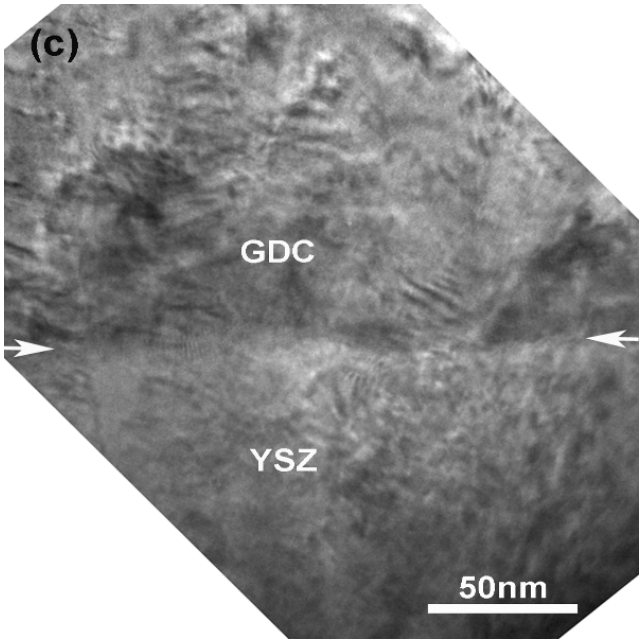

Fig 5.3. Continued.

As shown in Fig 5.4, the AC impedance spectra of bilayer samples were plotted at 450ºC. Our earlier study showed a single arc from the GDC thin film in the Nyquist plot because it was difficult to obtain two well-separated intra-grain and grain boundary resistances due to the short time constant and cell geometry [117, 120, 158]. Similarly, the YSZ/GDC bilayer thin films also exhibit one semicircle at high frequency regime, while the low frequency arc corresponds to the Pt electrode as shown in Fig 5.4. Based on the results, the total resistance of the YSZ/GDC bilayer film increases by increasing the YSZ film thickness, which indicates the YSZ layer, has a lower conductivity at low temperature regimes.

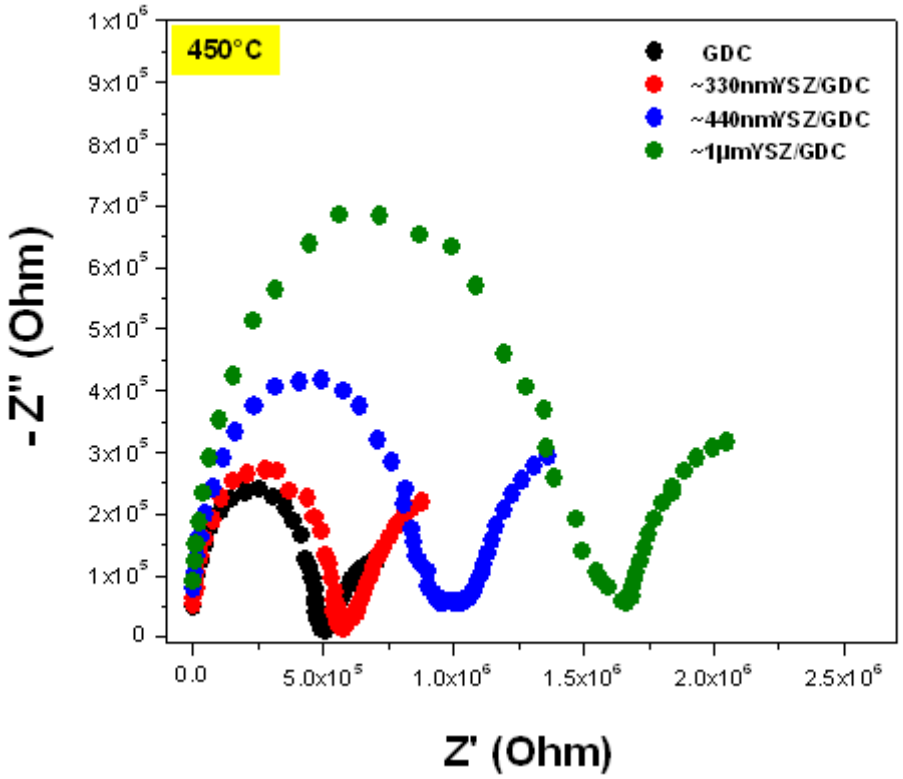

Fig 5.4. AC impedance spectra of Nyquist plots of YSZ/GDC bilayer thin films.

Arrhenius plots of the total conductivity versus reciprocal temperature in Fig 5.5 are derived from the AC impedance spectra for a comparison between the total conductivities of the GDC single layer and YSZ/GDC bilayers as a function of the YSZ film thickness. All samples show a similar range of activation energies of 0.75 – 0.78 eV since the overall conductivity is mainly contributed by the intra-grain conductivity at intermediate operating temperatures according to our previous results [159]. Although the AC impedance study shows a decrease of the electrical conductivity with the YSZ incorporation (Fig 5.5), it should be noted that the measurement was performed in air,

where GDC remains as a pure oxide ion conductor. In actual single cell configuration, however, the GDC electrolyte will be reduced from the anode side in contact with fuels that results in OCV loss and consequent deterioration of SOFC performance. Therefore, the effect of the YSZ/GDC bilayer on the OCV and fuel cell performance has been evaluated using NiO-YSZ anode-supported single cells.

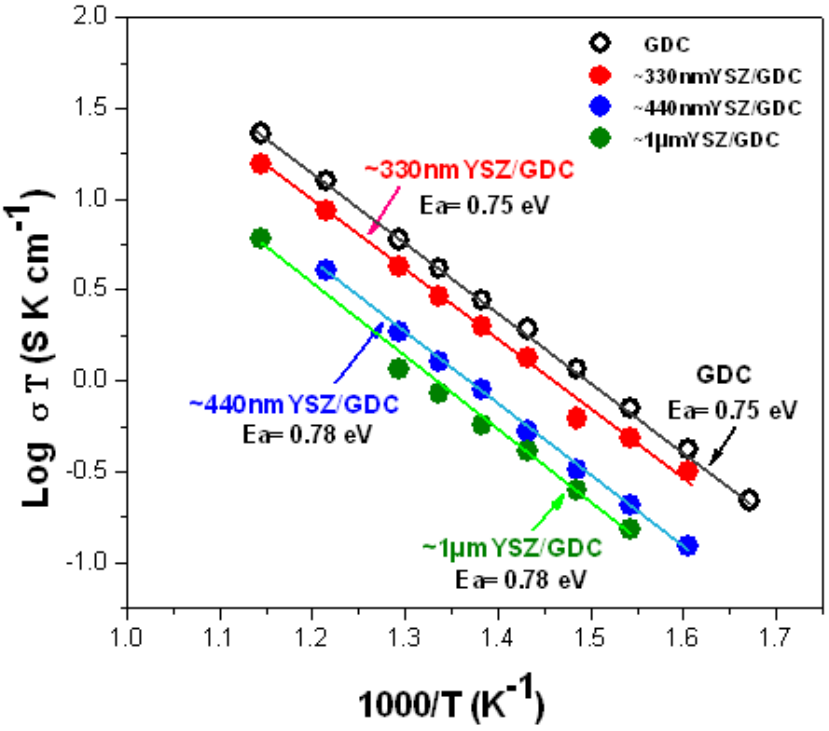

Fig 5.5. Arrhenius plots of the total conductivities of YSZ/GDC thin films with various thicknesses of YSZ.

The I-V characteristics and power densities of anode-supported single cells were examined in a temperature range of 650 – 750 ^{o}C. In Fig 5.6(a), maximum power densities of the cell with only the GDC single layer electrolyte (~6 μm) were measured to be 198, 263, and 315 mWcm^{-2} (highlighted as red arrow) at 650, 700, and 750^{o}C, respectively. The cell provided the OCV of 0.5V at 750^{o}C. However, a dramatic enhancement in the power performance and the OCV were observed in the bilayer electrolyte cells. For a cell with thinner YSZ (~330 nm)/GDC (~6 μm) bilayer electrolyte, as shown in Fig 5.6(b), the maximum power densities increase to 188, 430, and 587 mWcm^{-2} (highlighted as red arrow) at 650, 700, and 750^{o}C, respectively, and the OCV is 0.67 V at 750^{o}C. The SOFC with thicker YSZ (~1 μm) layer shows an appreciable increase of OCV (1.05 V) with high power densities of 301 and 438 mWcm^{-2} (highlighted as red arrow) at 700 and 750^{o}C, respectively. From the power measurement results, one can conclude the following. First, the YSZ thickness plays an important role in the OCVs in all cells. For example, the measured OCVs of the bilayer electrolyte cells were improved to > 0.67 V (~330 nm thickness) and > 1.05 V (~1 μm thickness) as the YSZ layer thickness increases. It was reported that the interfacial oxygen partial pressure increases linearly with the decrease in the thickness ratio of YSZ/GDC, which causes a reduction in the n-type conductivity of the GDC at the YSZ/GDC interface, a decrease in the penetration electronic current through the bilayer and an increase in the OCV [125, 160-161]. Second, superior chemical stability was achieved by the YSZ layer, resulting in the enhanced cell performance. It is interesting to note that sufficient YSZ thin film in the cell can suppress ceria reduction on the anode

side, thus generating higher power output than the GDC single layer cell. For example, he bilayer electrolyte cell with the thin YSZ layer of ~330 nm (Fig 5.6(b)) doubles the maximum power density at 750°C.

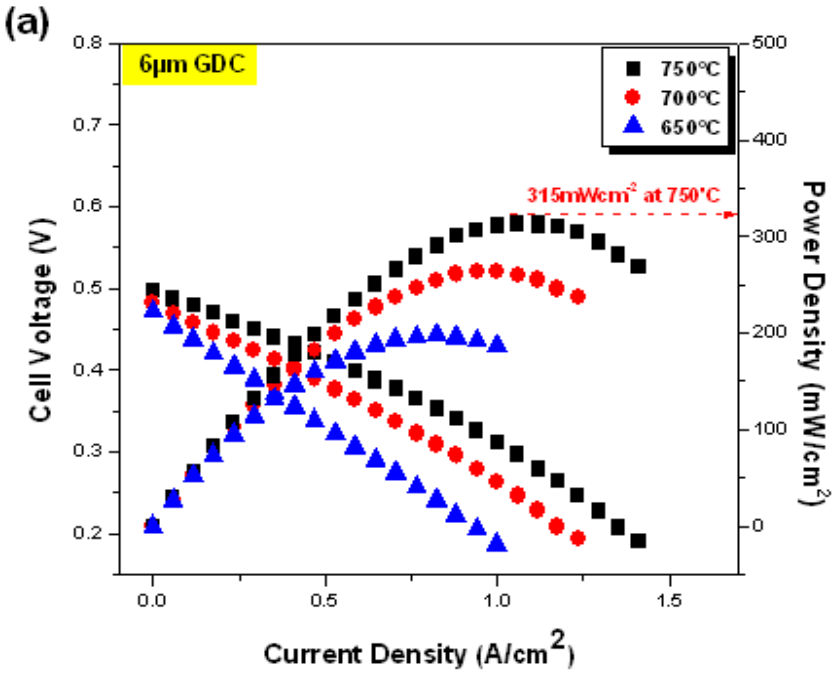

Fig 5.6. Cell voltages and power densities of anode-supported single cells as a function of current densities at different temperatures (650 ~ 750°C): (a) ~6 μm GDC single layer electrolyte, (b) ~330 nm YSZ/GDC bilayer electrolyte, and (c) ~1μm YSZ/GDC bilayer electrolyte.

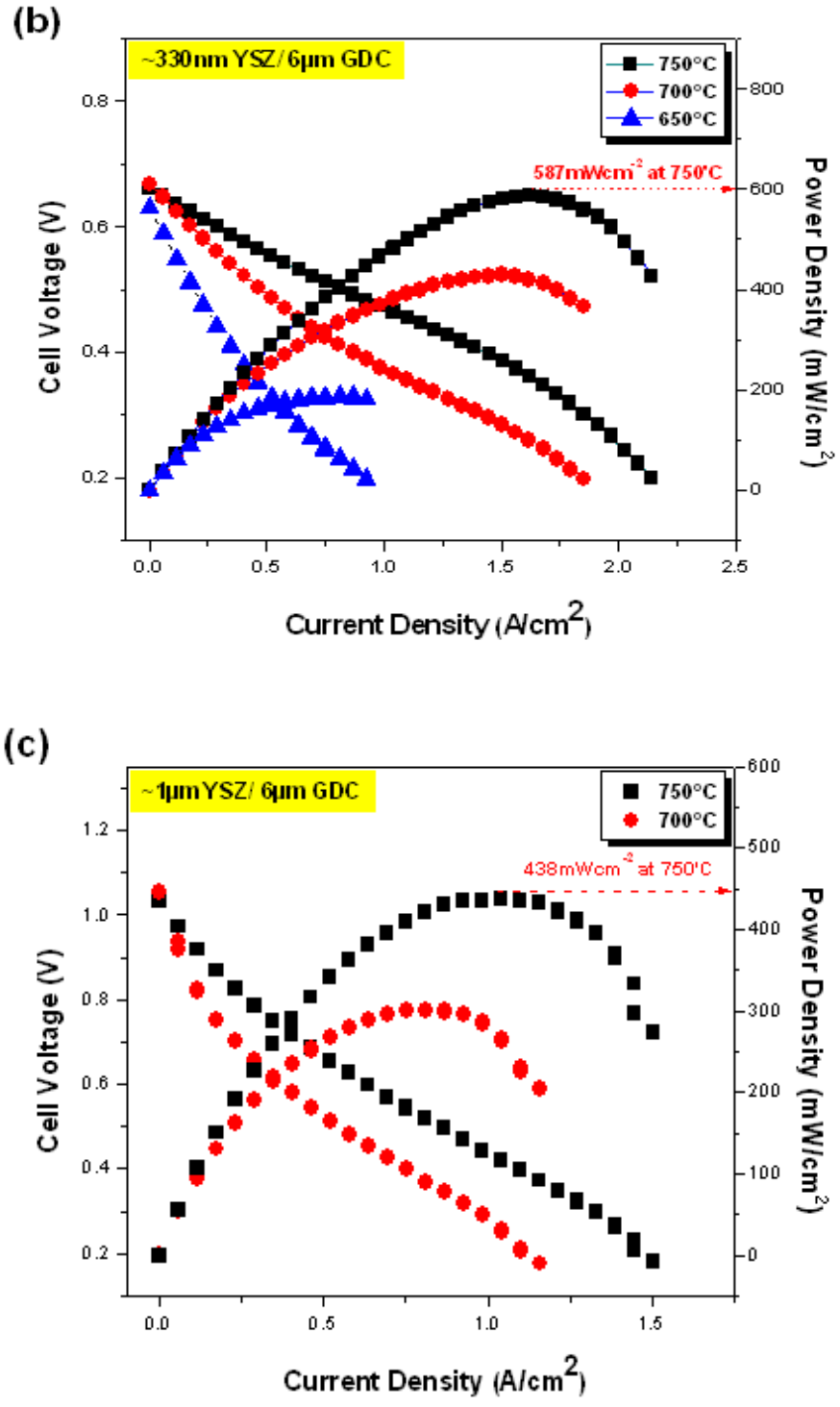

Fig 5.6. Continued.

Fig 5.7 shows the cross-sectional SEM images of anode-supported single cells after the cell performance measurements at high temperatures. The microstructures of both the ~6 μm GDC single layer (Fig 5.7(a)) and ~1 μm YSZ/~6 μm GDC bilayer electrolyte (Fig 5.7(b)) show fully dense layer structures between the cathode and anode electrodes. A clear interface can be seen between the YSZ and GDC layers in the YSZ/GDC bilayer electrolyte in Fig 5.7(b). The LSCO-GDC composite cathode and NiO-YSZ anode exhibit a porous structure as required for the SOFC applications. It is obvious that the electrolyte layers remain dense and solid after the high temperature measurements and the adhesion between the adjacent layers is excellent without any obvious crack formation at interfaces. Based on the above microstructural, electrochemical, and power measurement results, it is evident that a tailored bilayer electrolyte is needed for the optimization of power density characteristic and electrolyte stability, i.e., the bilayer electrolyte structure with a proper YSZ thickness can enable the chemical, mechanical, and structural stability of the YSZ/GDC electrolyte in the single cells.

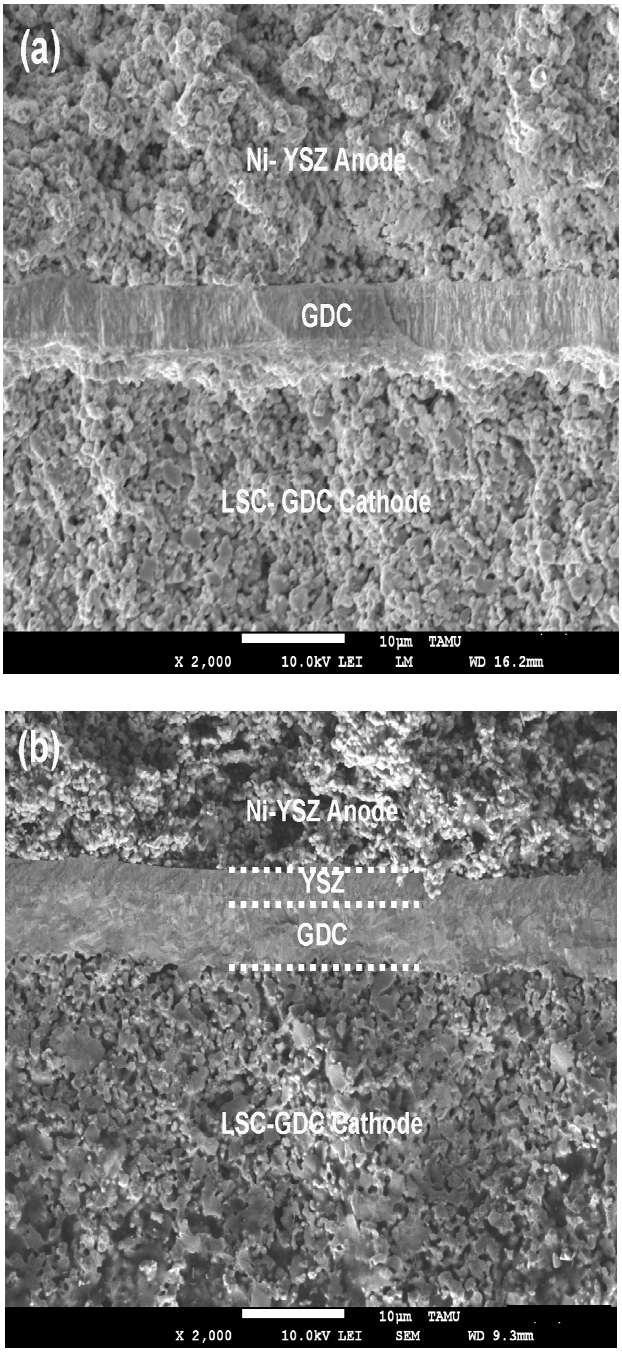

Fig 5.7. Cross-sectional SEM images of YSZ/GDC bilayer electrolyte single cells: (a) the cell with GDC single layer electrolyte, (b) the cell with YSZ/GDC bilayer electrolyte.

5.5 Conclusions

We have successfully investigated the microstructural and electrochemical properties of the YSZ/GDC (~6 μm) bilayer electrolytes with the YSZ thickness varied from ~330 nm to ~1 μm for thin film SOFCs. The total conductivity of the bilayer films is found to be inversely proportional to YSZ film thickness at the intermediate operating temperatures in air. However, the single cells with the YSZ (~330 nm thickness)/GDC bilayer electrolyte double the overall power output at 750^{o}C compared to that obtained with the GDC single electrolyte layer. The YSZ/GDC bilayer electrolyte has shown the effectiveness of YSZ as an electron blocking layer. The bilayer structure improves the cell voltage by shifting the potential displacement at the electrolyte interface under the reducing conditions. Therefore, the ceria-based electrolyte with the thin YSZ interlayer presents a feasible architecture for enhancing the overall power density and enabling chemical, mechanical, and structural stability in the cells.

CHAPTER VI

MICROSTRUCTURE AND ELECTROCHEMICAL PROPERTIES OF PBCO/GDC VERTICALLY ALIGNED NANOCOMPOSITE THIN FILM AS INTERLAYER FOR THIN FILM SOLID OXIDE FUEL CELLS

6.1 Overview

A thin layer of a vertically aligned nanocomposite (VAN) structure of $PrBaCo_2O_{5+\delta}$ (PBCO) and $Ce_{0.9}Gd_{0.1}O_{1.95}$ (GDC) between the cathode and the electrolyte was demonstrated by a pulsed laser deposition (PLD) technique for thin film solid oxide fuel cells (TFSOFCs). The VAN structured PBCO/GDC thin film shows high quality epitaxial growth on the single crystal $SrTiO_3$ substrate at high deposition temperatures. It also has a lattice matching relation between the PBCO and GDC nanocolumns. The symmetric cells with the VAN interlayer are found to have a lower area specific resistance (ASR) of 2.1 Ωcm^2 compared to that of the ones without interlayer (2.5 Ωcm^2) at 400°C. The maximum power density of the single cell prepared with the VAN interlayer was 151, 263, and 350 $mWcm^{-2}$ at 650, 700, and 750°C, respectively, with an open circuit voltage (OCV) of 0.88 V at 750 °C. The PBCO/GDC VAN interlayer could perform as a transition layer that enhances adhesion and relieves stress from different thermal expansion coefficients and lattice parameters between the cathode and the electrolyte in TFSOFCs.

6.2 Introduction

Solid oxide fuel cells (SOFCs) are considered to be one of the most promising energy conversion devices because of their high energy conversion efficiency. To enable their wide applications, intermediate operation temperature SOFCs (400 ~ 700ºC) are needed for the considerations of cost reductions (material, manufacturing process), structural integrity of the cells, extensive selection of SOFC materials, and longevity of the cells [162]. However, the increased cathode polarization resistance at low operating temperatures becomes one of the major limiting factors in the overall performance of the intermediate temperature SOFCs. The general requirement of the SOFC cathode material is a high oxygen reduction rate which is firmly limited to triple phase boundary (TPB) sites where the oxygen molecules merge with electrons and form into ions. An extension of the TPB active zone over the entire cathode plays an important role to increase the cell performance. In this aspect, many oxide materials containing Fe, Mn, Co and Ni have been studied for the cathode materials [163-166] and several perovskite-types mixed ionic electronic conductor (MIEC) ceramic materials with doped $LaCoO_3$, $BaCoO_3$, and $SmCoO_3$ have been introduced as a promising cathode candidate for intermediate temperatures SOFCs [167-169]. Recently, as a new cathode material of the layered or double perovskite-type structure with ordered A-cations, $PrBaCo_2O_{5+\delta}$ is found to be a potential cathode candidate for SOFCs because of its high electronic conductivity, rapid oxygen ion diffusion, and surface exchange kinetics at intermediate temperatures. It has been reported that the distribution of vacancies could greatly

improve the diffusivity of oxide ions in the bulk material and possibly provides surface defect sites with enhanced reactivity towards molecular oxygen [170-175].

On the other hand, existing materials with new nanostructures could also provide enhanced cell performance. A vertically aligned nanocomposite (VAN) structure of LSCO/GDC as an interlayer between the cathode and the electrolyte has been demonstrated and effectively increased the cathode/electrolyte interface as well as the TPBs and thus lead to the enhanced power density of the cells [176]. This again suggests that the microstructural variations in the electrolyte and the electrode could affect the reaction kinetics of the cell and the main power loss occurs due to the polarization resistance at the cathode/electrolyte interface in SOFCs. It is consistent with previous reports [177-182]. Here, a new binary VAN interlayer consisted of the new cathode material, $PrBaCo_2O_{5+\delta}$ (PBCO), and the electrolyte, $Ce_{0.9}Gd_{0.1}O_{1.95}$ (GDC), is deposited for thin film SOFCs (TFSOFCs). A schematic sketch of the binary VAN interlayer is given in Fig 6.1(a) and (b). The goal of this work is to enable this new VAN structure through optimizing the deposition parameters and implementing the VAN structure in single cells. This new cell structure could take the advantage of the new cathode material as well as the increased cathode/electrolyte interfacial area and achieve a better overall cell performance.

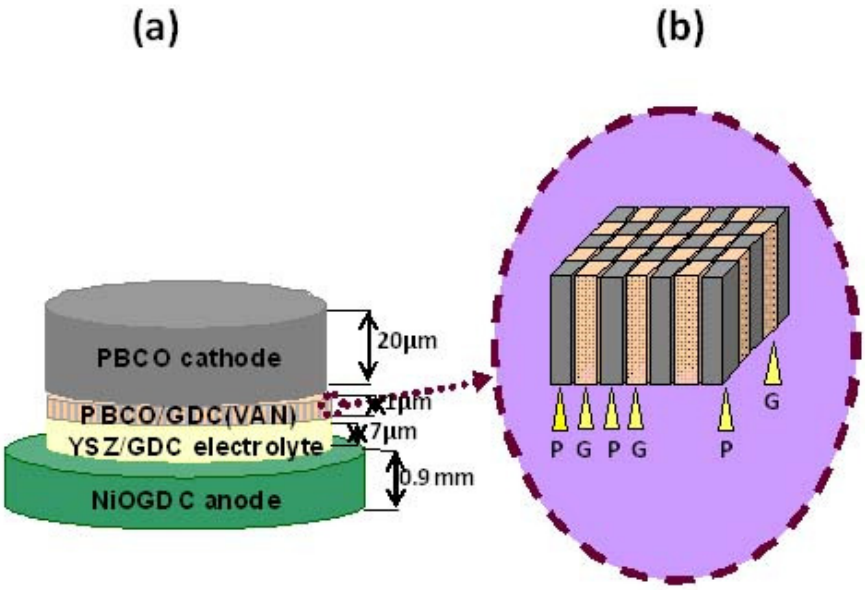

Fig 6.1. (a) Schematic diagram of anode supported single cell and (b) VAN interlayer where "P" and "G" stand, respectively, for PBCO and GDC columns.

6.3 Experimental

Thin film depositions of the yttria-stabilized ZrO_2 (YSZ) / GDC electrolyte, and the $PrBaCo_2O_{5+\delta}$ (PBCO)-GDC cathode were performed using a KrF excimer laser (Lambda Physik 210, λ = 248 nm, 2-10 *Hz*) in a pulsed laser deposition (PLD) chamber. The laser beam was focused to obtain an energy density of approximately 5 J cm^{-2} at a 45º angle of incidence. Oxygen partial pressure was varied for optimization of the depositions. Various substrates such as $SrTiO_3$ (STO) (001), pressed GDC ($Ce_{0.9}Gd_{0.1}O_{1.95}$), and 60wt% NiO + 40wt% $Ce_{0.8}Gd_{0.2}O_{1.95}$ (NiO-GDC, Praxair Inc) anode disks were selected for the VAN growth, symmetric cell growth and single cell

deposition, respectively. The pressed targets of PBCO-GDC (50:50 wt.%), 8 mol% YSZ, and GDC ($Ce_{0.9}Gd_{0.1}O_{1.95}$) were all prepared by mixing the stoichiometric amounts of raw powders. To make the PBCO powder, the raw powders including Pr_6O_{11}, $BaCO_3$, and Co_3O_4 were mixed in ethanol and calcinated at 1000ºC for 12 hrs in air. The calcinated powders were then grounded, pressed into pellets, and annealed at 1200ºC for 12 hrs in air. The anode substrates were prepared with 5 wt.% starch as a pore former to increase the anode porosity. The NiO-GDC anode powders were ball milled for 48 hrs and then the resultant NiO-GDC with 5 wt.% starch cermet powder was compacted into disks under a uniaxial press using a die set of 1 inch in diameter and sintered at 1300ºC for 3 hrs in air.

~1 μm YSZ / ~6 μm GDC electrolyte and ~800 nm PBCO-GDC composite cathode films were deposited on the NiO-GDC anode substrates under the stated conditions by PLD. The growth rates of these thin films were about ~0.86Å /s at 600ºC and ~0.64 Å /s at 750ºC for PBCO-GDC interlayer under an oxygen partial pressure of 200 mTorr and ~1.4 Å/s and 3.2 Å/s for the YSZ and GDC layers in an oxygen partial pressure of 20 mTorr. The substrate temperature was varied from 300 to 750ºC to optimize the film crystallinity and the nanostructure of the interlayer. To make a thick cathode layer, the PBCO-GDC powder is mixed with an organic binder (Heraeus V006) was applied onto the sample by the screen printing method. The cathode is about ~20 μm after annealing at 1150 ^{o}C for 5 hrs in air. Microstructural characterizations of these films were performed by the cross-sectional transmission electron microscopy (TEM, JEOL2010). Surface morphology study for the thin films was conducted with a field

emission scanning electron microscopy (FESEM). The symmetric cells were fabricated and subsequently conducted for electrochemical evaluation using AC impedance analyzer (Gamry Instruments) in the frequency range of 10^{-2} – 300K*Hz* from 350 to 650ºC in air. The cell performance with the PBCO-GDC interlayer was examined with an anode-supported single cell consisted of PBCO/PBCO-GDC/electrolyte/NiO-GDC using a potentiostat (Autolab-Eco Chemie BV). During the single cell performance test, humidified H_2 (~3% H_2O at 25ºC) and air were supplied as a fuel and oxidant, respectively, at a constant flow rate of 100 mL min^{-1}. The effective electrode area of the cell was 1.13 cm^2. Measurement details can be found elsewhere [176].

6.4 Results and Discussions

The microstructural characterization of PBCO and PBCO/GDC thin films was first performed by X-ray diffraction (XRD). A set of PBCO/GDC nanocomposite films were prepared on STO (001) substrates in the temperature range of 300-750ºC. Fig 6.2 shows the XRD patterns of the PBCO thin film, and the PBCO/GDC nanocomposite films deposited at 500ºC and 650ºC, respectively. The film thickness of the PBCO and PBCO/GDC films is ~40 nm and ~100 nm, respectively. The PBCO thin film in Fig. 6. 2(a) is orientated dominantly along the *c*-axis and all PBCO peaks are very close to the STO peaks e.g., the PBCO (002) diffraction peak (c= 0.7636 nm) is almost overlapped with the STO (001) peak (a=0.3904 nm). The PBCO/GDC nanocomposite film shows a similar structure as the PBCO thin film with highly textured growth along (00*l*) orientation as shown in Fig. 6. 2(b). Note that the XRD pattern of the PBCO thin film

exhibits excellent crystallinity with the deposition temperature beyond 500ºC. In addition, the strain state of both films can be concluded as the following. First, the calculated out-of-plane lattice parameter of the PBCO thin film is 0.780 nm based on PBCO (002) peak position, which is in tension out-of- plane on STO substrate compared to that of its bulk lattice parameter (c=0.7636 nm). Second, the PBCO phase in PBCO/GDC nanocomposite film has a higher tensile stress along the out-of–plane direction based on the calculated lattice parameter of 0.790 nm. This suggests that a further tensile stress is introduced by the GDC secondary phase.

Fig. 6. 3 shows cross-sectional TEM images of the PBCO/GDC thin films on STO substrates. In Fig. 6. 3(a), the binary VAN thin film deposited at 600ºC grows as a columnar structure with two phases clearly separated. The one deposited at 750ºC (Fig. 6. 3(b)) instead shows an interesting nanolayered structure within the pillars.

High resolution cross-sectional TEM images of the PBCO/GDC thin films at different temperatures are shown in Fig 6.4–5. The film deposited at 600ºC shows a typical VAN structure with excellent epitaxial quality (Fig 6.4(a)). The corresponding selected area diffraction pattern (SAD, inset in Fig 6.4(a)) shows the distinguished diffraction dots from both the film and substrate indicating the excellent epitaxial quality of the VAN film. In Fig 6.4(b), clear alternating columns of PBCO and GDC are shown in the high resolution TEM image. The average column width for the PBCO and GDC is ~9 nm and ~7 nm, respectively. High angle annular dark field (HAADF) images were taken under STEM mode. It is also called Z-contrast image, where the contrast is proportional to Z^2.

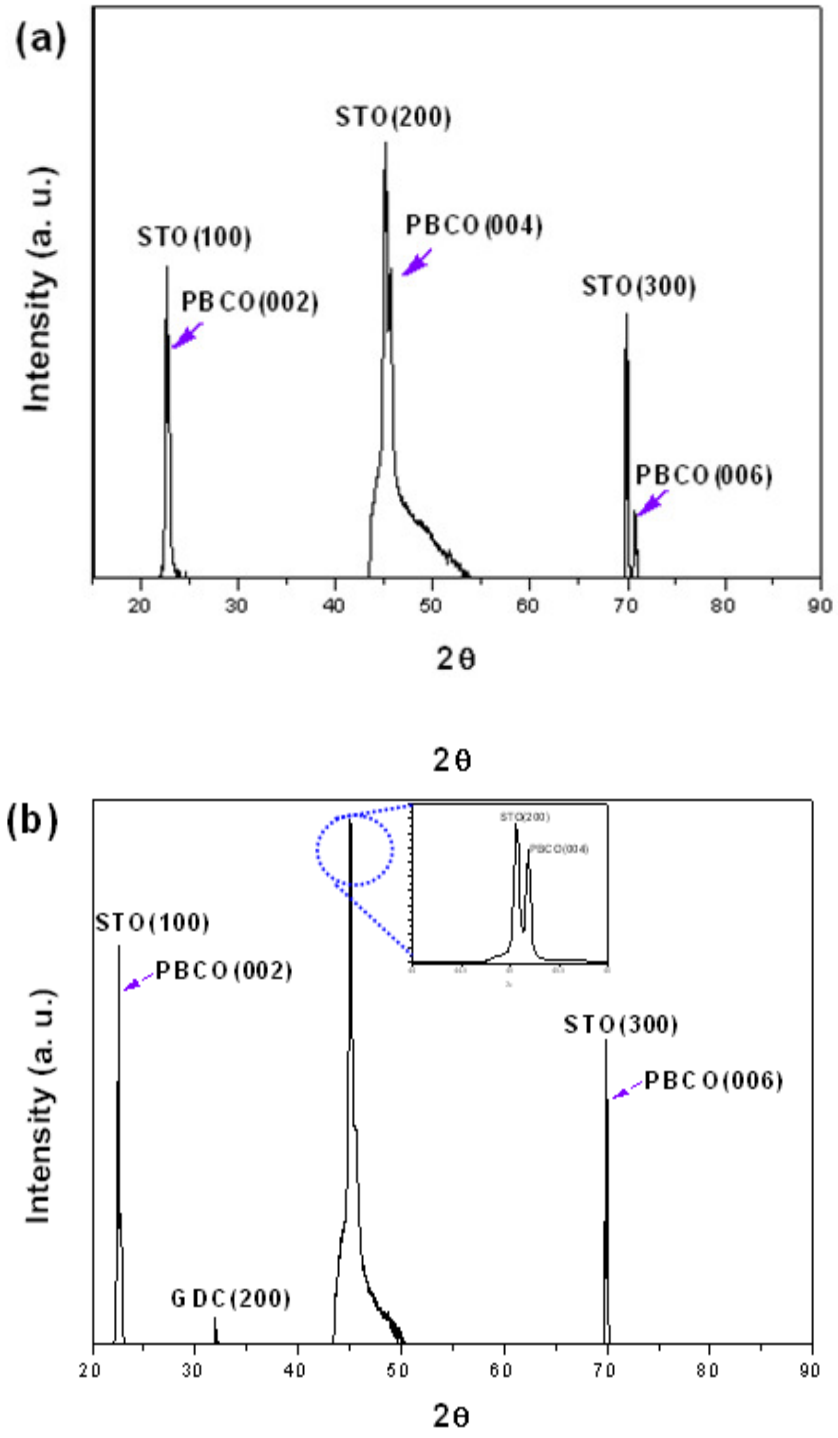

Fig 6.2. XRD patterns of (a) PBCO thin film and (b) PBCO/GDC composite film.

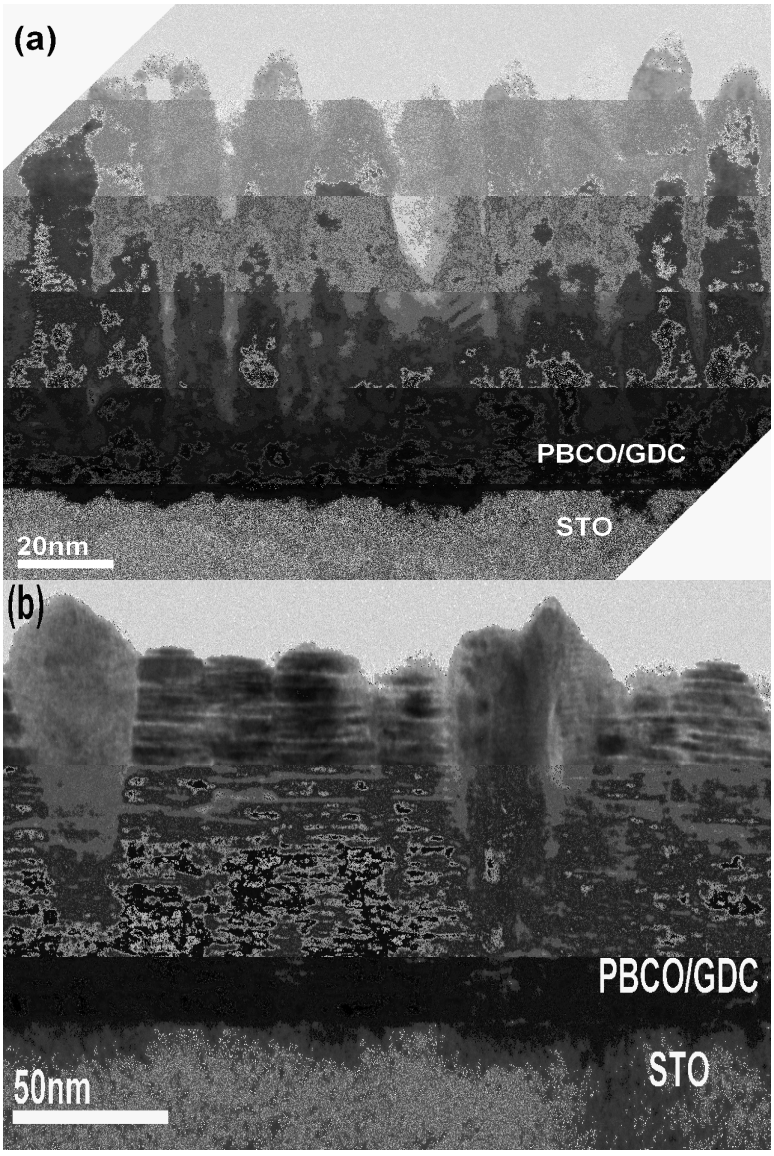

Fig 6.3. **C**ross-sectional TEM images of the PBCO/GDC thin films: (a) deposited at 600ºC and (b) deposited at 750ºC.

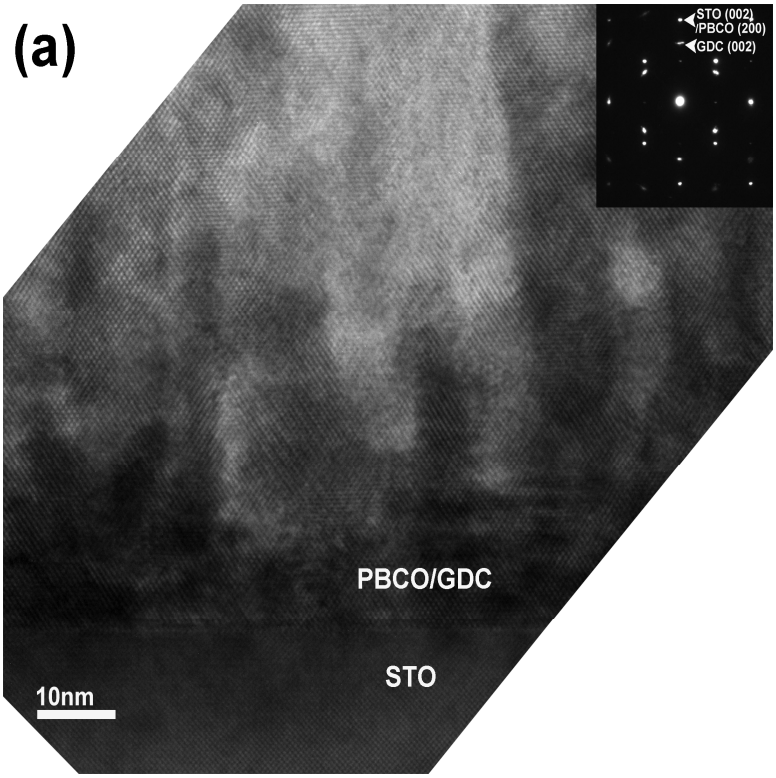

Fig 6.4. Cross-sectional (a) low magnification, (b) high resolution TEM images, and (c) STEM (Z-contrast) image of the PBCO/GDC VAN structure grown on STO substrate at 600ºC.

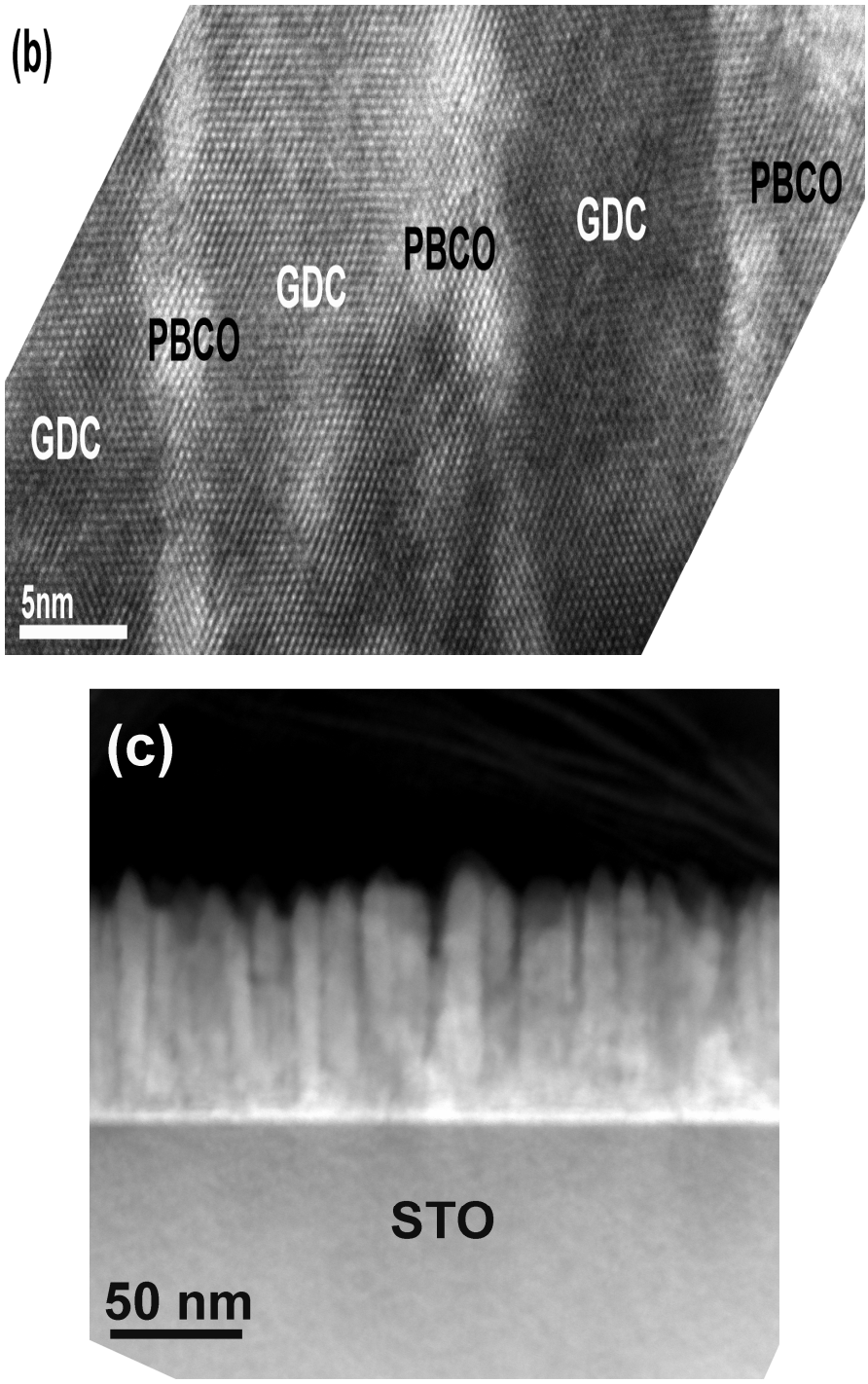

Fig 6.4. Continued.

One such image in Fig 6.4(c) shows well-aligned vertical columns with the different contrast from PBCO (darker contrast) and GDC (brighter contrast) columns, which is consistent with the TEM observations. Fig 6.5 shows the high resolution cross-sectional TEM images of the PBCO/GDC thin film deposited at 750ºC. As seen in Fig 6.5(a), the lateral layers are the alternating PBCO and GDC layers indicating by alternating bright and dark contrasts. The nanolayer thickness is about ~2.3 nm and ~1.0 nm for the PBCO and GDC nanolayers, respectively. The corresponding SAD diffraction pattern clearly indicates the high quality epitaxial growth of the PBCO and GDC phases. As shown in Fig 6.5(c), STEM image confirms the apparent nanolayer structure of PBCO and GDC with high epitaxial quality and smooth interface.

It is interesting to note that the deposition temperature strongly affects the architecture of the PBCO/GDC nanocomposite thin film, i.e., from the vertically aligned columnar structure (Fig 6.4) to the lateral layered structure (Fig 6.5). It has been reported for the VAN structure the phase separation in Perovskite systems indicates the close proximity to the free energy minima, because the fast growth kinetics are possible to reach by spinodal decomposition in proper timescales [183-184]. However, the nanocomposite structure is strongly affected by the growth kinetics. For example, the VAN structure is formed only when the desired adatom surface mobility and the deposition rate were applied.

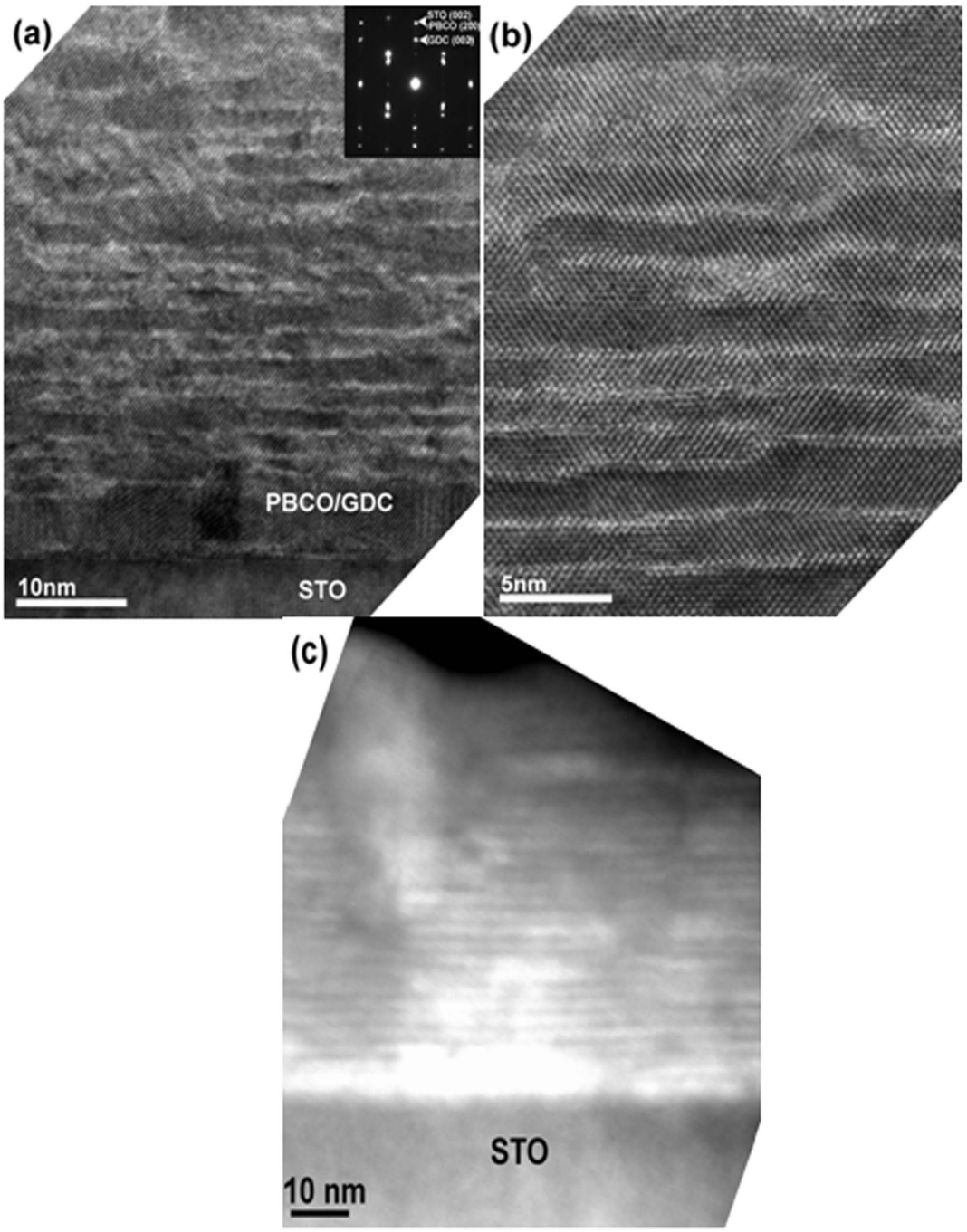

Fig 6.5. Cross-sectional (a) low magnification, (b) high resolution TEM images, and (c) STEM (Z-contrast) image of the PBCO/GDC nanolayered structure grown on STO substrate at 750ºC.

Fig 6.6(a) shows the AC impedance spectra in the form of a Nypuist plot for a symmetric cell with a 150 nm PBCO/GDC interlayer at 350°C. This measured impedance data is fitted well to an equivalent circuit as shown in Fig 6.6(b). In this model, a constant phase element (CPE) is used to study the inhomogeneous porous electrode/electrolyte systems for exact fitting results. The first small arc at the high and medium frequency intercepts of the spectrum is related to the contributions of the Pt wire and bulk electrolyte resistance which is represented as R_0 and (R_1-CPE_1) circuits. The second semicircle is associated with the electrode polarization resistance at the low frequency range. With the fitting results, the (R_2-CPE_2) circuit is for the oxide ion transfer through the electrode/electrolyte interface and both (R_3-CPE_3) and (R_4-CPE_4) are attributed to an electron charge transfer in the typical range at the interface which is in good agreement with previous literatures [185-186].

To compare area specific resistance (ASR) of symmetric cells without and with a 150 nm interlayer, the ASR of the cathode was calculated by the following equation:

$$ASR = [(R_p = R_2+R_3+R_4)] * (Area) /2 \quad (6.1)$$

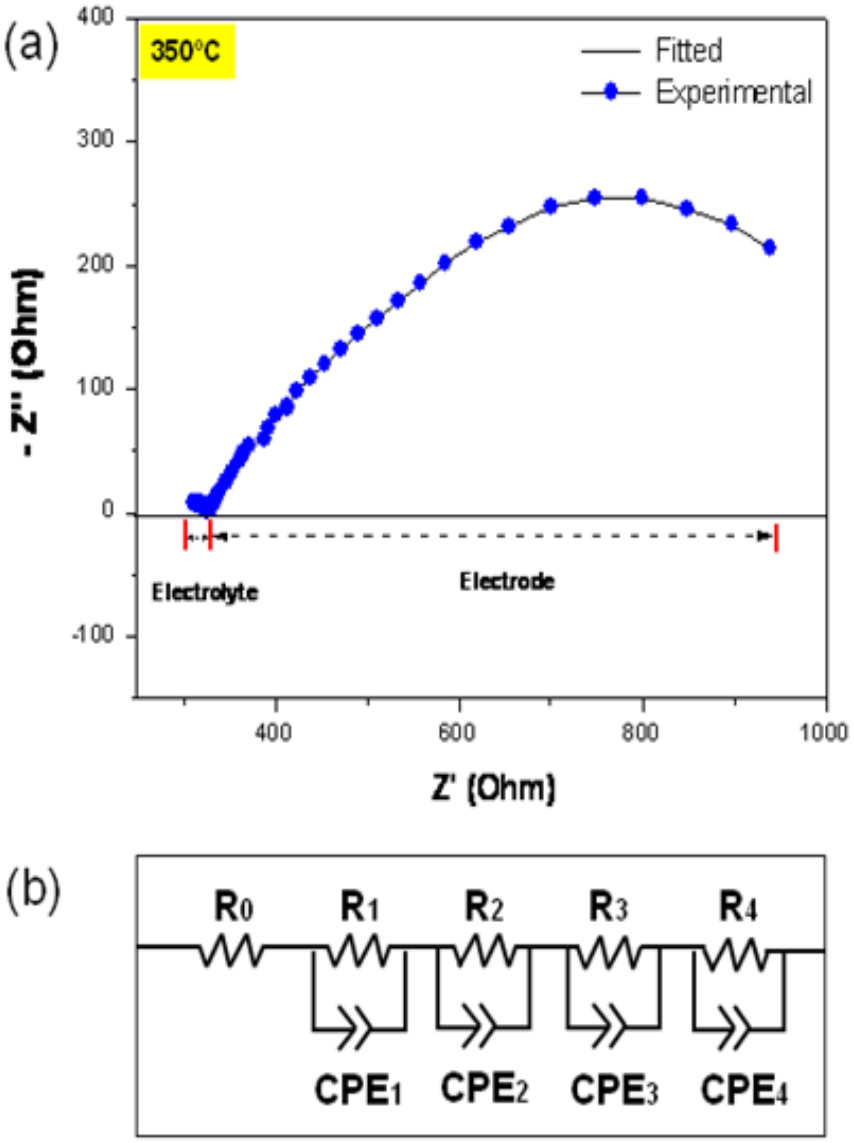

Fig 6.6. AC impedance spectra of Nyquist plot of the symmetric cell with PBCO/GDC interlayer at 350ºC.

The calculation was based on the AC impedance data under air in the temperature range of 350–650°C. As shown in Fig. 6. 7, the ASR of the cell with the VAN interlayer shows a lower value in comparison to the results obtained for the cell

without the interlayer. For example, the cell without interlayer has a higher ASR (2.5 Ωcm^2) than the one with the interlayer (2.1 Ωcm^2) at 400°C. Therefore, the VAN PBCO/GDC interlayer incorporation into the PBCO cathode which can affect the total polarization of cathode with increasing the effective area of the TPBs. The interlayer also improves the catalytic reaction probability at the gas–cathode–electrolyte TPBs. Accordingly, a decrease of the ASR of the cathode could lead to a better performance in TFSOFCs.

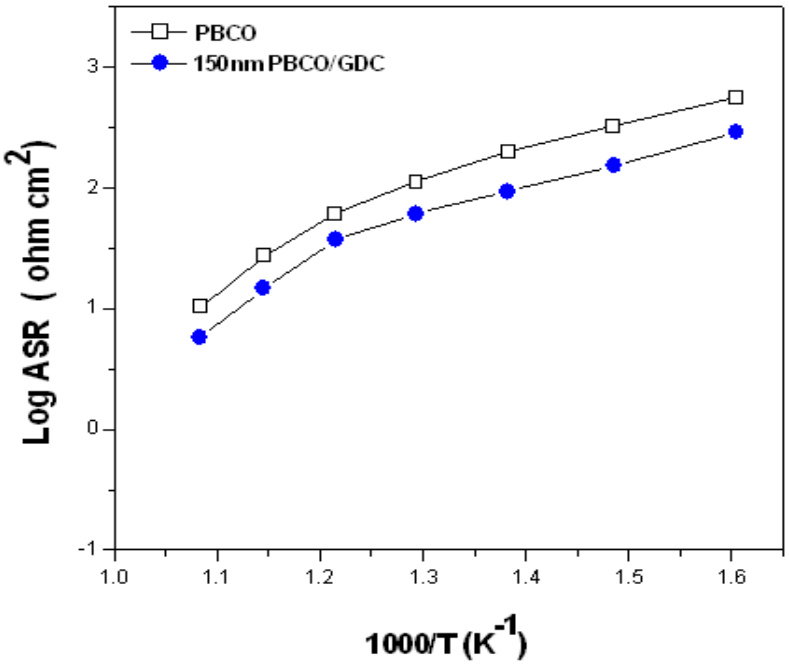

Fig 6.7. Area specific resistance (ASR) of the symmetric cells with and without the VAN PBCO/GDC structure grown by PLD.

An anode-supported single cell with the PBCO/GDC interlayer was prepared for the I-V characteristic measurement at the temperatures of 650-750°C. Fig 6.8 presents the cell voltage and power density as a function of the current density by a two-electrode set-up under humidified hydrogen at the rate of 100 mL min^{-1}, using Pt wires as electrical contacts on both sides of the cell. The open circuit voltages (OCV) of 0.88 V was obtained at 750°C by implementing the bilayer CGO/ YSZ. Adding a thin YSZ can suppress ceria reduction at the anode side and improve the power output based on our previous work [187]. The general trend is that the cell voltage drops with respect to increasing current density at each temperature. The maximum power density of the cell with the PBCO/CGO interlayer is 151, 263, and 350 (highlighted as red arrow) $mWcm^{-2}$ at 650, 700, and 750^{o}C, respectively. Besides, it is worth to note that concentration polarization in the IV curve is observed under current drain of ~0.8 A/cm^2 which indicates the limited fuel supply due to the low porosity in the anode side. The true maximum power density of the cell at 750^{o}C shall be higher under the optimized porosity in the anode side.

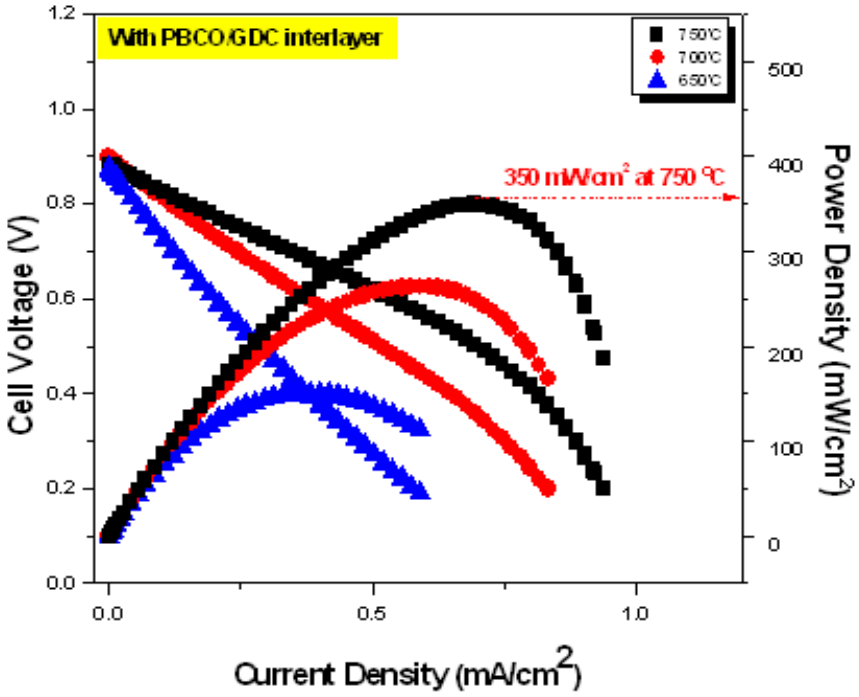

Fig 6.8. I-V curve of the anode-supported single cell with PBCO/GDC interlayer at different temperatures of 650 ~ 750 °C.

Cross-sectional SEM image in Fig 6.9 shows the anode-supported single cell after the power measurements at high temperatures. The microstructures of PBCO/GDC interlayer and YSZ/GDC bilayer can be clearly observed as ~1 μm and ~6 μm, respectively. The bilayer electrolyte shows fully dense structure with an obvious interface between the YSZ and GDC layers in the cell. The PBCO cathode and NiO-GDC anode exhibit a porous structure with uniform pore distribution. It is evidence that there is no crack or delamination issue observed at the interfaces between the cathode,

interlayer, and electrolyte thin film layers. This suggests that the PBCO/GDC interlayer acts as an effective transition layer and improve the adhesion properties between the cathode and electrolyte.

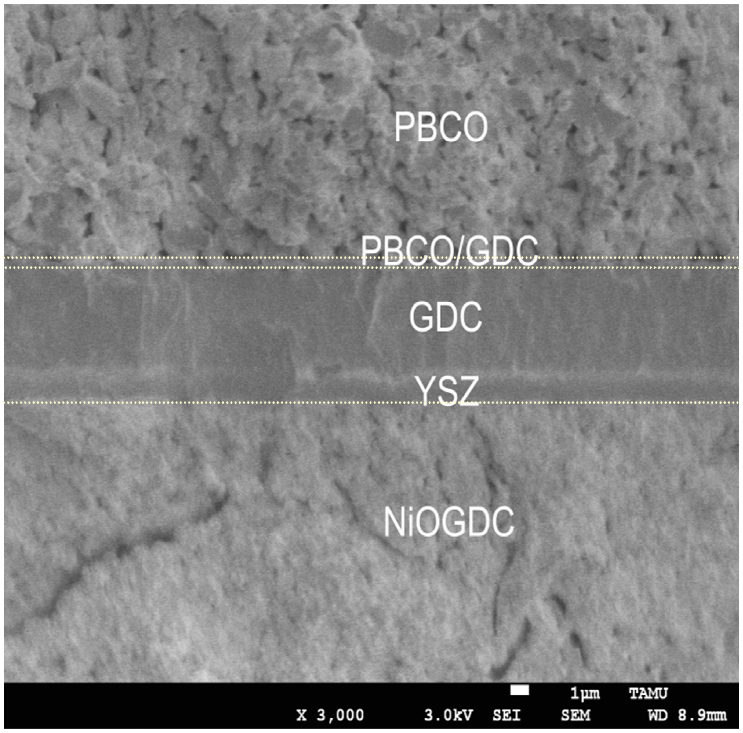

Fig 6.9. Cross sectional SEM images of the anode supported single cell with PBCO/GDC interlayer after power measurement.

6.5 Conclusions

The VAN structures of the PBCO/GDC interlayer between the cathode and electrolyte for thin film solid oxide fuel cells (TFSOFCs) were prepared by PLD. The PBCO/GDC thin film interlayer shows either the vertically ordered columnar structure (600^{o}C) or the nanolayered structure (750^{o}C). Both cases, the nanocomposite films have highly epitaxial growth on the substrates. The symmetric cell with the VAN PBCO/GDC interlayer shows a lower ASR of 2.1 Ωcm^2 at 400 °C compared to the cell without the interlayer (2.5 Ωcm^2). The single cell with the PBCO/GDC interlayer shows the OCV of 0.9 V at 750^{o}C and the maximum power densities of 151, 263, and 350 $mWcm^{-2}$ at 650, 700, and 750^{o}C, respectively. Overall the VAN PBCO/GDC interlayer performs as an adequate transition layer between the cathode and electrolyte, enhances the adhesion properties in between the layers, and thus leads to improve the overall cell performance.

CHAPTER VII

CONCLUSIONS

Designing thin films of a vertically-aligned nanocomposite (VAN) structure of $La_{0.5}Sr_{0.5}CoO_3$ or $PaBaCo_2O_{5+\delta}$ and $Ce_{0.9}Gd_{0.1}O_{1.95}$ and nanostructure thin film electrolytes have been demonstrated for thin film solid oxide fuel cells (TFSOFCs).

First, the binary VAN interlayer of $(LSCO)_{0.5}(CGO)_{0.5}$ between the cathode and electrolyte was achieved. This unique binary VAN interlayer effectively increases the cathode/electrolyte interfacial area density (by 14~25 times depending on the interlayer thickness) and significantly lowers the polarization resistance at the cathode/electrolyte interface. The effect of varying deposition parameters such as the pressure and pulse time on the VAN interlayer thickness and column width can be systematically controlled by varying these two dimensions. As the VAN thickness increases, the ASR shifts to lower values as well as the power performance of the cell is enhanced at intermediate operating temperatures.

Second, the GDC thin film electrolyte with different grain sizes at various deposition temperatures was demonstrated. The crystallinity of the films has been found to increase with increasing substrate temperature. The GDC thin film deposited above 500 ºC starts to show epitaxial growth on YSZ substrates. A series of electrical properties as functions of temperature and grain size show that the films with large grains (deposited at higher temperatures) have higher conductivity and lower activation energy than the films with small grains and poor grain connectivity (deposited at lower

temperatures). The substrate temperature significantly influences the microstructure of the GDC films (i.e., grain size and grain morphologies) and its overall electrical properties including ionic conductivity.

Third, YSZ/GDC (~6 μm) bilayer electrolytes with the YSZ thickness varied from ~330 nm to ~1 μm were achieved for thin film SOFCs. The incorporation of YSZ thin film in the bilayer electrolyte cells will suppress the electrical current leakage and chemical reduction of ceria from Ce^{4+} to Ce^{3+} from the anode side where the electrolyte is exposed to a reducing atmosphere. This YSZ/GDC bilayer electrolyte has shown the effectiveness of YSZ as an electron blocking layer. Based on the microstructural, electrochemical, and power measurement results, a tailored bilayer electrolyte is needed for the optimization of power density characteristic and electrolyte stability i.e., the bilayer structure improves the cell voltage by shifting the potential displacement at the electrolyte interface under the reducing conditions. The ceria-based electrolyte with the thin YSZ interlayer presents a feasible architecture for improving the overall power density and enabling chemical, mechanical, and structural stability in the cells.

Fourth, the VAN structures of PBCO/GDC interlayer between the cathode and electrolyte were prepared for TFSOFCs. The PBCO/GDC thin film interlayer shows either the vertically ordered columnar structure (600^{o}C) or the nanolayered structure (750^{o}C). In both cases, the nanocomposite films have highly epitaxial growth with the substrates. The symmetric cell with the VAN PBCO/GDC interlayer shows a lower ARS with a good power output. The overall the VAN PBCO/GDC interlayer acts as an effective transition layer between the cathode and electrolyte, which enhances the

adhesion properties in between the layers, and thus leads to an improved overall cell performance.

The future work could focus on the fundamental understanding of the growth mechanism of the binary VAN structure and further electrochemical analysis.

REFERENCES

[1] A. J. Bard, L. R. Faulkner, *Electrochemical Methods: Fundamentals and Applications*, John Wiley & Sons Inc, New York 1980.

[2] W.R. Grove, *Philos. Mag*. **1839**, *14*, 127.

[3] *Fuel Cell Handbook* (7th ed.), Tech. Rep. DOE/NETL 2004/1206, National Energy Technology Laboratory, Morgantown, WV 2004. (http://www.netl.doe.gov).

[4] N. Q. Minh, T. Takahshi, *Science and Technology of Ceramic Fuel,* Elsevier Science B. V, Amsterdam, Netherlands 1995.

[5] S. Singhal, K. Kendall, *High-temperature Solid Oxide Fuel Cells: Fundamentals, Design and Applications*, Elsevier Science Ltd, Oxford UK 2004.

[6] G. Hoogers, *Fuel Cell Technology Handbook*, CRC, Boca Raton, FL 2003.

[7] W. Z. Nernst, *Electrochem.* **1899**, *6*, 41.

[8] A. Boudghene Stambouli,E. Traversa, *Renew. Sustain. Energy Rev,* **2002***, 6,* 433.

[9] A. Negishi, K. Nozaki, T. Ozawa, *Solid State Ionics*, **1981**, *3*, 443.

[10] S. Souza, S. J. Visco, L.C. De Jonghe, *Solid State Ionics*, **1997**, *98*, 57.

[11] J. Will, A. Mitterdorfer, C. Kleinlogel, D. Perednis, L. J. Gauckler, *Solid State Ionics*, **2000**, *131*, 79.

[12] P. J. Kelly, R. D. Arnell, *J. Vacuu*m, **2000**, *56*, 159.

[13] T. W. Kueper, S. J.Visco, L. C. Jonghe, *Solid State Ionics*, **1992**, *52*, 251.

[14] S. Sameshima, *Mater. Chem. Physics*, **1999**, *61*, 31.

[15] A. Bieberle, L. J. Gauckler, *Z. Metallkd*, **2001**, *92*, 796.

[16] S. P. Jiang, Y. Y. Duan, J. G. Love, *J. Electrochem. Soc*, **2002**, *149*, A1175.

[17] M. Brown, S. Primdahl, M. Mogensen, *J. Electrochem. Soc*, **2000**, *147*, 475.

[18] A. Lashtabeg, S. J. Skinner, *J. Mater. Chem*, **2006**, *16*, 3161.

[19] B. C. H. Steele, *J. Mater. Sci*, **2001**, *36*, 1053.

[20] S. Somiya, N. Yamamoto, H. Yanagida, Science and Technology of Zirconia III (Advances in Ceramics ,Vol 24B) The American Ceramic Society, Columbus, Ohio 1988.

[21] A. H. Heuer, L. W. Hobbs, Science and Technology of Zirconia (Advances in Ceramics, Vol 3). The American Ceramic Society, Columbus, Ohio 1981.

[22] N. Sammes, Y. Du, *Fuel Cell Technol: State and Perspec*, *19*, **2005**.

[23] M. Mogensen, N. M. Sammes, G. A. Tompsett, *Solid State Ionics*, **2000**, *129*, 63.

[24] B. C. H. Steele, *Solid State Ionics*, **2000**, *129*, 95.

[25] K. Huang, R.S Tichy, J. B. Goodenough, *J. Am. Ceram. Soc*, **1998**, *81*, 2565.

[26] K. Huang, R.S Tichy, J. B. Goodenough, *J. Am. Ceram. Soc*, **1998**, *81*, 2576.

[27] T. Ishihara, H. Matsuda, Y.Takita, *J. Am. Chem. Soc*, **1994**, *116,* 3801.

[28] M. Feng, J. B. Goodenough, *Eur J. Solid State Inorg. Chem*, **1994**, *31*, 663.

[29] S. P. Simner, J. F. Bonnett, N. L. Canfield, K. D. Meinhardt, J. P. Shelton, V. L. Sprenkle, J. W. Stevenson, *J. Power Sources*, **2003**, *113*, 1.

[30] T. Bak, J. Nowotny, M. Rekas, C. C. Sorrell, E. R. Vance, *Solid State Ionics,* **2000**, *135*, 557.

[31] Y. Teraoka, T. Nobunaga, K. Okamoto, N. Miura, N. Yamazoe, *Solid State Ionics*, **1991**, *48*, 207.

[32] Z. P. Shao, S. M. Haile, *Nature*, **2004**, *431*, 170.

[33] D. Waller, J. A. Lane, J. A. Kilner, B. C. H. Steele, *Mater. Lett*, **1995**, *27*, 225.

[34] L.-W. Tai, M. N. Nasrallah, H. U. Anderson, D. M. Sparlin, S. R. Sehlin, *Solid State Ionics*, **1995**, *76*, 273.

[35] T. Kenjo, M. Shimizu, K. Sasaki, *Denki Kagaku*, **1992**, *60*, 700.

[36] A. M. Chang, S. J. Skinner, J. A. Kilner, *Solid State Ionics*, **2006**, *177*, 19.

[37] G. Kim, S. Wang, A. J. Jacobson, Z. Yuan, W. Donner, C. L. Chen, L. Reimus, P. Brodersen, C. A. Mims, *Appl. Phys. Lett*, **2006**, *88*, 024103.

[38] K. Tomida, T. Namikawa, Y. Yamazaki, *Denki Kagaku*, **1994**, 62, 1043.

[39] B.C. H. Steele, A. Heinzel, *Nature*, **2001**, *414*, 345.

[40] I. Kosackia, C. M. Rouleaub, P. F. Bechera, J. Bentleya, D. H. Lowndes, *Solid State Ionics*, **2005**, *176*, 1319.

[41] Y.-M. Chiang, E. B. Lavik, I. Kosacki, H. L. Tuller, J. Y. Ying, *Appl. Phys. Lett*, **1996**, *69*, 185.

[42] A. Tschöpe, R. Birringer, *J. Electroceram*, **2001**, *7*, 169.

[43] S. Kim, J. Maier, *J. Electrochem. Soc*, **2002**, *149*, J73.

[44] A. Tschöpe, *Solid State Ionics*, **2001**, *139*, 267.

[45] Y. -M. Chiang, E. B. Lavik, I. Kosacki, H. L. Tuller, *J. Electroceram*, **1997**, *1*, 7.

[46] T. Suzuki, I. KosackiI, H. U. Anderson, *Solid State Ionics*, **2002**, *151*, 111.

[47] S. Azad, O. A. Marina, C. M. Wang, L. Sara, V. Shutthanandan, D. E. McCready, A. El-Azab, J. E. Jaffe, M. H. Engelhard, C. H. F. Peden, and S. Thevuthasan, *Appl. Phys. Lett*, **2005**, *86*, 131906.

[48] C. Wagner, *J. Phys. Chem. Solids*, **1972**, *33*, 1051.

[49] J. Maier, *Prog. Solid State Chem*, **1995**, *23*, 171.

[50] R. Chockalingam, V. R. W. Amarakoon, H. Giesche , *J. Eur. Ceram. Soc*, **2008**, *28*, 959.

[51] N. Imanishia, T. Matsumura, Y. Sumiya, K. Yoshimura, A. Hirano, Y. Taked, D. Mori, R. Kanno, *Solid State Ionics*, **2004**, *174*, 245.

[52] T. Kawada, K. Masuda, J. Suzuki, A. Kaimai, K. Kawamura, Y. Nigara, J. Mizusaki , H. Yugami , H. Arashi , N. Sakai , H. Yokokawa*, Solid State Ionics*, **1999**, *121*, 271.

[53] G. Kim, S. Wang, A. J. Jacobson, L. Reimus, P. Brodersen, C. A. Mims, *J. Mater. Chem*, **2007**, *17*, 2500.

[54] A. Orera, P. R. Slater, *Chem. Mater*, **2009**, *22*, 675.

[55] A. J. Jacobson, *Chem. Mater*, **2009**, *22*, 660.

[56] C. Sun, *J. Solid State Electr*, **2010**, *14*, 1125.

[57] A. Tarancón, M. Burriel, J. Santiso, S. J. Skinner, J. A. Kilner, *J. Mater. Chem*, **2010**, *20*, 3799.

[58] X. Chen, S. Wang, Y. L. Yang, L. Smith, N. J. Wu, B. -I. Kim, S. S. Perry, A. J. Jacobson, A. Ignatiev, *Solid State Ionics*, **2002**, *146*, 405.

[59] M. Burriel, C. Niedrig, W. Menesklou, S. F. Wagner, J. Santiso, E. Ivers-Tiffée, *Solid State Ionics*, **2010**, *181*, 602.

[60] M. Burriel, J. Santiso, M. D. Rossell, G. Van. Tendeloo, A. Figueras, G. Garcia, *J. Phys. Chem*. C, **2008**, *112*, 10982.

[61] C. Grygiel, S. R. C. McMitchell, Z. Xu, L. Yan, H. J. Niu, D. Giap, J. Bacsa, P. R. Chalker, M. J. Rosseinsky, *Chem. Mater,* **2010**, *22*, 1955.

[62] M. Burriel, M. C. Cabanas, J. Zapata, H. Tan, J. Verbeeck, C. Sol, J. Roqueta, S. J. Skinner, J. A. Kilner, G. V. Tendeloo, J. Santiso, *Chem. Mater*, **2010**, *22*, 5512.

[63] D. Beckel, A. Bieberle-H¨utter, A. Harvey, A. Infortuna, U. P. Muecke, M. Prestat, J. L. M. Rupp, L. J. Gauckler, *J. Power Sources*, **2007**, *173*, 325.

[64] B. Huang, X. –J. Zhu, W. –Q. Hu, Y. –Y. Wang, Q. –C. Yu, *J. Power Sources*, **2010**, *195*, 3053.

[65] M. Chen, B. H. Kim, Q. Xu, B, G. Ahn, *J. Membr. Sci*, **2009**, *334*, 138.

[66] H. -S. Noh, J.-S. Park, J. -W. Son, H. Lee, J. –H. Lee, H. -W. Lee, *J. Am. Ceram. Soc*, **2009**, *92*, 3059.

[67] A. Infortuna, A. S. Harvey, U. P. Muecke, L. J. Gauckler, *Phys. Chem. Chem. Phys*, **2009**, *11*, 3663.

[68] M. Brandner, M. Bram, J. Froitzheim, H.P. Buchkremer and D. Stover, *Solid State Ionics,* **2008***, 179*, 1501.

[69] K**.** Chen, X. Chen, Z. Lü, N. Ai, X. Huang and W. Su, *Electrochem. Acta*, **2008**, *53*, 7825.

[70] R. K. Singh, J. Narayan, A. K. Singh, J. Krishnawmy, *Appl. Phys. Lett*, **1989**, *54*, 2271.

[71] R. K. Singh, O. W. Holland, J. Narayan, *J. Appl. Phys*, **1990**, *68*, 233.

[72] R. K. Singh, J. Narayan, *Phys. Rev. B*, **1990**, *41*, 8843.

[73] B. D. Cullity, *Elements of X-Ray Diffr.*, Addison-Wesley, Inc, Reading, MA 1982.

[74] M. Birkholz, *Thin Film Analysis by X-Ray Scattering,* Wiley-VCH Verlag GmbH& Co, Heidelberg, Germany 2006.

[75] H. Bullen, *Introduction to X-ray Diffraction (XRD) Learning Activity* (http://www.asdlib.org/)

[76] *Atomic Force Microscope*, Nanoscience Inc (http://www.nanoscience.com/ education/afm.html)

[77] A.V. Clemente, *Principle of atomic force microscope* (http://www.mansic.eu Documents /PAM1/Frangis.pdf).

[78] B. Hafner, *Scanning Electron Microscopy Primer*, (http://www.charfac.umn.edu/ (2008) sem_primer.pdf).

[79] R. F. Egerton, *Physical Principles of Electron Microscopy*, Springer Science Business Media Inc, New York 2005.

[80] B. Fultzz, J. M. Howe, *Transmission Electron Microscopy and Diffractometry of Materials*, 3rd Ed, Springer, New York 2007.

[81] M. E. Orazem, B. Tribollet, *Electrochemical Impedance Spectrosco*py, John Wiley& Sons, New York 2008.

[82] *Electrical test methods for on-line fuel cell ohmic resistance measurement*, Scribner Accociates Inc (http://www.scribner.com/component/option,com _quickfaq/Itemid,230/cid,2/id,20/view, items/)

[83] L. J. van der Pauw, *Philips. Res. Repts*, **1958**, *13*, 1.

[84] M. P. Gutiérrez, Thin film surface resistivity (www.sjsu.edu/faculty/selvaduray/ page/papers/mate210/thinfilm.pdf).

[85] H. Apfel, A. Rzepka, H. Tu, U. Stimming, *J. Power Source*, **2006**, *154*, 370.

[86] B. Kenney, K. Karan, *Solid State Ionics*, **2007**, *178*, 297.

[87] M. H. Hung, M. V. M. Rao, D. S. Tsai, *Mater. Chem. Phys*, **2007**, *101*, 297.

[88] J. Deseure, Y. Bultel, L. Dessemond, E. Siebert, P. Ozil, *Appl. Electrochem*, **2007**, 37, 129.

[89] M. Sase, J. Suzuki, K. Yashiro, T. Otake, A. Kaimai, T. Kawada, J. Mizusaki, H. Yugami, *Solid State Ionics*, **2006**, *177*, 1961.

[90] E. Koep, C. M. Jin, M. Haluska, R. Das, R. Narayan, K. Sandhage, R. Snyder, M. L. Liu, *J. Power Sources*, **2006**, *161*, 25.

[91] S. P. Yoon, J. Han, S. W. Nam, T. H. Lim, S. A. Hong, *J. Power Sources*, **2004**, *136*, 30.

[92] J.-H. Kim, F. Prado, A. Manthiram, *J. Electrochem. Soc*, **2008**, *155*, B1023.

[93] J.-H. Kim, A. Manthiram, *J. Electrochem. Soc*, **2008**, *155*, B385.

[94] B. S. Kang, H. Wang, J. L. MacManus-Driscoll, Y. Li, Q. X. Jia, I. Mihut, J. B. Betts, *Appl. Phys. Lett*, **2006**, *88*, 1453.

[95] J. L. MaCmanus-Driscoll, P. Zerrer, H. Wang, H. Yang, J. Yoon, A. Fouchet, R. Yu, M. G. Blamire, Q. X. Jia, *Nat Mate*, **2008**, *7*, 314.

[96] Z. Bi, J. Lee, H. Yang, Q. Jia, J. L. MacManus-Driscoll, H. Wang, *J. Appl. Phys*, **2009**, *106,* 094309.

[97] J. Yoon, R. Araujo, N. Grunbaum, L. Baque, A. Serquis, A. Caneiro, X. H. Zhang, H. Wang, *Appl. Surf. Sci*, **2007**, *254*, 266.

[98] V. Dusastre, J. A. Kilner, *Solid State Ionics*, **1999**, *126*, 163.

[99] L. Baqué, A. Caneiro, M. S. Moreno, A. Serquis, *Electrochem. commun*, **2008**, *10*, 1905.

[100] B. C. H. Steele, *Solid State Ionics*, **2000**, *129*, 95.

[101] A. O. Stoermer, J. L. M. Rupp, L. J. Gauckler, *Solid State Ionics*, **2006**, *177*, 2075.

[102] S. Zha, A. Moore, H. Abernathy, M. Liu, *J. Electrochem. Soc*, **2004**, *151*, A1128.

[103] A. Jaiswal, E. D. Wachman, *Ionics*, **2005**, *11*, 161.

[104] G. L. Liu, K. A. Khor, S. H. Chan, X. J. Chen, *J. Power Sources*, **2006**, *162*, 1036.

[105] A. V. Virkar, *J. Electrochem. Soc*, **1991**, *138*, 1481.

[106] Y. D. Zhen, A. I. Y. Tok, S. P. Jiang, F. Y. C. Boey, *J. Power Sources*, **2008**, *178*, 69.

[107] S. H. Chan, X. J. Chen, K. A, Khor, *Solid State Ionics*, **2003**, *158*, 29.

[108] M. Mogensen, N. M. Sammes, G. A. Tompsett, *Solid State Ionics*, **2000**, *129*, 63.

[109] B. C. H, Steel, *Solid State Ionics*, **2000**, *129*, 95.

[110] T. Suzuki, I. Kosacki, H. U. Anderson, *Solid State Ionics*, **2002**, *151*, 111.

[111] D. X. Huang, C. L. Chen, A. J. Jacobson, *Appl. Phys. Lett*, **2003**, *83*, 043506-1.

[112] D. X. Huang, C. L. Chen, L. Chen, A. J. Jacobson, *Appl. Phys. Lett*, **2004**, *84*, 708.

[113] C. Kleinlogel, L. J. Gauckler, *Solid State Ionics*, **2000**, *135*, 567.

[114] G. Chiodelli, L. Malavasi, V. Massarotti, P. Mustarelli, E. Quartarone, *Solid State Ionics*, **2005**, *176*, 1505.

[115] T. Ishihara, T. Shibayama, M. Honda, H. Nishiguchi, Y. Takita, *J. Electrochem. Soc*, **2000**, *147*, 1332.

[116] J. W. Kim, A. V. Virkar, K. Z. Fung, K. Mehta, S. C. Singhal, *J. Electrochem. Soc*, **1999**, *146*, 9.

[117] J. Will, A. Mitterdorfer, C. Kleinlongel, D. Perednis, L. J. Gauckler, *Solid State Ionics*, **2000**, *131*, 79.

[118] R. Maric, S. Ohara, T. Fukui, H. Yoshida, M. Nishimura, T. Inagaki, K. Miura, *J. Electrochem. Soc*, **1999**, *146*, 2006.

[119] C. Xia, M. Liu, *J. Adv. Mater*, **2002**, *14*, 521.

[120] T. Ishihara, K. Sato, Y. Takita, *J. Am. Ceram. Soc*, **1996**, *79*, 913.

[121] J. A. Kilner, *Solid State Ionics*, **2000**, *129*, 13.

[122] S. de Souza, S. J. Visco, L. C. de Jonghe, *Solid State Ionics*, **1997**, *98*, 57.

[123] C. Xia, F. Chen, M. Liu, *Electrochem. Solid-State Lett*, **2001**, *4*, A52.

[124] S. P. Jiang, Y. J. Leng, S. H. Chan, K. A. Khor, *Electrochem. Solid-State Lett*, **2003**, *6*, A67.

[125] J. L. M. Rupp, L. J. Gauckler, *Solid State Ionics*, **2006**, *177*, 2513.

[126] Y. -L. Kuo, C. Lee, Y-S. Chen, H. Liang, *Solid State Ionics*, **2009**, *180*, 1421.

[127] L. Chen, C. L. Chen, X. Chen, W. Donner, S. W. Liu, and Y. Lin, D. X. Huang, A. J. Jacobson, *Appl. Phys. Lett*, **2003**, *83*, 4737.

[128] J. H. Joo, G. M. Choi, *Solid State Ionics*, **2007**, *27*, 4273.

[129] A. Infortuna, A. S. Harvey, L. J. Gauckler*, J. Adv. Func. Mater*, **2008**, *18*, 127.

[130] K. Rodrigo, J. Knudsen, N. Pryds, J. Schou, S. Linderoth, *Appl. Sur. Sci*, **2007**, *254*, 1338.

[131] H. Wang, A. Sharma, A. Kvit, *J. Mater. Res*, **2001**, *16*, 9.

[132] J. Yoon, R. Araujo, N. Grunbaum, L. Baque, A. Serquis, A. Caneiro, X. H. Zhang, H.Wang, *Appl. Surf. Sci*, **2007**, *254*, 266.

[133] J. Yoon, S. Cho, J.-H. Kim, J.H. Lee, Z. Bi, A. Serquis, X. Zhang, A. Manthiram, H. Wang, *J. Adv. Func. Mater*, **2009**, *19*, 1.

[134] X. Zhou, W. Huebner, I. Kosacki, H. U. Anderson*, J. AM Ceramic Society*, **2002**, *85*, 1757.

[135] S. R. Hui, J. Roller, X. Zhang, C. D. Petit, Y. Xie, R. Maric, D. Ghosh, *J. Electrochem. Soc* (Solid Oxide Fuel Cell IX), **2005**, *2*, 964.

[136] E. Barsoukov, J. R. Macdonald: *Impedance Spectroscopy Theory, Experiment, and Applications*, 2nd ed. John Wiley & Sons Inc, Hoboken, New Jersey 2005.

[137] B. C. H. Steele, *Solid State Ionics*, **2000**, *129*, 95.

[138] J. W. Kim, A. V. Virkar, K. Z. Fung, K. Mehta, S. C. Singhal, *J. Electrochem. Soc*, **2000**, *146*, 9.

[139] C. Xia, M. Liu, *J. Adv. Mater*, **2000**, *14*, 521.

[140] D. X. Huang, C. L. Chen, A. J. Jacobson, *Appl. Phys. Lett*, **2003**, *83*, 043506-1.

[141] D. X. Huang, C. L. Chen, L. Chen, A. J. Jacobson, *Appl. Phys. Lett*, **2004**, *84*, 708.

[142] T. Ishihara, T. Shibayama, M. Honda, H. Nishiguchi, Y. Takita, *J. Electrochem. Soc*, **2000**, *147*, 1332.

[143] Y. Mizutani, M. Tamura, M. Kawai and O. Yamamoto, *Solid State Ionics*, **1994**, *72*, 271.

[144] J. L. M. Rupp, L. J. Gauckler, *Solid State Ionics*, **2006**, *177*, 2513.

[145] Y-L. Kuo, C. Lee, Y-S. Chen, H. Liang, *Solid State Ionics*, **2009**, *180*, 1421.

[146] L. Chen, C. L. Chen, X. Chen, W. Donner, S. W. Liu, and Y. Lin, D. X. Huang, A. J. Jacobson, *Appl. Phys. Lett*, **2003**, *83*, 4737.

[147] A. Infortuna, A. S. Harvey, L. J. Gauckler*, J. Adv. Func. Mat*er, **2008**, *18*, 127.

[148] X. Zhou, W. Huebner, I. Kosacki, H. U. Anderson, *J. AM. Ceram. Soc*, **2002**, *8*, 1757.

[149] C. Brahim, A. Ringued´e, E. Gourba, M. Cassir, A. Billard, P. Briois, *J. Power Sources*, **2006**, *156*, 45.

[150] Q. L. Liu, K. A. Khor, S. H. Chan, X. J. Chen, *J. Power Sources*, **2006**, *162*, 1036.

[151] W. S. Jang, S. H. Hyun, *J. Mater. Sci*, **2002**, *37*, 2535.

[152] A. Tsoga, A. Gupta, A. Naounidis, P. Nikoloulos, *Acta mater*, **2000**, *48*, 4709.

[153] S. H. Chan, X. J. Chen, K. A. Khor, *Solid State Ionics*, **2003**, *158*, 29.

[154] A. Tsoga, A. Gupta, A. Naoumidis, D. Skarmoutsos, P. Nikolopoulos, *Ionics*, **1998**, *4*, 234.

[155] H. -T. Lim, A. V. Virkar, *J. Power Sources*, **2009**, *192*, 267.

[156] J. Yoon, S. Cho, J.-H. Kim, J. H. Lee, Z. Bi, A. Serquis, X. Zhang, A. Manthiram, H. Wang, *J. Adv. Func. Mater*, **2009**, *19*, 1.

[157] J.-H. Kim, Y. N. Kim, S. M. Cho, H. Wang, A. Manthiram, *Electrochim. Acta*, **2010**, *19*, 5312.

[158] J. H. Joo, G. M. Choi, *Solid State Ionics*, **2007**, *27*, 4273.

[159] S. Cho, J. Yoon, J.-H. Kim, X. Zhang, A. Manthiram, H. Wang, *J. Mater Res*, **2011**, *26*, 854.

[160] T. Tsai, E. Perry, S. Barnett, *J. Electrochem. Soc*, **1998**, *145*, 99.

[161] P. Soral, U. Pal, *J. Electrochem. Soc*, **1997**, *144,* L130.

[162] N. P. Brandon, S. Skinner, B. C. H. Steele, *Annu. Rev. Mater. Res*, **2003**, *33*, 183.

[163] C. Zuo, S. Zha, M. Liu, M. Hatano, M. Uchiyama, *Adv. Mater*, **2006**, *18*, 3318.

[164] M. Liu, D. Dong, L. Chen, J. Gao, X. Liu, G. Meng, *J. Power Sources*, **2008**, *176*, 107.

[165] E. Boehm, J.-M. Bassat, M. C. Steil, P. Dordor, F. Mauvy, J.-C. Grenier, *Solid State Sci*, **2003**, *5*, 973.

[166] Z. Tao, L. Bi, L. Yan, W. Sun, Z. Zhu, R. Peng, W. Liu, *Electrochem. Commun,* **2009**, *11*, 688.

[167] E. P. Murray, M. J. Sever, S. A. Barnett, *Solid State Ionics,* **2002**, *148*, 27.

[168] Z. Shao, S. M. Haile, *Nature*, **2004**, *431*, 170.

[169] C. Xia, W. Rauch, F. Chen, M. Liu, *Solid State Ionics*, **2002**, *149*, 11.

[170] G. Kim, S. Wang, A. Jacobson, Z. Yuan, W. Donner, C. L. Chen, L. Reimus, P. Brodersen, C. A. Mims, *Appl. Phys. Lett*, **2006**, *88*, 024103/1.

[171] G. Kim, S. Wang, A. J. Jacobson, L. Reimus, P. Brodersen, C. A. Mims, *J. Mater. Chem*, **2007**, *17*, 2500.

[172] M. Yadav, W. Gong, A. J. Jacobson, *J. Solid State Electrochem*, **2011**, *15*, 293.

[173] A. Yu. Suntsov, I. A. Leonidov, A. A. Markov, M. V. Patrakeev, Ya. N. Blinovskov, V. L. Kozhevnikov, *Rus. J. Phys. Chem. A*, **2009**, *83*, 832.

[174] H. Ding, Y. Xie, X. Xue, *J. Power Sources*, **2011**, *196*, 2602.

[175] Y. Lin, R. Ran, C. Zhang, R. Cai, Z. Shao, *J. Phys. Chem. A*, **2010**, *114*, 3764.

[176] J. Yoon, S. Cho, J.-H. Kim, J. H. Lee, Z. Bi, A. Serquis, X. Zhang, A. Manthiram, H. Wang, *J. Adv. Func. Mater*, **2009**, *19*, 1.

[177] B. Kenney, K. Karan, *Solid State Ionics*, **2007**, *178*, 297.

[178] M. H. Hung, M. V. M. Rao, D. S. Tsai, *Mater. Chem. Phys*, **2007**, *101*, 297.

[179] J. Deseure, Y. Bultel, L. Dessemond, E. Siebert, P. Ozil, *Appl. Electrochem*, **2007**, *37*, 129.

[180] M. Sase, J. Suzuki, K. Yashiro, T. Otake, A. Kaimai, T. Kawada, J. Mizusaki, H. Yugami, *Solid State Ionics*, **2006**, *177*, 1961.

[181] E. Koep, C. M. Jin, M. Haluska, R. Das, R. Narayan, K. Sandhage, R. Snyder, M. L. Liu*, J. Power Sources*, **2006***, 161*, 250.

[182] S. P. Yoon, J. Han, S. W. Nam, T. H. Lim, S. A. Hong, *J. Power Sources*, **2004**, *136*, 30.

[183] J. L. MacManus-Driscoll, *J. Adv. Func. Mater*, **2010**, *20*, 2035.

[184] H. Yang, H. Wang, B. Maiorov, J. Lee, D. Talbayev, M. J. Hinton, D. M. Feldmann, J. L. MacManus-Driscoll, A. J. Taylor, L. Civale, T. R. Lemberger, Q. X. Jia, *J. Appl. Phys*, **2009**, *106*, 093914.

[185] D. Chen, R. Ran, K. Zhang, J. Wang, Z. Shao, *J. Power Sources*, **2009**, *188*, 96.

[186] J.-H. Kim, Y. N. Kim, S. Cho, H. Wang, A. Manthiram, *Electrochim. Acta*, **2010**, *19*, 5312.

[187] S. Cho,.Y. N. Kim, J.-H. Kim, H. Wang, A. Manthiram, *Electrochim. Acta*, **2011**, *5656,*5472.

VITA

Name: Sungmee Cho

Address: Department of Electrical and Computer Engineering, Texas A&M University, 721 Jack E. Brown Engineering Bld., College Station, TX 77843-3128

Email Address: csmise@gmail.com

Education:

B.S.,	Chemical Engineering, Daejin Unversity, Korea, 2000
M.S.,	Chemical Engineering, Hongik University, Korea, 2002
Ph.D.,	Electrical and Computer Engineering, Texas A&M University, 2011

Journal Publications:

- **Sungmee Cho**, YoungNam. Kim, JoonHwan Lee, Arumugam. Manthiram, Haiyan Wang, ***J. Electrochimica Acta,*** **2011**, submitted.
- **Sungmee Cho**, YoungNam Kim, Jung-Hyun Kim, Arumugam Manthiram, and Haiyan Wang, ***J. Electrochimica Acta,*** 56, **2011**, 5472-5477.
- **Sungmee Cho,** Jongsik Yoon, Jung-Hyun Kim, Xinghang Zhang, Arumugam Manthiram and Haiyan Wang, ***J. Materials Research, 26,*** **2011**, 854-859.
- Jongsik Yoon, **Sungmee Cho**, Jung-Hyun Kim, Zhenxing Bi, Joonhwan Lee, Adriana Serquis, Xinghang Zhang, Arumugam Manthiram, and Haiyan Wang (The authors S. Cho and J. Yoon had an equal contribution.), ***J. Advanced Functional Material*****,** 19, **2009**, 1-6.
- J.-H. Kim, Y. N. Kim, **S. M. Cho**, H. Wang, and A. Manthiram, ***J. Electrochimica Acta,*** 19, **2010,** 5312-5317.
- Qing Su, **Sungmee Cho**, Zhenxing Bi, Aiping chen, Haiyan Wang, ***J. Electrochimica Acta,*** 56, **2011**, 3969-3974.
- S. Wang, **S. Cho**, H. Wang, and A. Jacobson, ***ECS Trans***, 35, **2011**, 1891.
- F. Napolitano, L. Baqué, **S. Cho**, S. Qing, H. Wang, A. Caneiro, A. Soldati, A. Serquis, ***219th ECS Meeting***, ***Trans***, 35, **2011**, 2379.
- **Sungmee Cho**, S. W. Lee, ByungWon Cho, Won Il Cho, JaeBeck Ju, TaeWon Sohn, ***J. Korean Electrochemical Society,*** 5, **2002**, 159-163.

This dissertation was typed by the author.